Thermal Stress Characteristics of Friction Welding

by

Aspen W. Glaspell

Submitted in Partial Fulfillment of the Requirements

for the Degree of

Doctor of Philosophy

in the

Materials Science and Engineering

Program

YOUNGSTOWN STATE UNIVERSITY

August, 2022

i

Thermal-Stress Analysis of Friction Welded Systems

Aspen W. Glaspell

I hereby release this dissertation to the public. I understand that this dissertation will be made available from the OhioLINK ETD Center and the Maag Library Circulation Desk for public access. I also authorize the University or other individuals to make copies of this thesis as needed for scholarly research.

Signature:

_____

Aspen W. Glaspell, Student   Date

Approvals:

_____

Dr. Kysoung Choo, Thesis Advisor   Date

_____

Dr. Pedro Cortes, Committee Member   Date

_____

Dr. Timothy Wagner, Committee Member   Date

_____

Dr. Jaejoong Ryu, Committee Member   Date

_____

Dr. Holly Martin, Committee Member   Date

_____

Dr. Salvatore A. Sanders, Dean of Graduate Studies   Date

ABSTRACT

Linear friction welding (LFW) is a solid-state joining process that is increasingly gaining interest in its use for bonding dissimilar metals. The parameters necessary for successful bonding are not well understood for various dissimilar metal combinations. Laser welding (LW) is also a solid-state joining process that has gained interest for joining shape memory alloys to other metals. Similarly, the parameters needed for bonding these dissimilar metals are not well documented. Understanding what parameters are necessary for joining is essential for advancing knowledge in this field. This thesis focuses on the development and validation of computational models to address this issue.

A 2D numerical and computational model was developed for the LFW, while a 2D thermal and a 3D structural computational model was developed for the LW. The numerical model was developed using MATLAB, while the computational models were developed using the finite element analysis software ANSYS Workbench. The models were validated with experimental data taken during the experimental welding. The results showed for LFW increasing frictional heat flux and pressure increased deformation, while for LW increasing laser power increased deformation and increasing thickness decreased deformation.

In conclusion, the aims of this thesis were successfully addressed, thus increasing understanding of both the LFW and LW processes. The work showed the implicit decoupled 2D models can capture results necessary for parametric and geometric studies. The work also has a deeper insight into the necessary process parameters needed for successful bonding on dissimilar metals under both linear friction and laser welding.

Acknowledgements

To my friends, colleagues, and the professors in the Materials Science Department at Youngstown State University (YSU), thank you for your support, guidance, and knowledge you have taught me. Immense appreciation goes to my academic advisor Dr. Choo for his invaluable guidance and mentoring; It was a pleasure learning under you.

To my family and friends, thank you for you love and support. I appreciate everything you have done for me, particularly I would like to thank my mother for encouraging me to start my doctorate.

To my friends at Taylor-Winfield, thank you for allowing me to use your welding machines to perform the experiments presented in this dissertation. A special thanks to Mr. Deley and Mr. Gaskill for your help and guidance in performing both the linear friction welding and the laser welding performed for this dissertation.

To Shania my lovely fiancée, thank you for your love, your support, for everything, especially the times you reassured me.

To God, thank you for giving me the strength, wisdom, and patience to achieve this accomplishment.

Table of Contents

List of Figures

List of Tables

1 MOTIVATION

Traditional fusion welding utilizes high energy input to produce weld pool mixing and solidify. Generally, the fusion welded metals result in defects including porosity, hot cracking and segregation. However, linear friction welding (LFW) is a solid-state joining process that utilizes friction heat to soften the workpieces and bonding by applied pressure [1, 2].

LFW was first patented by W. Richter in 1924 in England and 1929 in Germany [3, 4]. Currently the predominant commercial use of LFW is in aerospace, specifically joining aero-engine compressor blades to compressor disks, to form Blisks [1]. The benefits of LFW include:

- Due to the weld remaining in the solid-state, many of the defects associated with melting and solidification during fusion welding are avoided entirely [5, 6, 7, 8, 9, 10, 11, 12], for example pores and solidification cracks

    o Also, the distortion observed in the welded component is also reduced [13]

    o In comparison to more traditional welding techniques, residual stresses generated by linear friction welding can be considerably lower [14]

- Having lower peak temperatures than fusion welding, reducing intermetallic formation and allowing for a range of dissimilar materials to be joined [15, 16, 17]

- No need for filler metal, flux, or shielding gasses [13]

- The process can easily be automated, making the process both highly repeatable and independent of human influence [18, 19, 20]

    o Resulting in low defect rates [21]

- When used to fabricate preforms the material usage and manufacturing costs are reduced when compared to subtractive techniques [18, 19, 22]

While this process offers multiple impressive advantages compared to traditional welding methods, it also has specific limitations that must be considered for example:

- Cost and size of LFW machines are expensive compared to traditional subtractive manufacturing machines [1]

- The maximum weld size is directly limited by the size of the machine, with maximum sizes no larger than several hundred mm^2 [1]

- Currently this process is under-researched compared to other more common solid-state welding processes, especially when bonding of dissimilar materials is concerned [23]

2 PURPOSE

This study investigates two different phenomena under the umbrella of solid-state welding. Those phenomena being the effect frictional heat flux has on the structural stability of a part created by linear friction welding and the effect of laser power on the weldability of Ti-6Al-4V to Nitinol via laser welding. As mentioned in the Motivation, LFW is still an under-researched topic, especially LFW of dissimilar materials. The specific goals of this study are:

1. Perform welding tests to attempt bonding of Ti-6Al-4V to Cobalt Chrome Molybdenum via LFW and determine if welding was successful

2. Develop a 2D numerical simulation model to calculate the thermal profile during the welding process

3. Develop an FEA coupled thermomechanical model to simulate the welding process.

    a. Compare the thermal results of the simulation model to both numerical and experimental results to ensure the model is an accurate representation of the LFW process.

b. Using the output from the thermal portion of simulation model, simulate the structural deformation of the model during the welding process.

4. Perform welding tests to attempt bonding of Ti-6Al-4V to Nitinol via laser welding and perform analysis to determine if bonding was successful

5. Develop a 3D numerical simulation to calculate the thermal profile of during the welding process

3 LITERATURE REVIEW

This research work studied linear friction welding which is a solid-state welding process. Both the thermal and mechanical effects on materials used are unique for this type of additive manufacturing process. This chapter begins with an overview of the most used types of solid-state welding detailing how each method is performed, typical use case for each method, each method's advantages, and limitations. Linear Friction Welding is examined in-depth towards the end of this chapter as it is the technique used in this report.

3.1 SOLID-STATE WELDING

Solid-state welding (SSW) is an umbrella term referring to a group of welding processes that produce coalescence via the application of pressure without melting any of the joint components [24]. Within the category of SSW there are thirteen different welding processes. Those processes are coextrusion welding, cold welding, diffusion welding, explosion welding, forge welding, friction welding, friction stir welding, hot pressure welding, induction welding, pressure gas welding, resistance seam welding, resistance spot welding, roll welding, ultrasonic welding, and upset welding. Laser welding can also fall into this category so long as there is no filler material being introduced during the welding process. A recent addition to SSW is linear

friction welding. Linear friction welding falls within the broader category of friction welding along with friction stir welding. The most commonly used SSW methods are diffusion, resistance spot, ultrasonic, friction stir, and laser welding. Later in this chapter these methods along with linear friction welding will be explained in detail.

3.2 HISTORY AND TIMELINE OF SOLID-STATE WELDING

The concept of solid-state welding is quite ancient. The first recorded instance of solid-state welding occurred around 3000 BC when the Egyptians developed a process for heating iron ore over a flame while hammering it to produce sponge iron [4]. In more modern times, there have been a plethora of advancements. The first patent for linear friction welding was in the late 1920s [3], however there are very few records of its use at that time. Discussion on linear friction welding would not occur again until the 1960s when the process with being documented in the USSR [1, 25]. Explosion welding was developed in the US in 1960, CO_2 lasers were developed for cutting and welding in 1965 [4]. In the 1990s the aero engine industry advanced the understanding of linear friction welding for use in their industry [26]. In the 1990s, the Welding Institute (TWI) located in Cambridge, England developed the first commercial linear friction machine [27]. Current research focuses on the process of linear friction welding, primarily its use in the joining of dissimilar materials. Also, there is active research into how best to optimize simulations of this phenomenon.

3.3 DIFFUSION WELDING

Diffusion welding often abbreviated to DFW [24], occurs in the solid state when properly prepared surfaces are in contact under predetermined conditions of time, pressure, and elevated temperature. The applied pressure is set above the level needed to ensure essentially uniform

surface contact but below the level that would cause macroscopic deformation. The temperature

is generally well below the melting point. A filler metal, usually preplaced as an insert or plating,

may be used. The function of the filler metal generally is to lower the required temperature,

pressure, or time required for welding or to permit welding in a less expensive atmosphere.

Heating can be accomplished in a furnace, retort, or by resistance techniques. Pressure is applied

by dead weight loading, a press, differential gas pressure, or by differential thermal expansion of

the parts or of the tooling. The use of high-pressure autoclaves or differential gas pressure

techniques permits the welding of assemblies in which the joint surfaces are intersecting planar

surfaces. Uniaxial methods of applying pressure are limited to welding parallel planar surfaces

roughly perpendicular to the direction of load application. All techniques are essentially

mechanized and require appropriate equipment. Encapsulating or canning of parts for welding is

necessary when differential pressure techniques are practical and is useful when using other

techniques. A schematic representation of the diffusion welding process with the addition of an

interstitial layer can be seen below in Figure 3-1.
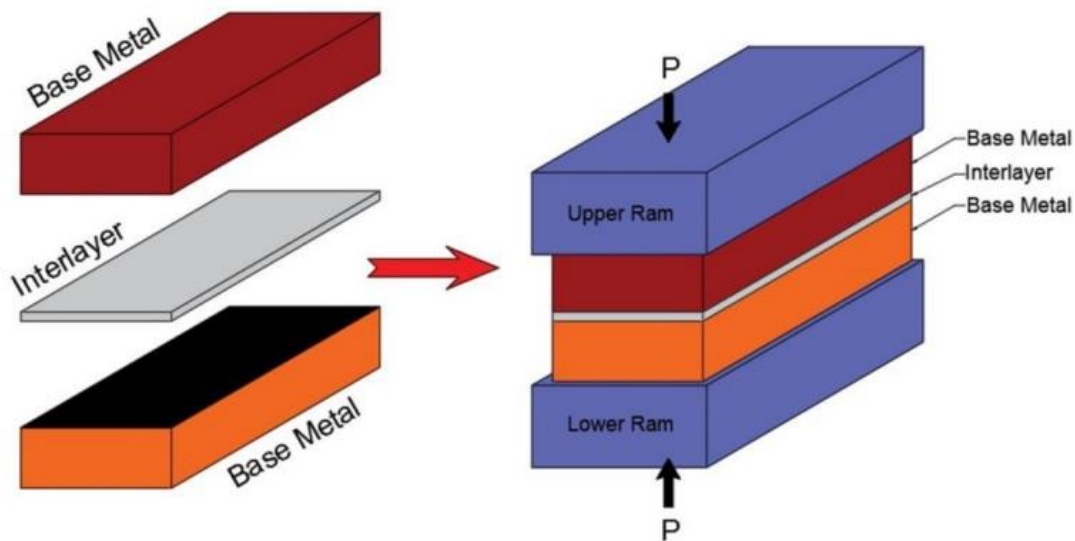
Figure 3-1. Diffusion welding diagram. [28]

Diffusion welding is almost exclusively used when the materials being welded have metallurgical changes in other welding process that would result in parts not having the specific material properties needed for their application. Historically the use of diffusion welding has been limited to the aerospace, nuclear, and electronics industries [24, 28]. While its applications are limited diffusion welding does have certain advantages unique to it. Generally, the use of diffusion welding is advantageous when the avoidance of metallurgical issues certain materials experience under fusion welding, for its ability to fabricate parts to net dimensions, maintaining joint corrosion resistance in welded specimens, and its ability to produce of thick parts with uniform material properties [24, 28]. The limitations of diffusion welding are largely economical. Diffusion welding's limitations include low productivity due to the time-consuming nature of the process, large amounts of preprocessing are required for successful bonding, requires highly skilled weld operators increasing labor costs, and the process extremely expensive with the cost per weld area typically ranging between $2000 and $4000 per square inch [24].

3.4 RESISTANCE SPOT WELDING

Resistance spot welding (RSW) is a solid-state process in which workpieces are bonding at specific points via the application of an electric current through both workpieces [24]. The resistance of the workpieces produces the heat needed for bonding while a compressive force is applied to the workpieces The combination of the heat and compressive force results in the two workpieces being joined. RSW is the simplest and most common type of resistance welding (RW) [29]. RSW is the most commonly used method to bond metal sheets within the automotive industry [29]. RSW dominates the automotive industry because the process has a low skill barrier, versatility, high operating speeds, repeatability, and its ease of inclusion in assembly

6

lines [30]. A diagram displaying the process parameters utilized in RSW can be seen below in Figure 3-2.
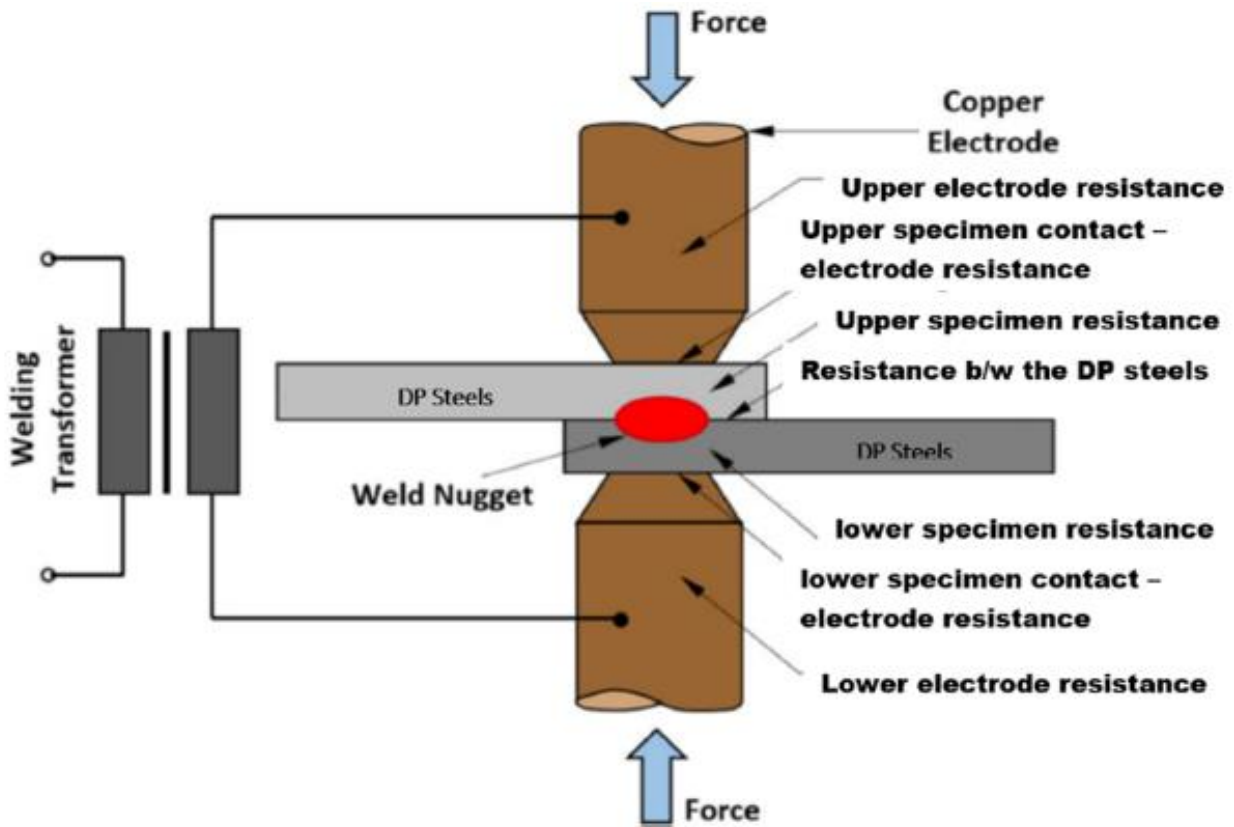
Figure 3-2. Spot welding diagram, showing typical process parameters. [31]

RSW has several advantages that make it a popular choice for use in the automotive industry. As RSW is a solid-state process, meaning that filler material is not needed, and it does not produce fumes making it an environmentally friendly process. Finally, the process is easily repeatable allowing for the process to be automated. RSW also has multiple limitations that have relegated its use to the automotive industry. For example, RW can produce warping which reduces the workpiece's fatigue strength [32], and its weld strength when producing discontinuous welds is less than that of other methods [33]. RSW is limited to welding sheets with thicknesses under 6 mm and the machines are expensive in comparison to traditional welding machines [33].

3.5 ULTRASONIC WELDING

Ultrasonic welding (USW) is a solid-state welding process where the weld is generated by the application of high frequency vibration energy while the workpieces are held in place under pressure [24]. USW can be used to shear lap joints, butt joints, and shear joints [34, 35, 36]. USW is used in many industries including the automotive, aerospace, medical, and electronics industries [34]. A diagram showing the typical features of USW for plastic bonding and metal bonding can be seen below in Figure 3-3.
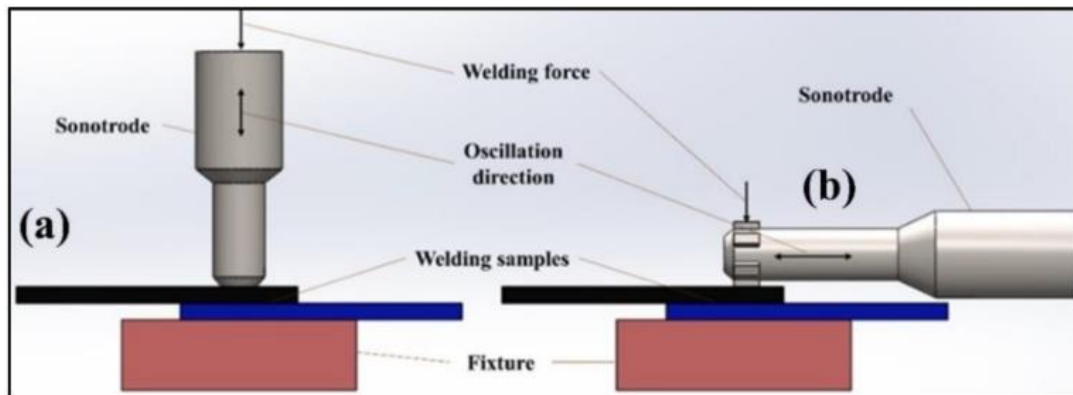
Figure 3-3. Diagram, showing typical features for (a) ultrasonic plastic welding and (b) ultrasonic metal welding. [34]

USW has multiple advantages which allows it to be utilized in many industries. USW is an incredibly fast joining process compared to other methods such as induction, resistance welding, and arc welding. Making it perfectly suited for mass production and automated processing [34, 37]. It does not require the use of filler material and it does not produce fumes or sparks making it environmentally friendly. Finally, the process only generates minimal surface damage during the welding process. Although USW does have some limitations. Critically, the process is limited to only shear, and overlap joints and there is a limit on the maximum weld thickness [34]. The process is sensitive to certain material properties including high stiffness,

8

hardness, and the damping factor which can limit how effective the process can be [34]. Its final major limitation is that the process produces substantial amounts of noise [34].

3.6 FRICTION STIR WELDING

Friction stir welding is often abbreviated to FSW [38]. FSW utilizes a rotating tool to weld two flat plates together, the choice of the specific tool is dependent on the materials that are to be welded [39]. This method joins materials by moving a rotating abrasive cylindrical tool along the interface to be welded. As the rotating tool moves there is a constant compressive force applied to it which ensures it remains in contact with the workpieces. The heat generated by this process is what bonds the two workpieces. FSW is primarily used by the aerospace and automotive industry as a manufacturing technique [40]. A diagram displaying typical parameters of FSW can be seen below in Figure 3-4.
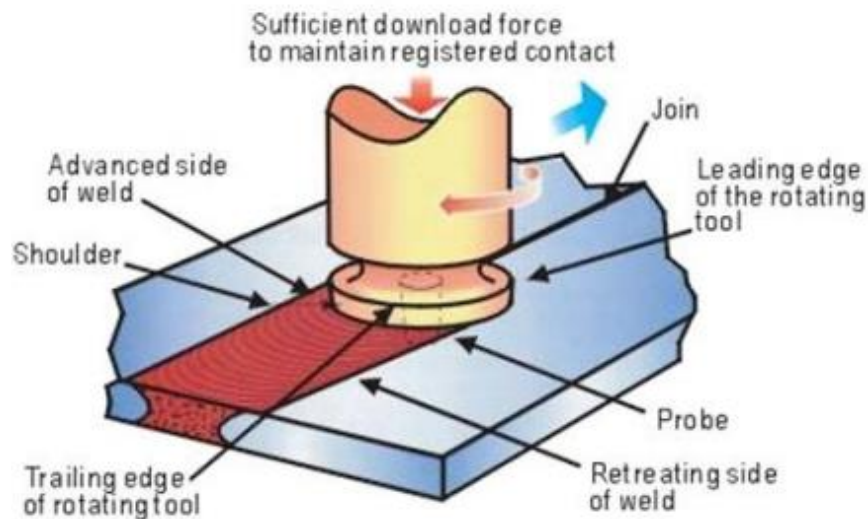
Figure 3-4. Friction stir weld diagram showing typical process parameters. [41]

FSW has certain advantages that make it quite desirable for specific applications. FSW produces welded joints that have a both fine microstructure and improved material properties compared to joints created via metal inert gas (MIG) or tungsten inert gas (TIG) welding [42].

9

This process does not require the use of filler material and it is both environmentally friendly and cost-effective [42]. Finally, FSW can weld aluminum alloys without the need of shielding gas, flux, or filler metal [40]. Although, the disadvantages of FSW must also be considered. Firstly, there must not be gaps along the weld interface otherwise those sections with gaps will not be joined [40]. Workpieces must always be locked in place during the welding process, and finally at the end of the process an exit hole will be left when the tool is elevated off the workpieces [40].

3.7 LASER WELDING

Laser welding abbreviated to LW [24], is a fusion bonding process in which a laser passes over two workpieces fusing them as it moves. LW is based on the principle of how matter and light interact, the process can be described in 4 steps [43]. First the workpieces to be welded absorb the laser at the point of contact between the laser and the workpieces. Next the laser energy is diffused into the bulk material via conduction. Afterwards the material near the laser point of contact begins to melt due to the heat generated. Finally, as the laser passes the workpieces the material quickly solidifies forming the weld. A diagram detailing typical features of laser welding can be found below in Figure 3-5.
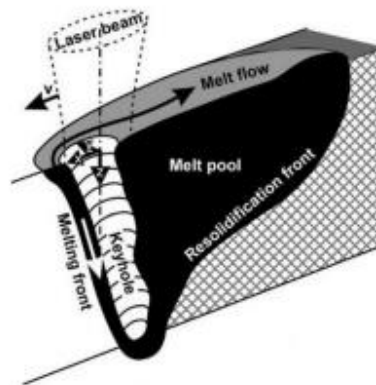
Figure 3-5. Laser weld diagram showing typical features. [44]

10

LW is most commonly used in the automotive industry, typically as an alternative to

RSW [45]. LW has many advantages which make it an attractive choice for SSW. For example,

the heat input is near the minimum necessary for fusion minimizing distortions [46]. Since LW is

a noncontact process there is virtually no tool wear, and it is an easily automated process [46].

Also, LW allows for a wide range of material combinations for joining [46]. Just as LW has an

impressive list of advantages, it also has numerous critical limitations that must be considered.

These limitations fall into three broad categories: material limitations, parameter constraints, and

cost. Under material limitations, it is noted that metals with high reflectivity and high thermal

conductivity such as aluminum and copper alloys can result in reducing the weldability of the

laser, also as LWs solidify rapidly welds tend to have increased levels of porosity and brittleness

[24]. The parameter constraints of LW are where the bulk of its limitations lie. The parameter

constraints fall into two categories, workpiece constraints and laser parameters. Regarding

workpiece constraints, the workpieces must be kept fixed relative to the laser beam's focal point

during the welding process [24, 47]. During the welding process the weld surfaces need to be

mechanically forced together, typically via a clamping mechanism [24]. Regarding laser

parameters, LW has a limited penetration depth of roughly 19 mm. Finally, as the cost of LW

equipment can be prohibitively expensive.

3.8 LINEAR FRICTION WELDING

3.8.1 Introduction

Linear Friction welding (LFW) is a solid-state joining process, in which one workpiece

oscillates relative to another while under a large compressive force [1, 48]. An example of this

can be seen below in Figure 3-6.
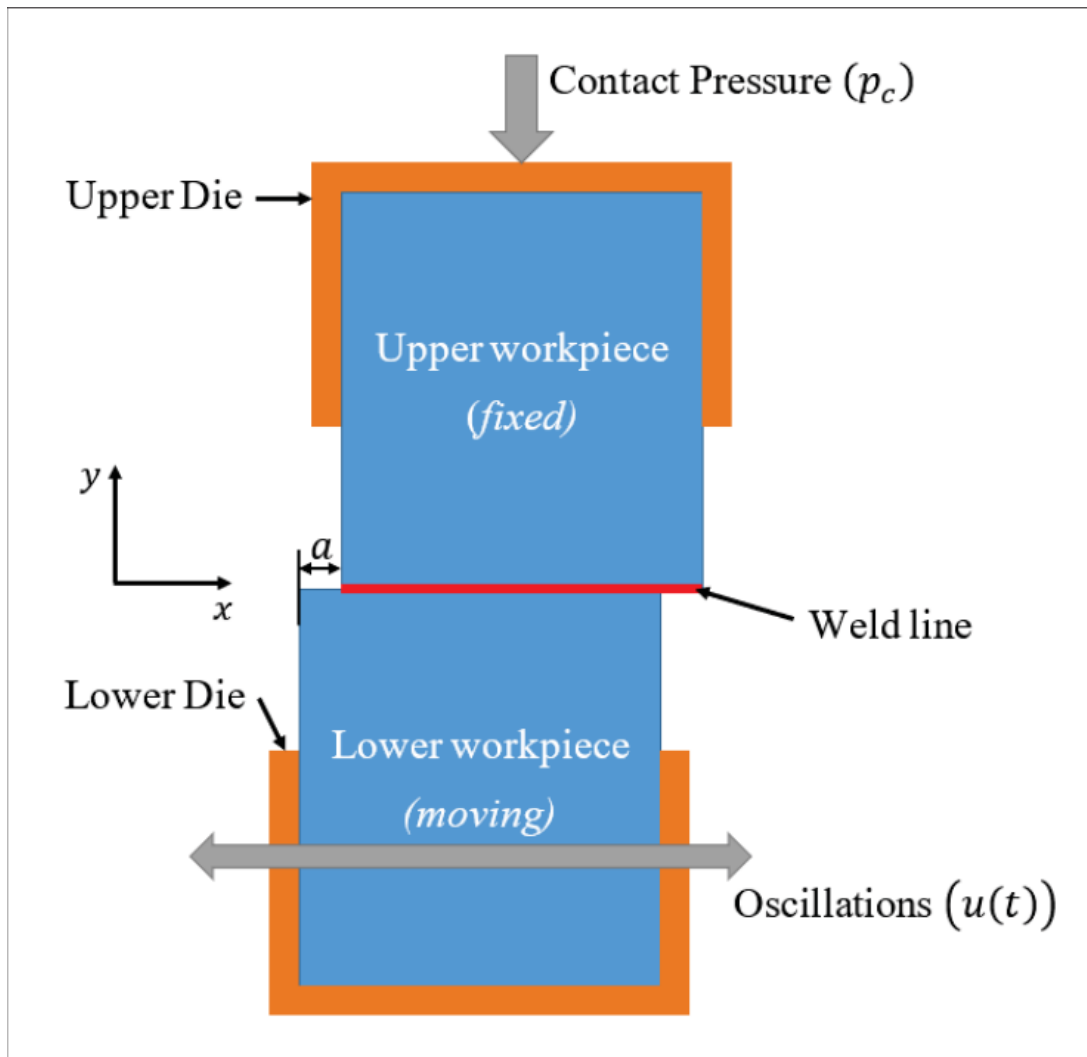
Figure 3-6. 2D Linear friction welding diagram, showing typical process parameters.

[49]

Although it is a continuous process, LFW is described as having four distinct phases [50].
Figure 3-7 gives a visual representation of each phase. Those phases are:

- Phase 1 – Initial phase. Contact between the two parts under pressure begins to
  occur. Initially both surfaces have asperities, along with this, heat generation due
  to friction begins. The true contact are increases as the asperities are worn away
  due to friction [51]. It is assumed that negligible burn-off occurs during this phase
  [52].

- Phase 2 – Transition phase. The true contact area reaches 100% and the heat affected zone (HZ) expands until phase 3. Along with this, large wear particles are expelled from the interface, and shear force begins to increase [53, 54]. Due to the expulsion of material burn-off begins to occur during this phase [55].

- Phase 3 – Equilibrium phase. The achievement of a quasi-steady-state condition occurs [56]. Extrusion of flash occurs which results in axial shortening [57]. The heat generated during this phase breaks and reforms bonds in the HZ causing more plastic material to be extruded.

- Phase 4 – Forging phase. The relative motion of the two parts is rapidly ceased, and a forging pressure is applied [58]. This final phase completes the weld formation.

There are a total of eight process parameters used for linear friction welding [41] . Those parameters are:

- Oscillation frequency

- Oscillation amplitude

- Applied force

- Burn-off

- Ramp-up time

- Oscillation decay time

- Forging pressure

- Forging time
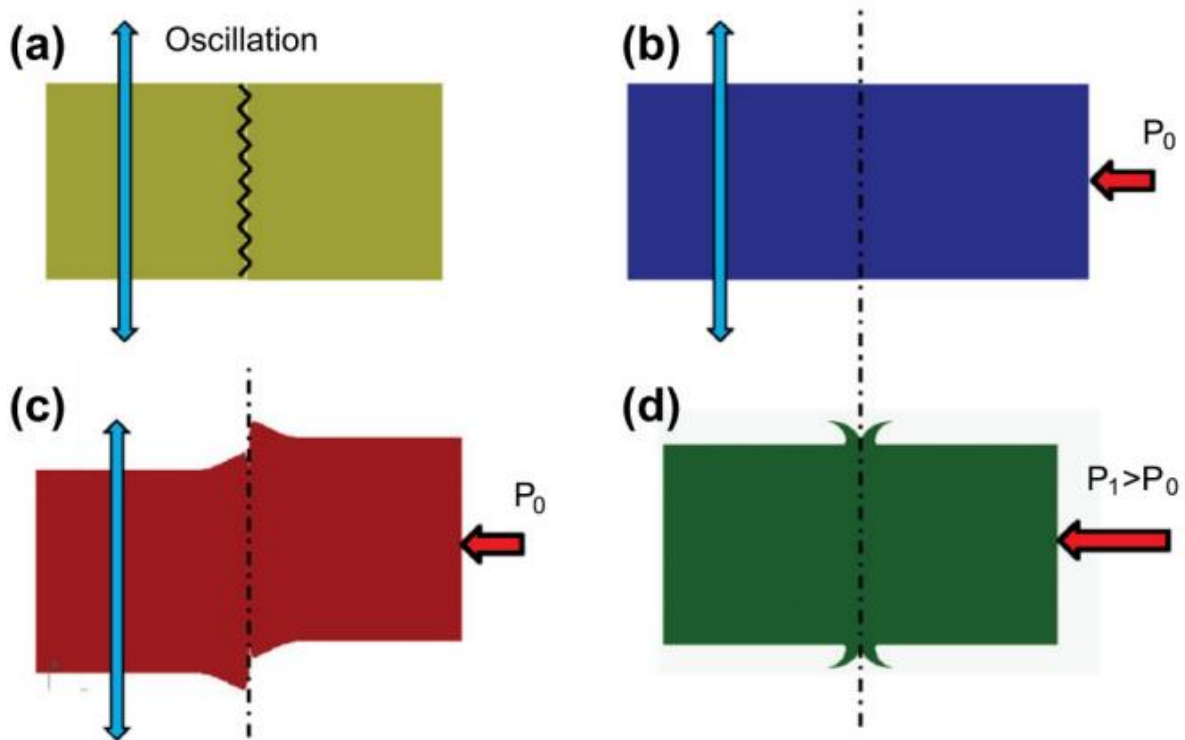
Figure 3-7. 2D Linear friction welding diagram, showing the four stages of the linear welding process. [49]

LFW is considered to be an "exotic" technology typically utilized for the manufacture of aerospace components [18, 19]. The process has been established as the industry standard for the fabrication of titanium alloy integrated bladed disks (Blisks) [19, 3, 59, 60, 61, 62]

The following sections will focus on more specific aspects of LFW. Including the materials used, common issues attributing to build failures.

3.8.2   Materials used in Linear Friction Welding

Each Solid-state welding process with the notable exceptions of friction stir welding and to a lesser extent laser welding have had certain rigid material property conditions which heavily limit their usage. Linear friction welding allows for the use of thermoplastics, ceramics, and metals, and combinations of these materials via dissimilar bonding. Although they cannot be in

powder form. The wide range of material combinations and the ability to avoid changes in

material properties due to filler material or liquification and re-solidification along the weld

interface is why research into LFW has gained steam over the years. This section gives an

overview of the materials typically used in LFW. As this research utilized metals specifically Ti-

6Al-4V and Cobalt Chrome Molybdenum, there is an extra emphasis on the metals used in LFW.

3.8.2.1   Thermoplastics

Thermoplastics are sometimes used in LFW. Their use is less common than that of metals

as they are poor thermal conductors, and their macromolecular structure reduces the

effectiveness of diffusion [63]. Thermoplastics that have been used in both LFW and FSW

include high density polyethylene (HDPE), polypropylene (PP), polymethylmethacrylate

(PMMA) and acrylonitrile butadiene styrene (ABS). As materials used in FSW are also capable

of being used in LFW, thus as FSW can bond dissimilar polymers [64], and polymers to

aluminum [65]. Therefore, LFW is also capable of bonding dissimilar polymers and bonding

polymers to aluminum.

3.8.2.2   Ceramics

Due to the extreme brittleness of ceramics, they are rarely used in LFW. There has been

literature on LFW of ceramics, but its predominant focus is on dissimilar bonding of application-

specific metals to ceramics.

3.8.2.3   Metals

Metals are by far the most common material used in LFW. This is due to them being

great thermal conductors and being effective at transferring heat via diffusion. Some of the most

common metals for LFW are [66]:

- Aluminum Alloys

- Brass

- Bronze

- Copper

- Copper Nickel

- Iron

- Magnesium Alloys

- Nickel Alloys

- Steel Alloys

- Titanium Alloys

They are also the most common materials used for dissimilar bonding via LFW. Some of the most common combinations of metals for dissimilar bonding via LFW are [66]:

- Aluminum to brass, nickel, magnesium alloys, steel alloys, etc.

- Carbon steel to bronze, cobalt, copper, nickel alloys, and steel alloys

- Stainless steel to copper nickel, titanium alloys, and zirconium alloys

These metals are popular due to their wide availability, cost, and use in industry. The metals listed have characteristics that allow for efficient heat flow, proper bonding, and applications in industry.

Since the materials used in the experiment and simulation are Ti-6Al-4V and Cobalt Chrome Molybdenum, the following sections are dedicated to reporting more specific material properties of said materials that are relent to this research. These metals are popular due to their wide availability, cost, and use in industry. The metals listed have characteristics that allow for efficient heat flow, proper bonding, and applications in industry.

3.8.3   Ti-6Al-4V (Ti-64)

Titanium alloys are used in many industries. Titanium alloys are often used as the material of choice for Blisks [67]. Ti-64 is also heavily utilized in the medical industry. Particularly as components of artificial knees, hip, shoulder joints, and bone fixators [68]. Ti-64 is so heavily favored for use in implants as it has excellent biocompatibility with bone tissue [69]. Titanium and more specifically Ti-64 are almost uniquely ideal for LFW as LFW excels at joining metals with high compressive and shear strength with low thermal conductivity [70]. Most material properties are a function of temperature and Ti-64 is no exception. The following plots, Figure 3-8 through Figure 3-14, show a graphical summary of both the mechanical and thermal material properties of Ti-64. The emissivity of Ti-64 was approximated to 0.40.
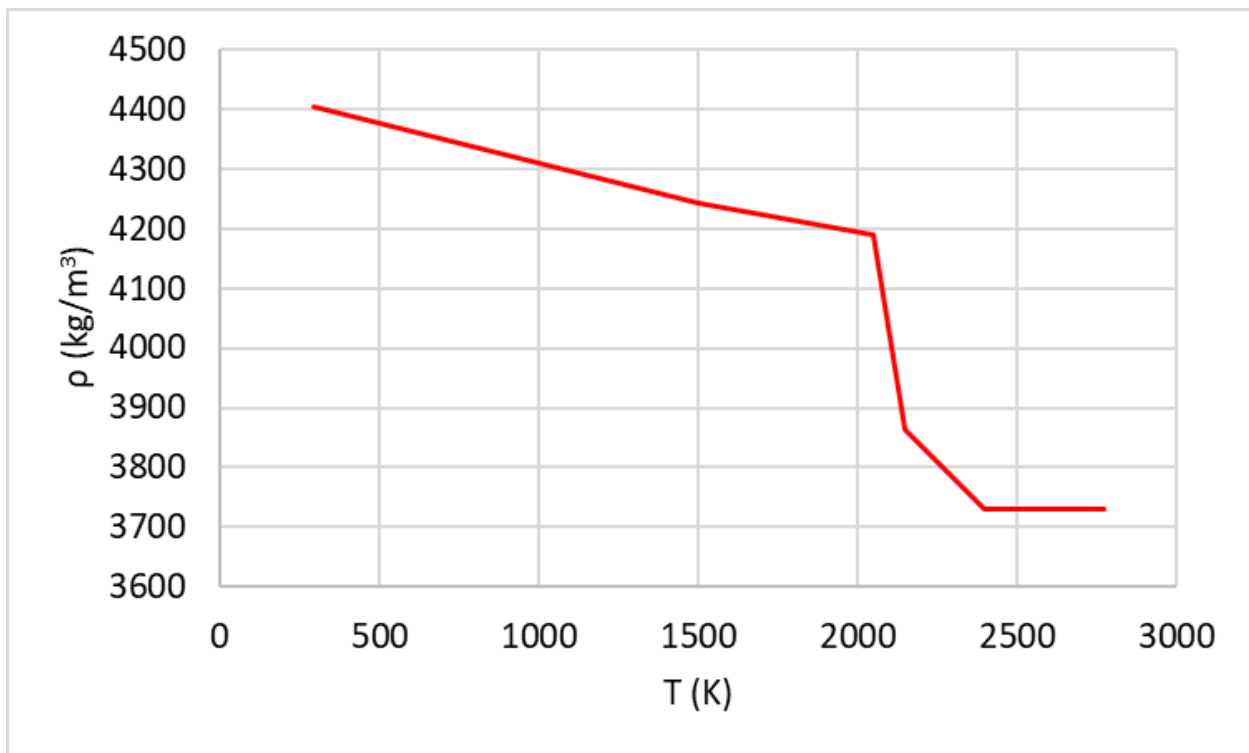
Figure 3-8. Density as a function of temperature. [71]

2
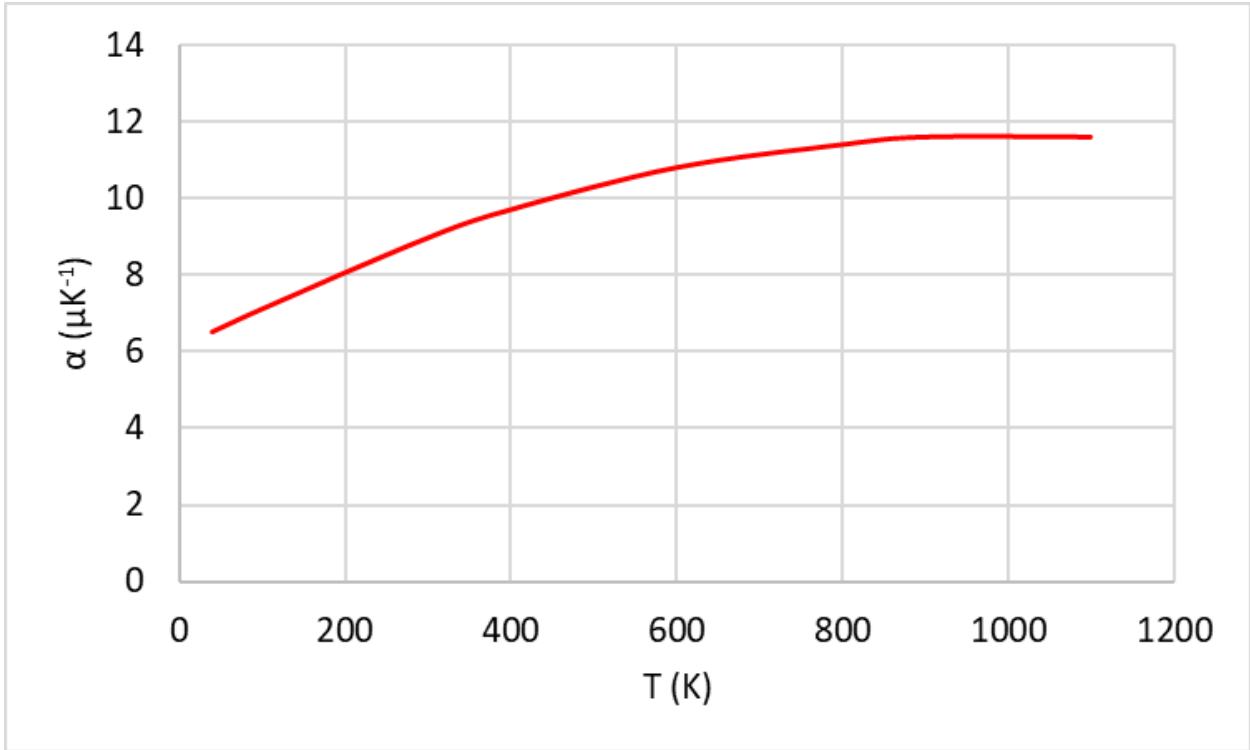
Figure 3-9. Coefficient of linear thermal expansion as a function of temperature. [71]
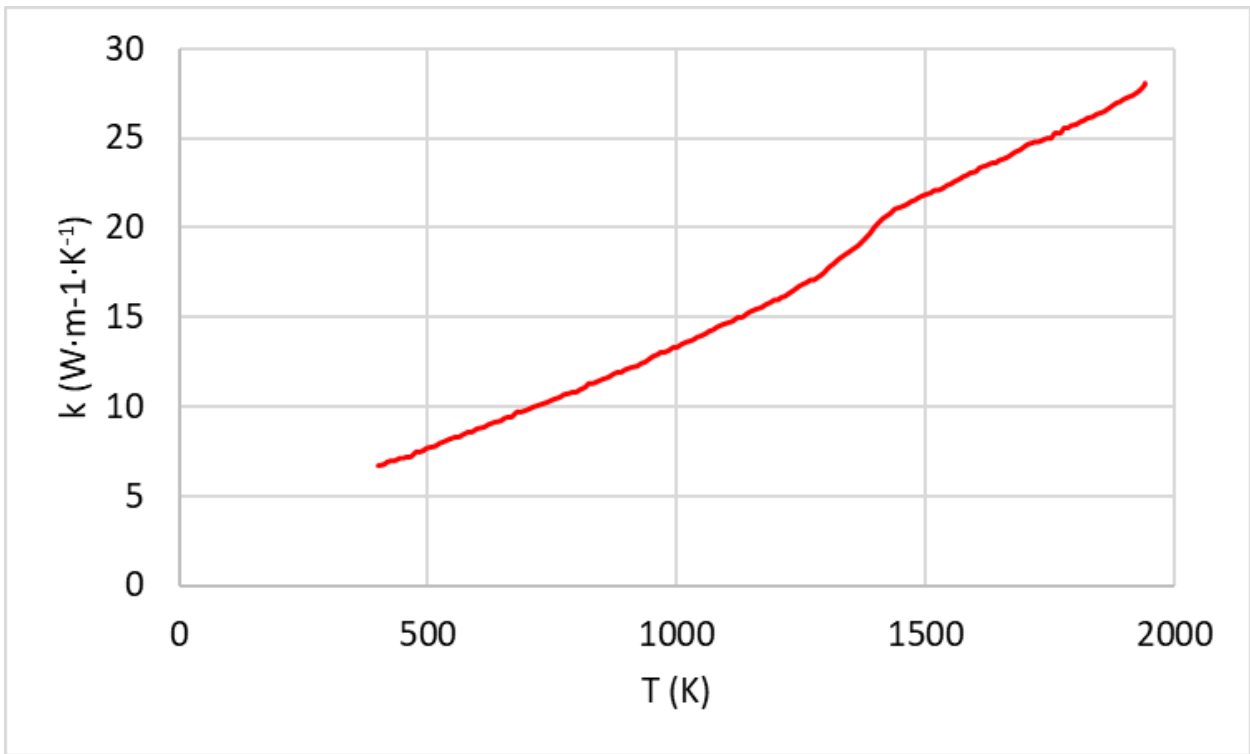
Figure 3-10. Thermal conductivity as a function of temperature. [72]
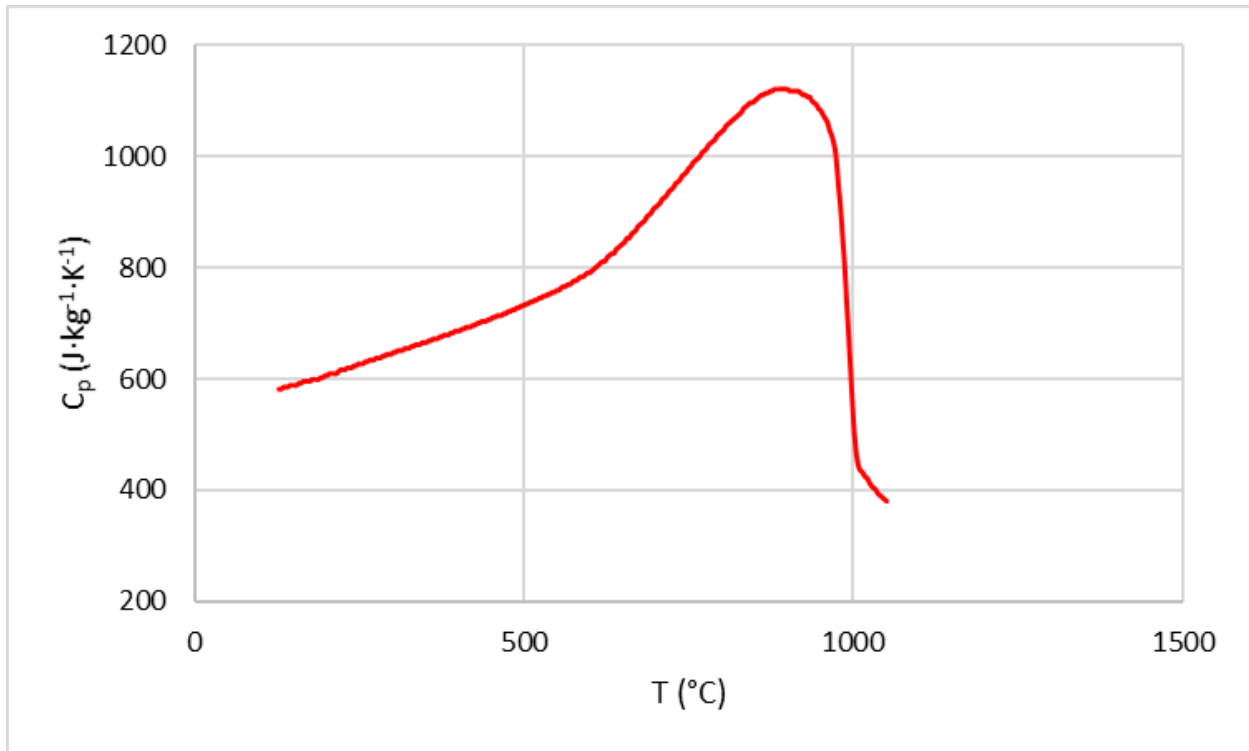
Figure 3-11. Specific heat capacity as a function of temperature. [72]
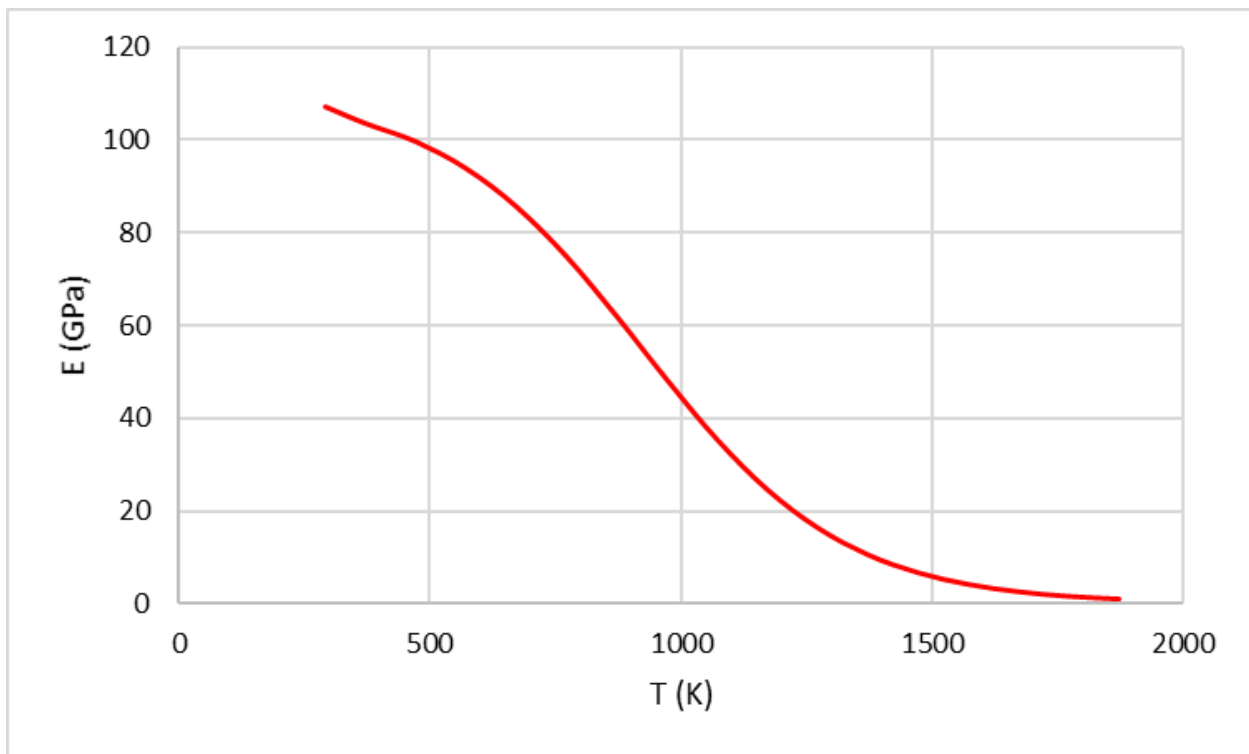
Figure 3-12. Young's modulus as a function of temperature. [71]
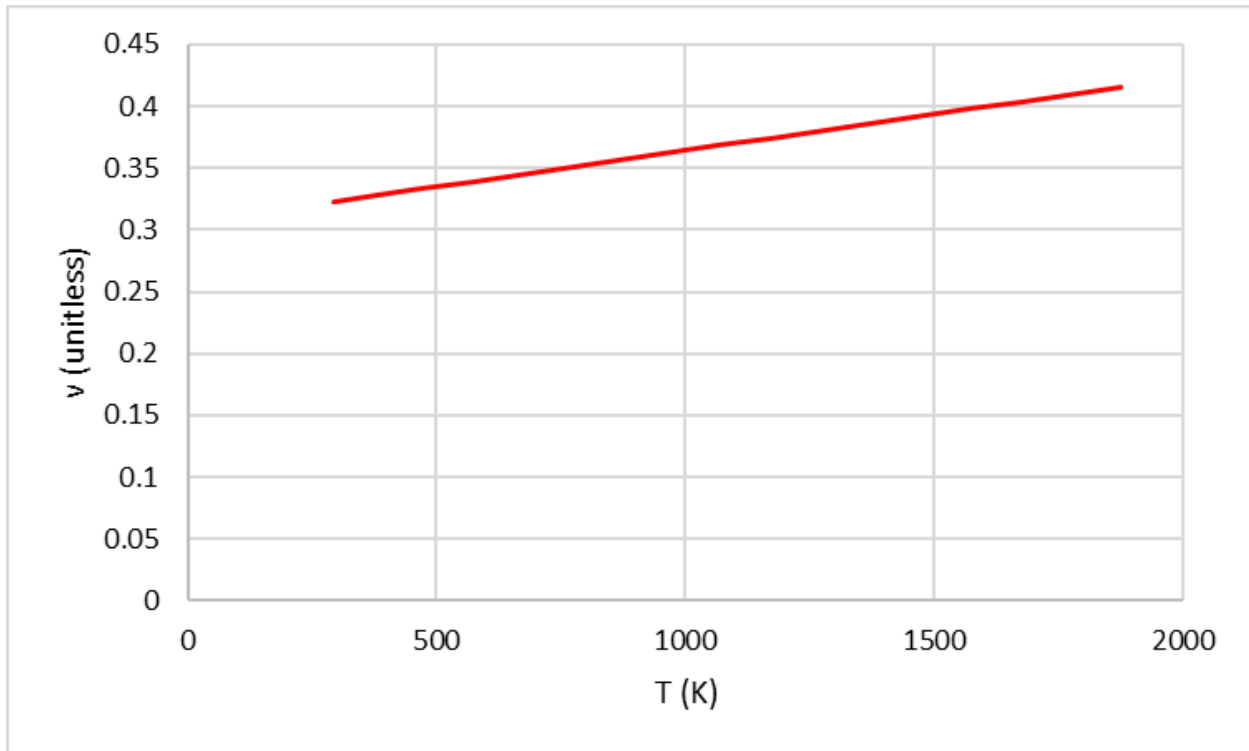
Figure 3-13. Poisson's ratio as a function of temperature. [71]
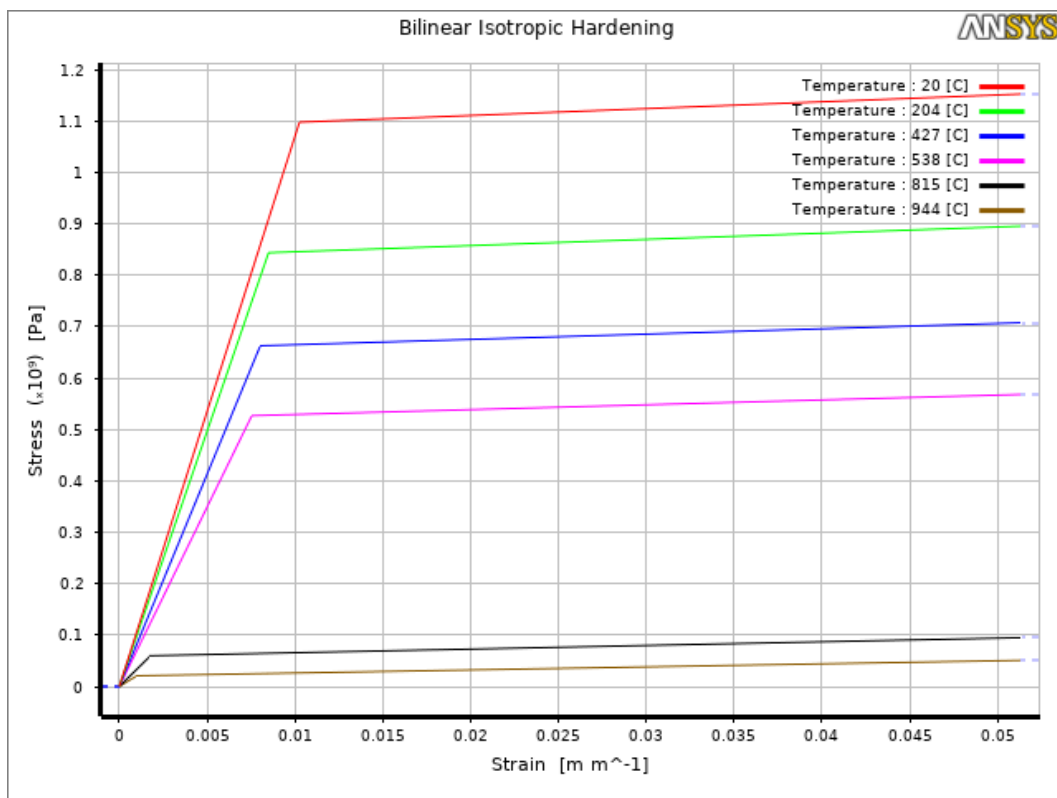
Figure 3-14. Bilinear Hardening as a function of temperature. [71]

3.8.4 Cobalt Chrome Molybdenum (CCM)

Cobalt Chrome Molybdenum (CoCrMo) is typically referred to as CCM. Due to CCM's high wear-resistance, corrosion resistance, and biocompatibility it is often utilized in the medical industry to produce medical implants [73]. Typically, in the form of artificial joints such as knee and hip joints. It is also utilized in the dental field where it is typically serves as the metal framework of partial dentures. Often when used in the medical implant industry CCM parts are made via casts, then machined to size [74]. Its uses in the non-medical applications are limited to areas where high resistance to both corrosion and wear are needed such as wind turbines and engine components. As currently there is virtually no literature detailing the temperature-dependent properties of CCM at elevated temperatures, the material properties of CCM were assumed to be constant. Known thermal and mechanical properties of CCM can be seen below in Table 1.

Table 3-1. CCM Material Properties

Material	CCM
ϱ (kg·m^{-3})	8500
k (W·m^{-1}·K^{-1})	13
C_P (J·kg^{-1}·K^{-1})	390
σ_Y (MPa)	958
σ_T (MPa)	1338
E (GPa)	210
ν (unitless)	0.3

3.9 Typical Failure Mechanisms for Linear Friction Welding

This section is dedicated to reporting research into LFW failure that helped shape the methods, models, and assumptions made in this research. To successfully design the experiment simulation model, it is essential to understand the different failure mechanisms intrinsic to LFW so that they can be avoided to the greatest extent possible. The different drivers of the weld

failure mechanisms detailed in this section include temperature, non-compatible materials and material properties, and process parameters. While this list is not all-inclusive, these topics highlight common design failures reported in literature reviews.

3.9.1 Plastic Buckling and Elastic Collapse

Plastic buckling occurs when the shear stress generated by the oscillating motion which is governed by the input frequency and amplitude are far greater than the shear strength and bending strength of the material. This causes the material to bend or buckle in the direction of motion at the point of failure. In contrast, elastic collapse occurs due to operator error. It is caused when one of the workpieces is not properly fitted into the LFW machine. As a result, when the friction pressure is applied the workpiece is blasted backward into its holding fixture causing failure. Thusly this prevents the welding process from occurring. A specimen with displaying plastic buckling can be seen below in Figure 3-15.

Figure 3-15. Specimen with plastic buckling.

3.9.2 Wrapping Deformation

Wrapping defects occur when one of the workpieces is too soft in comparison to the other workpiece. This difference results in the harder workpiece simply compressing the softer workpiece. This results in the weaker material wrapping around either itself or the stronger material while the stronger workpiece remains undeformed, resulting in a weld failure. This weld

failure is typically seen from stage 2 onward as stage 2 is when burn-off begins to occur. A specimen with displaying wrapping defect can be seen below in Figure 3-16.

Figure 3-16. Specimen with wrapping deformation along the weld interface.

3.9.3   Unsuccessful Bonding

Failure to bond can occur for a myriad of reasons. It can occur due to the presence of plastic buckling or wrapping defects. But it can also be caused by insufficient heat generation during the second phase of the LFW process or having too low of a forging pressure during the fourth phase of the LFW process. A specimen which did not achieve bonding can be seen below in Figure 3-17.

Figure 3-17. An example of a specimen that did not achieve successful bonding.

3.10 LFW – Finite Element Analysis

Numerical simulations for LFW fall into two categories: (1) mesh-free methods and (2) mesh-based methods. Finite volume and lattice Boltzmann methods are considered mesh-free

methods. These methods are typically used in fluid dynamic studies, and are rarely used in solid

structural studies that are typically modeled in solid structure numerical studies. Mesh-based

methods, i.e., finite element method (FEM), are the most popular choice for numerical analysis.

Their popularity is due to the fact that FEM reduces the problem to a limited number of unknown

variables discretizing the domain. This discretized domain is solved using a technique called

finite element analysis (FEA) which calculates approximate solutions to partial differential

equations. The solutions of these partial differential equations are based on dependent variables,

which are expanded into linear combinations of polynomial functions, which are defined over

elements. Most FEM software also allows for mesh customization of finite elements which can

allow for a better representation of the real-world process being modeled. As with virtually

everything related to computing, FEM also has become more powerful over the years since it

was first widely adopted. This has allowed users to solve more complex scenarios previously not

possible. Newer software has also given users the ability to complete a parametric optimization

study which will be critical if FEA is to be used to predict successful bonding in welding and to

help expand the body of knowledge on which materials can be bonding via LFW without the

overhead cost and waste of simply using trial and error.

Historically, most LFW parts were not vetted by FEM. The discovery of which materials

worked well under LFW, and the optimization of the process parameters used during the welding

process were found by trial and error. Recently, interest into the use of FEA for LFW parts has

grown along with the use of LFW is being expanded into more industries. Since the use of FEM

for LFW is relatively new, there isn't a large amount of research detailing complete methodology

on construction of simulation models that effectively couple thermal and structural results. As

such, researchers are still working out which methods offer the most realistic results that can

effectively couple thermodynamic history with accurate structural results. It should be noted that this can also be a time-consuming task, and most simulations employ a wide variety of approximations and assumptions which, while not always being reflective of the real-world process. are necessary for the simulation models to function. Although, the use of FEM can offer insight on the state of the system during the welding process which would be impossible to determine via conventional means [75]. The run time, processing power, and level of complexity required are the main reasons simulations are not used. There are different methods for predicting the thermal and structural characteristics of welded parts. These methods often create simplified elements to get a general estimate of idea of whether the weld will be successful and where problems are likely to arise during the LFW process. The simplified models typically incorporate constant material properties, simplified geometries, and simplified boundary conditions. While these simplifications significantly reduce the run time and processing requirements of a model, they also degrade the accuracy of the simulation. Therefore, it is essential to know how simplifying a model changes its results and to account for those changes.

For the purposes of this section, FEA can be classified by what type of analysis is studied. The two most common evaluations for LFW parts are thermal analysis and thermo-mechanical analysis. Typically, thermal analysis looks at how the weld generates heat throughout the workpieces to determine if the minimum temperature required for the weld to be successful was achieved. The thermo-mechanical analysis builds upon the thermal analysis and included the heat generation from the oscillating motion of the workpieces to generate a more accurate thermal history of the welding process and to determine the deformation generated by both the heat generated, oscillating frictional motion, and the forging pressure at the end of the welding sequence. This method not only allows for determining if the minimum temperature for

10

successful bonding was achieved, but it also allows for predicting the deformation generated by the welding process. The thermo-mechanical analysis accounts for all aspects of the LFW process, however it is also the most complicated and time-consuming of the two analyses requiring the knowledge detailed material properties at elevated temperatures in order to be successfully simulated.

3.10.1 FEM - Thermal Analysis

Improvements in numerical methods and increased computational speed have given rise to more accurate predictions of thermal histories for LFW processes. Typical FEM software used for this type of analysis is commercially available ANSYS, ABAQUS and DEFORM. Although, most literature tends to utilize ABAQUS. As LFW involves high-speed oscillation, convection plays a significant role in heat transfer during the process. Likewise, as the temperature of the workpieces is extremely large compared to that of the surrounding environment radiation also plays a significant role in the resulting heat transfer. And finally, conduction plays a critical role in the heat transfer as the two workpieces are being forced together under large compressive loads all throughout the LFW process. Often element birth/death is utilized to account for burn-off in these simulations, although the introduction of time step dependent birth/death of elements greatly increases the computation time required for said simulations.

Reference [76] collected thermal data during the experiment via the application of thermocouples which were placed at specific locations inside each workpiece. Along with this, the transverse force, burn-off, and power during the welding process was collected. A simulation (ABAQUS) was then generated to predict the thermal history and the power throughout the LFW process. This study also implemented element birth/death to account for burn-off. It is important to note that this study approximated the edges of the workpieces to be perfectly insulated as to

eliminate the effects of convection and radiation. Figure 3-18 details how the element birth/death was implemented. Figure 3-19 displays both the boundary conditions and mesh used, with a zoomed-in view of the mesh along the weld interface. Figure 3-20 displays the predicted thermal values at the end of the equilibrium stage.
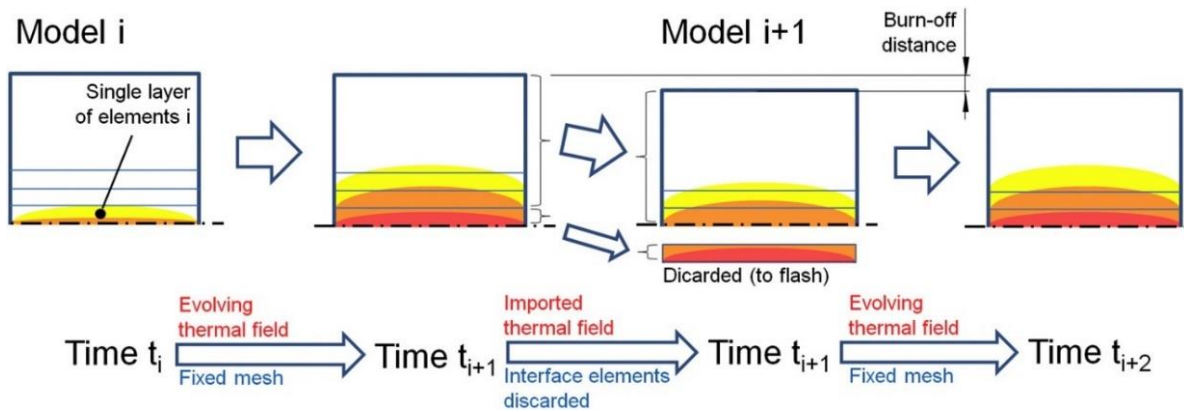
Figure 3-18. Schematic detailing the element birth/death at each time step. [76]
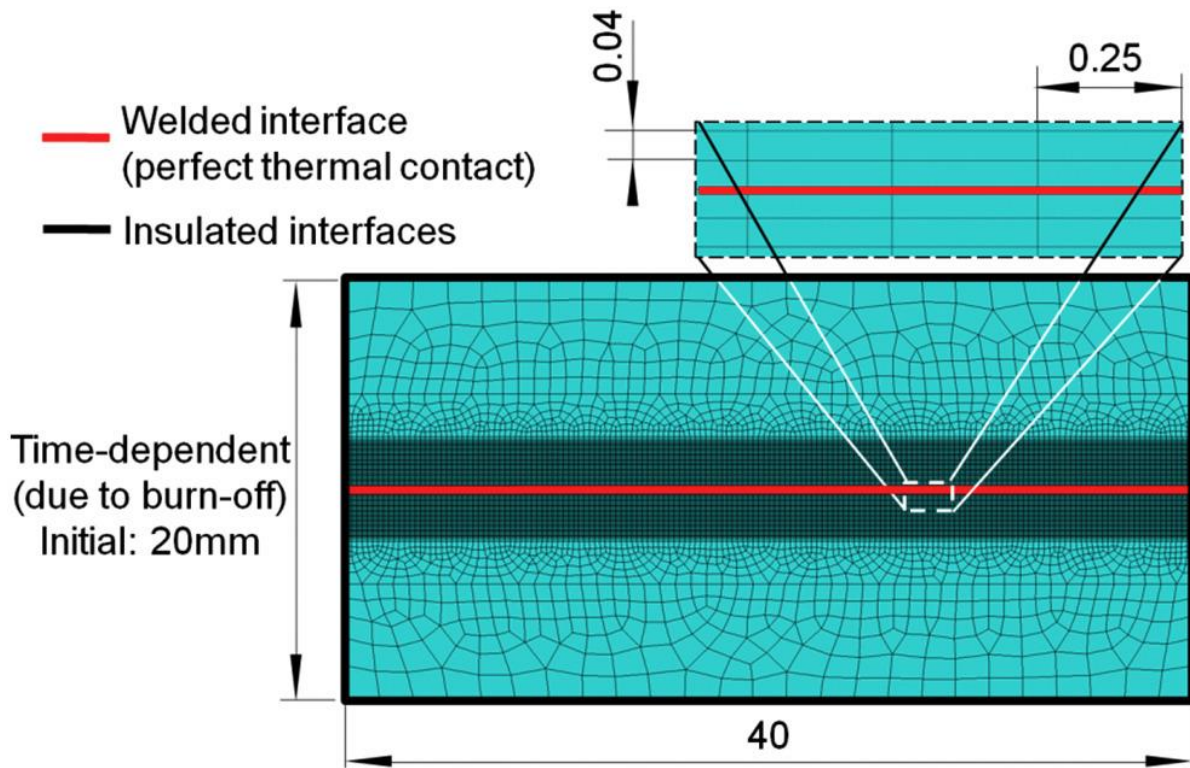
Figure 3-19. Boundary conditions and mesh utilized with a zoomed-in view of the mesh along the weld interface. [76]
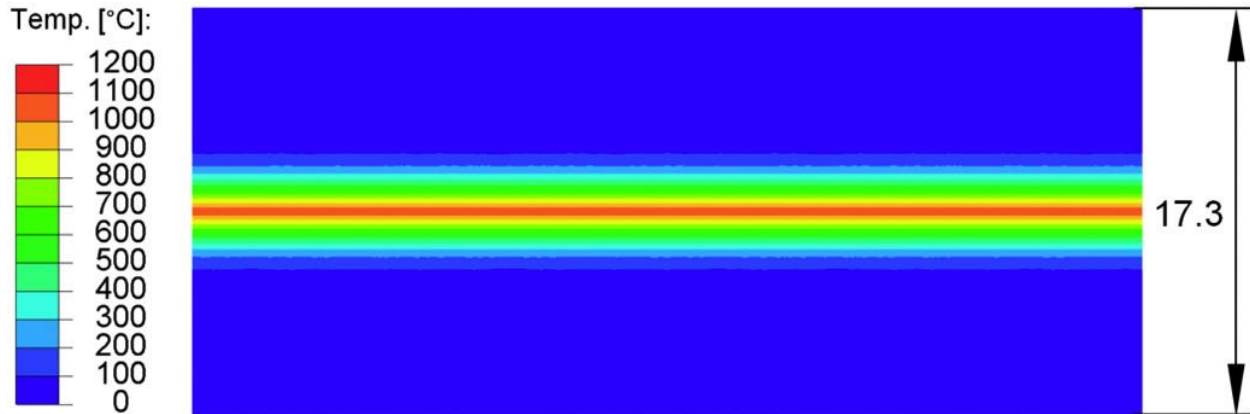
Figure 3-20. Thermal values at the end of the equilibrium stage. [76]

3.10.2 FEM - Thermomechanical Analysis

Reference [77] built upon the work of reference [76] to also simulate the plastic strain generated during the LFW process and compared those results to experimental cross-sections. It should be noted that the simulation model produced accurate results while having a fixed edge approximation. The mesh used for the structural analysis was identical to that used for the thermal analysis. The boundary conditions and mesh utilized by the model can be seen below in Figure 3-21.
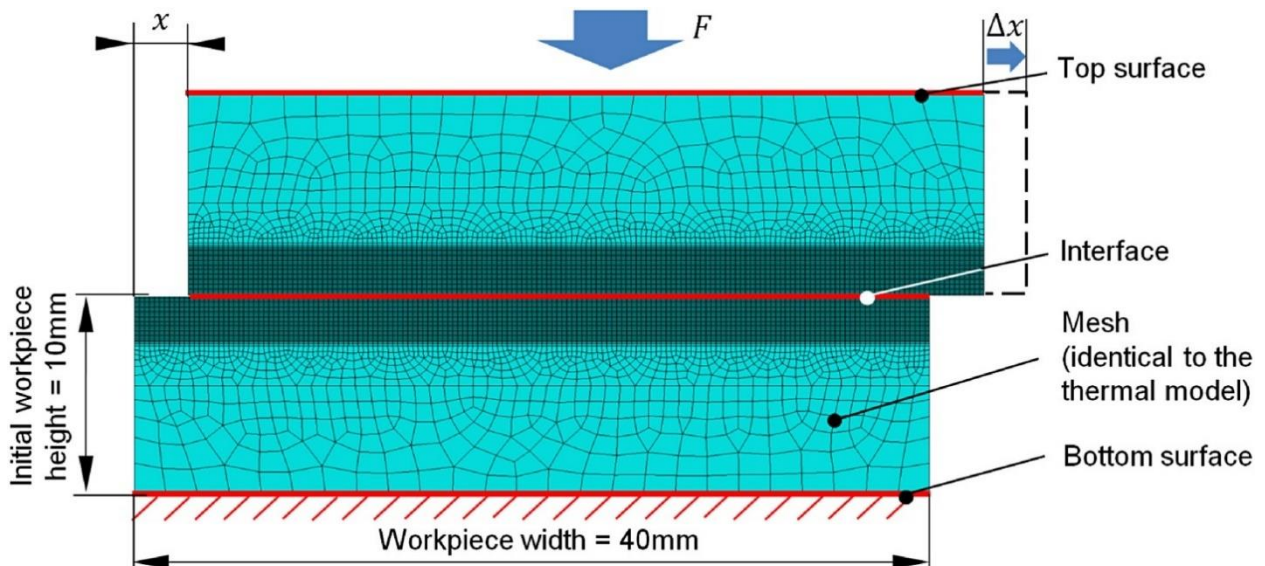
Figure 3-21. Boundary conditions and mesh utilized for the structural simulation. [77]

The work did not consider stress analysis and did not report results explicitly, instead showing results as a color map ranging from 0 to Max. The heat generated, equivalent plastic strain and a micrograph illustrating the results can be seen in Figure 3-22.
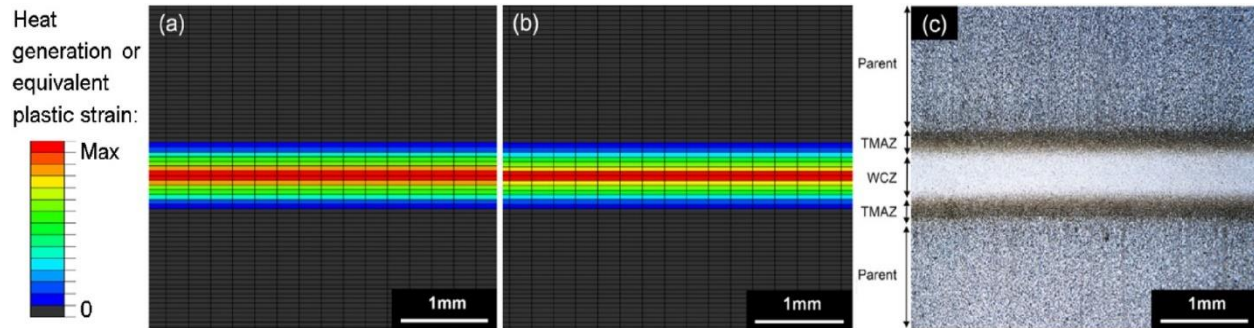
Figure 3-22. (a) Predicted heat generation per unit volume close the the weld interface; (b) corresponding equivalent plastic strain; (c) experimental cross-section showing weld zone (WCZ) and thermomechanically affected zone (TMAZ). [77]

Reference [78] performed multiple simulations for a variety of materials including GB 20 Chinese steel, Ti17, and Ti-64. All simulations were performed in ABAQUS. Although stress and deformation were simulated results were not given, instead the thermal values were superimposed onto the deformed models. To account for plastic deformation the Johnson and Cook plasticity model implemented into the model. It should be noted that the study did lay out the general computation times required for both implicit, explicit 2D analysis as well as 3D explicit analysis. The mesh used for the structural analysis was identical to that used for the thermal analysis. The boundary conditions and mesh utilized by the model can be seen below in Figure 3-23, followed by the thermal results at various times seen in Figure 3-24, and plots comparing the simulated thermal profile and burn-off rate to experimental data seen in Figure 3-25. The computation times for each method can be seen in Table 3-2.
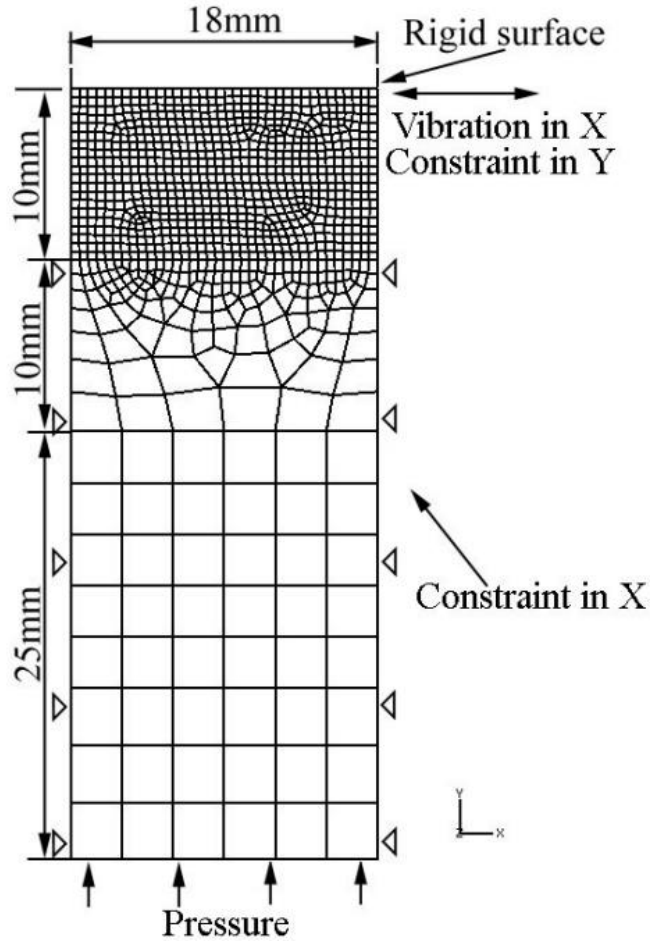
Figure 3-23. Mesh and boundary constraints utilized for 2D implicit model. [78]
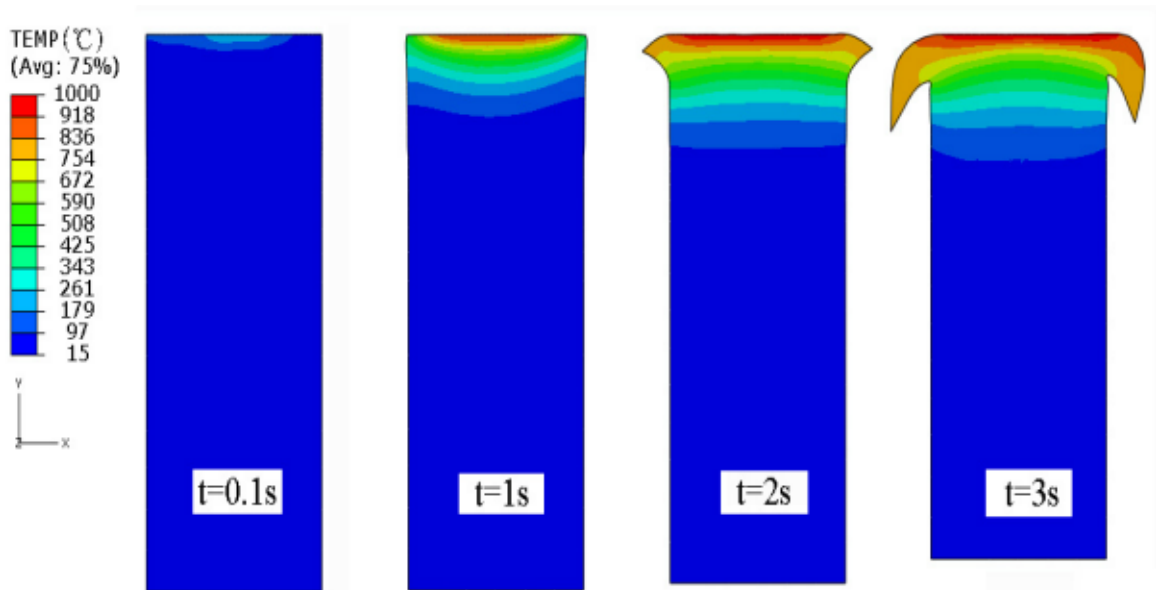
Figure 3-24. Thermal results at various times. [78]

15
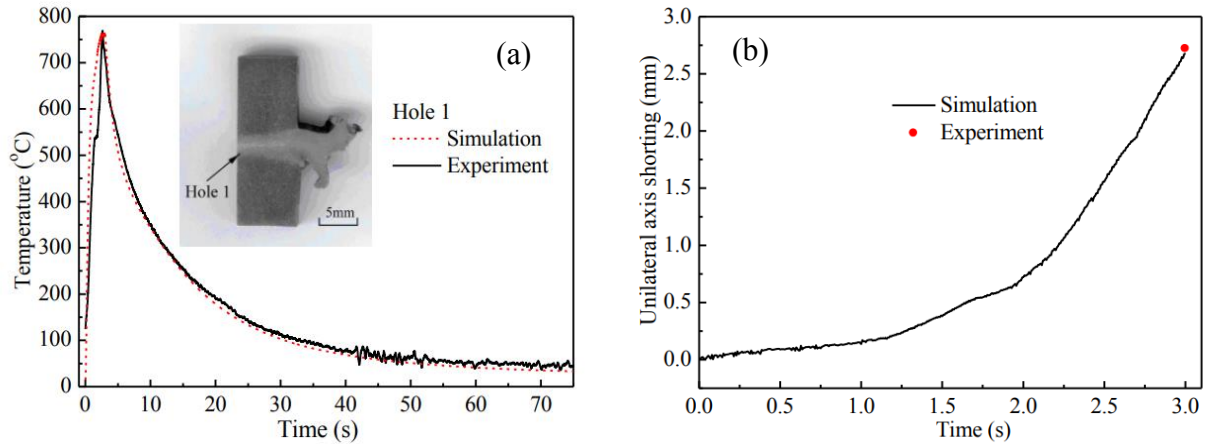
Figure 3-25 (a) Comaprison between simulated thermal profile and experimental thermal profile; (b) comparison between simulated burn-off and measured burn-off. [78]

Table 3-2. Comparison of comupatation times for each modeling method. [78]

Table 3   Comparison of different methods

Methods	Computation time, h	Accuracy	Problem solution	Specimen size
		Aspects		
2D explicit	4	Good	Temperature axial shortening	Limited
2D implicit	10	General	Temperature axial shortening	Limited
3D model	24	High	Temperature axial shortening residual stress	Unlimited

4   LFW RESEARCH

4.1   INTRODUCTION

This research sets out to analyze the thermomechanical properties of dissimilar butt welds of Ti-64 to CCM manufactured via the LFW process. This process is dependent on the material properties, heat generated by friction, and the forging pressure applied towards the end of the process. This work uses experimental results collected from References [2, 79] to validate the numerical models for the thermal analysis and structural deformation results. The validation of both the thermal values and the resulting deformation allows for this model to be the basis of future work which can incorporate parametric studies into the analysis.

16

At the time of the experimental design stage there was not much in the way of well-documented literature detailing the process parameters needed for successful dissimilar bonding of Ti-64 to CCM. As such, the experimental design was created with increasing burn-off distance under certain fixed parameters to determine the weldability of the dissimilar metals. The exact parameters used are detailed in the experimental section. Thermal imaging was incorporated to collect thermal data to help build an accurate thermomechanical simulation model. Thermal monitoring is a commonly used technique in the literature, although it is typically done via implanting thermocouples in the parent materials near the weld interface or by placing the thermocouples so close to the workpieces that the temperature gradient from heat loss from is negligible. As both methods are extremely time-consuming and prohibitively expensive, this work instead monitored the thermal history of the welding process via a thermal imaging camera. The use of cameras in LFW studies is not uncommon, Reference [80] utilized a high-speed camera to capture each phase of the LFW welding process for analysis.

This work demonstrates how essential detailed knowledge of material properties at elevated temperatures are as those properties are the primary factor in determining what types of approximations, and assumptions are necessary. It is also the one of the primary factors in deciding which analysis method to use for simulation.

4.2 EXPERIMENT

Both the workpieces were manufactured to ASTM standards [81, 82], with the Ti-64 workpiece following ASTM E8 guidelines and the CCM workpiece following the guidelines for wrought Cobalt chromium alloys for surgical implants. As such, both workpieces had a nominal diameter of 12.7 mm. A schematical representation of the workpieces displaying its nominal dimensions can be seen in Figure 4-1.
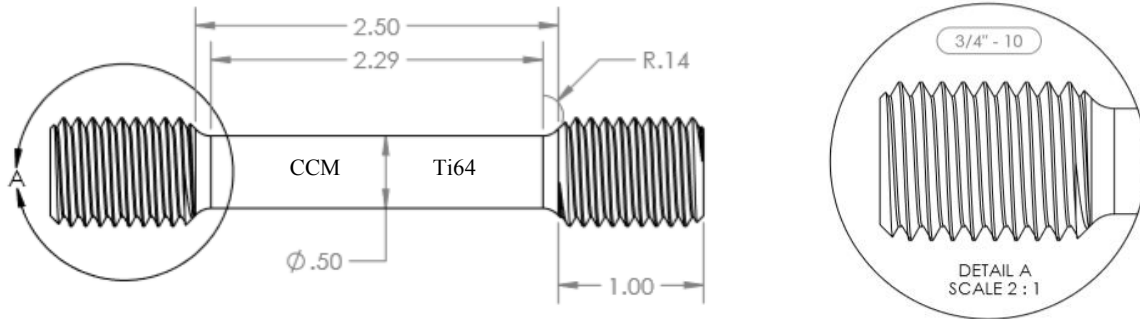
Figure 4-1. Schemtaic of workpieces showing nominal dimensions

Two devices were used to record the thermal history and change in process parameters during the welding process. The first device was an FLIR E60 thermal imaging camera was utilized to capture the temperature history throughout the welding process. The IR camera captured the thermographic profile along the weld interface and of the entire workpiece. The camera was paired with a computer running the FLIR Tools software package in order to record, save, and later analyze the thermographic history. The second device was the LFW machine itself, which recorded and plotted the change in the process parameters over time.

After the parts were welded, to measure the deflection of the along the weld interface each welded joint was measured with a micrometer and dial calipers to determine the macroscopic profile of the weld deformation. A table detailing the process parameters used for the experiment can be seen below in **Error! Reference source not found.** through Table 4-3. The amplitude and frequency of oscillation were chosen to minimize the chances of plastic buckling from occurring to excessive shear stress. Specimens were secured in a chuck fixture to ensure that elastic collapse would not occur. Figure 4-2 shows the variation in the process parameters for the first three tests captured by the LFW machine during the welding process.

Table 4-1. Phase I process parameters used in experimentation.

Test Set	Test Number	Frequency (Hz)	Amplitude (mm)	Pressure (MPa)	Burn-Off (mm)
			Phase I Process Parameters		
3	507	50	3.556	7	1.524
	508				3.048
	509				3.556
	510				4.064
4	511	50	3.556	7	1.524
	512				3.048
	513				3.302
	514				3.81

Table 4-2. Phase II process parameters used in experimentation.

Test Set	Test Number	Frequency (Hz)	Amplitude (mm)	Pressure (MPa)	Burn-Off (mm)
			Phase II Process Parameters		
1	412	45	4.064	52	1.524
	413				2.286
	414				3.302
	415				3.302
2	425	45	4.064	52	1.524
	426				2.386
	427				3.302
	428				4.572
3	507	50	3.556	207	3.048
	508				4.064
	509				4.064
	510				0.127
4	511	50	3.556	207	3.556
	512				3.302
	513				3.556
	514				4.064

Table 4-3. Phase III process parameters used in experimentation.

	Phase III Process Parameters				
Test Set	Test Number	Frequency (Hz)	Amplitude (mm)	Pressure (MPa)	Burn-Off (mm)
1	412 413 414 415	0	4.064	100	0
2	425 426 427 428	0	4.064	207	0
3	507 508 509 510	0	3.556	214	0
4	511 512 513 514	0	3.556	214	0

Figure 4-2. Plot of the weld process parameters during the weld process. [79]

Figure 4-3 (a) shows the thermography image along the midplane of the workpieces at the midpoint of the weld process at 1 s into the welding process. Figure 4-3 (b) shows an enhanced thermal image of the HAZ at a different point in time during the welding process. Figure 4-3 (a) also shows two data lines from which thermal profiles along the midplane at any time during the welding process could be extracted. A thermal profile at 1.2 s into the welding process was extracted and can be seen in Figure 4-4. From this plot it is clearly be seen that the decreases exponentially the as distance increases further away from the weld interface, this is consistent with what has been seen in similar studies. Figure 4-5 shows the thermal profile across the midplane at an earlier time in the welding process while Figure 4-4 shows the peak midplane thermal profile which occurs at 0.9 s. Figure 4-6 shows the maximum thermal development along the weld interface during the welding process. Emissivity was set to 0.87 in the FLIR software. Figures 4-4 and 4-6 were utilized to ensure that the simulation model was accurate to real world data.
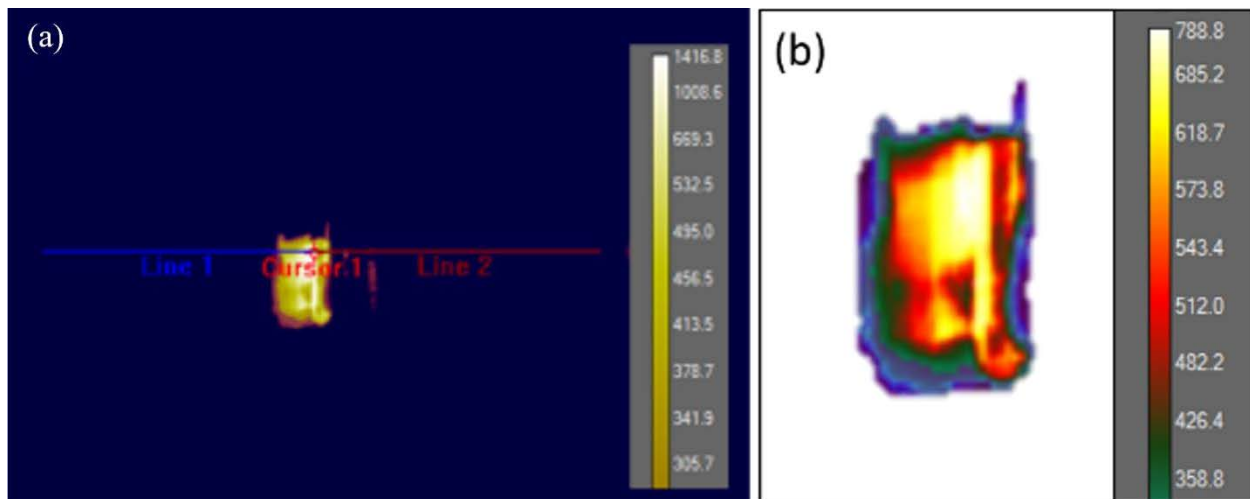
Figure 4-3. (a) Infrared imaging of experiment with a thermal horizontal profile and (b) enhanced thermal image of the HAZ during the welding process. [2, 79]
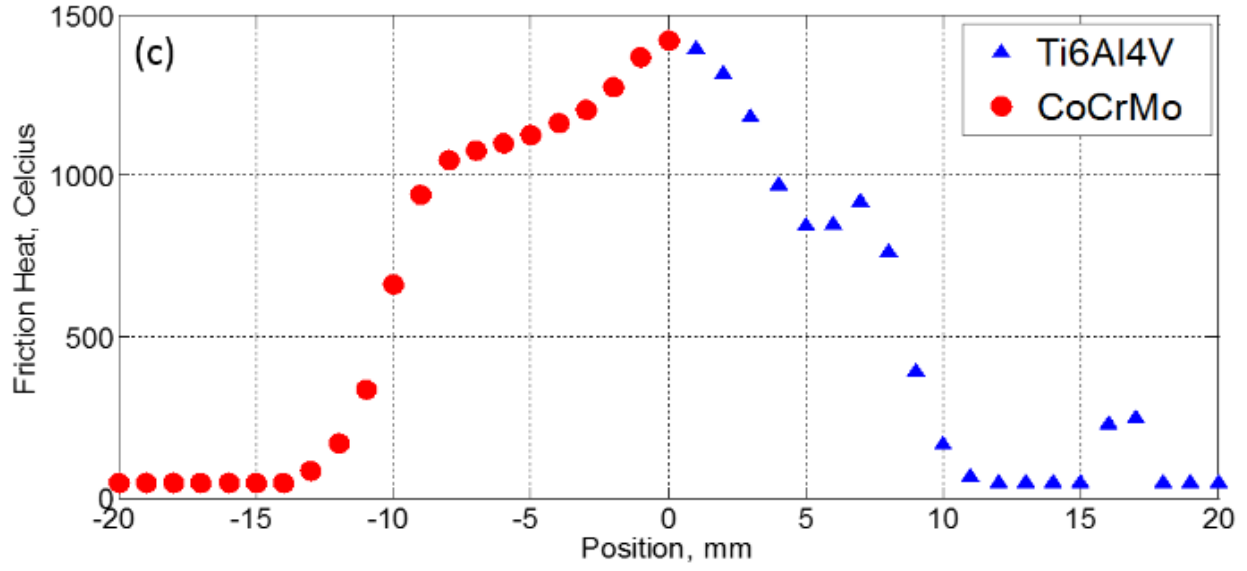
Figure 4-4. Maximum Temperature profile along the midplane of the two workpieces.

[79]
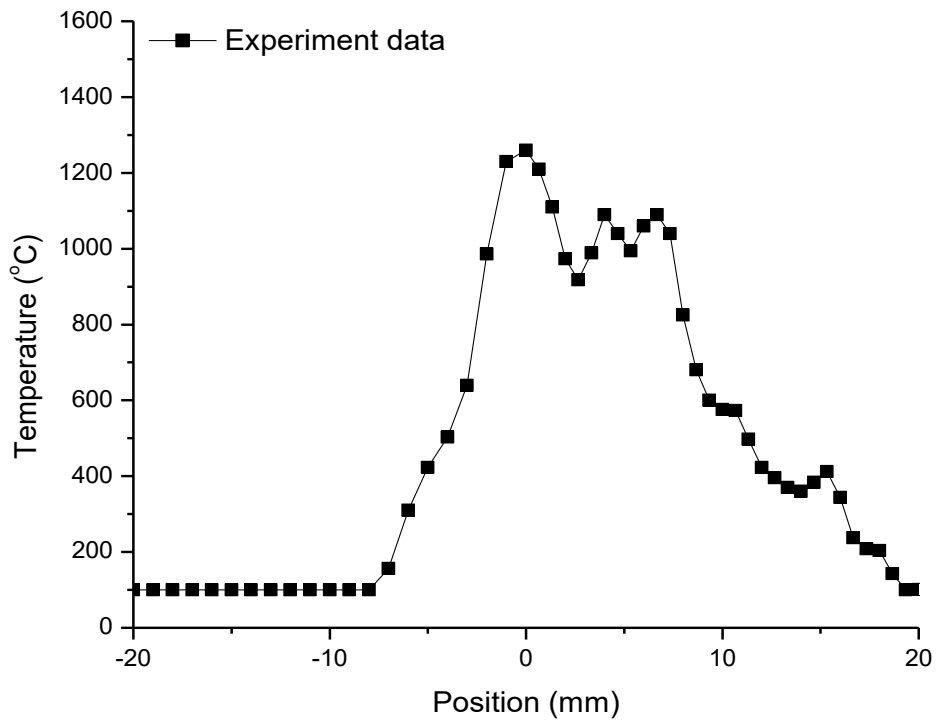
Figure 4-5. Temperature profile along the midplane of the two workpieces. [79]
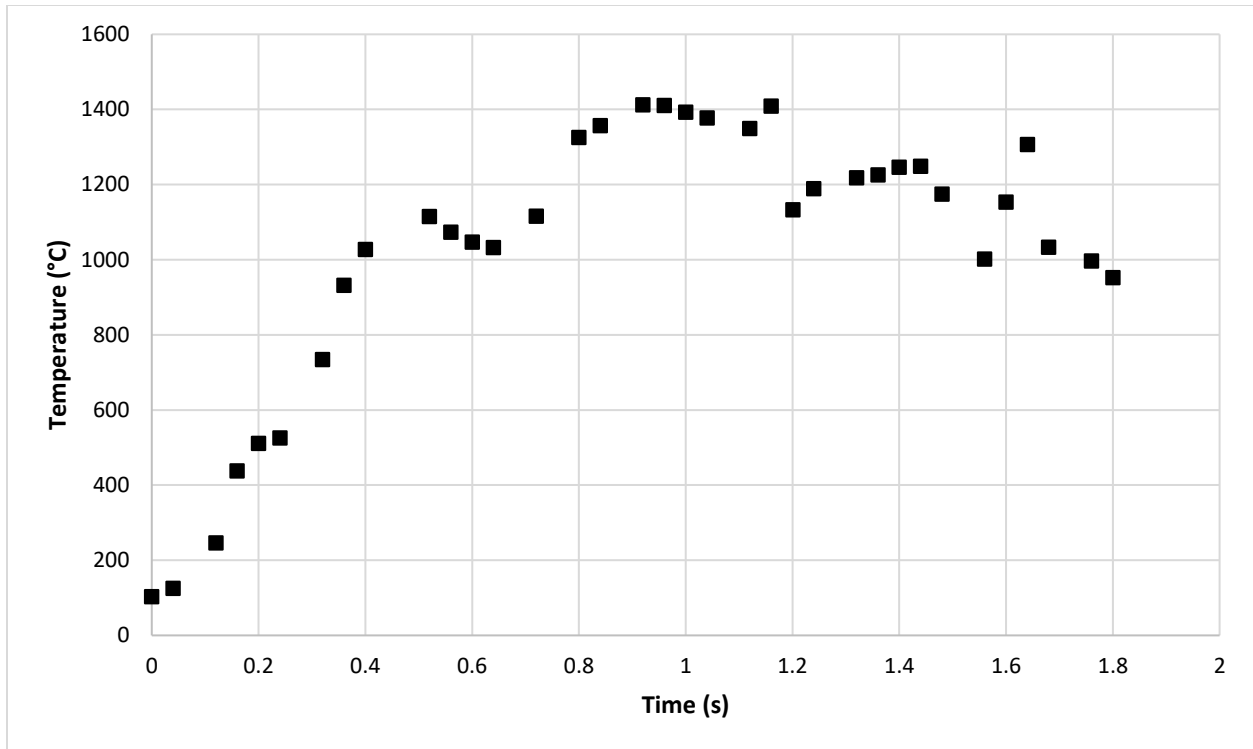
Figure 4-6. Temperature profile along the midplane of the two workpieces during the

welding process. [79]

4.2.1 Experimental Analysis

Tensile testing was performed on each sample from the test sets, with their results being seen in Figures Figure 4-7 through Figure 4-10 in accordance with the standards for Ti-64 and CCM specimens [81, 82]. The tensile testing indicated that true bonding was not successful as the ultimate tensile strength of the welded bonds were far below that of either parent material. The specimens from test set 1 were deformed, as such their tensile results were ignored in this study. It should be noted that test set 4 performed the best out of all the test sets far exceeding test set 2 and having improved results compared to test set 3. This suggests that with proper parameter optimization and heat-treated Ti-64, it may be possible to achieve true bonding with the fixed oscillation amplitude and oscillation frequency used in test set 4.

23
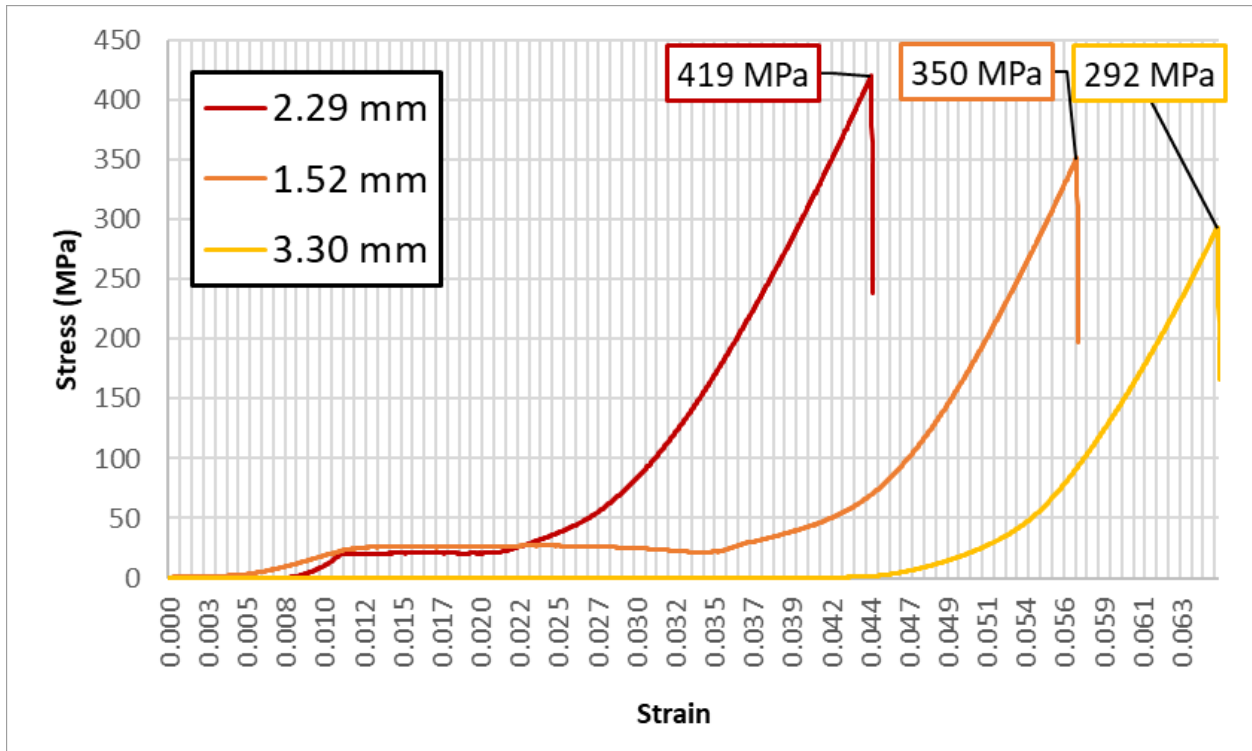
Figure 4-7. Tensile testing results from test set 1.
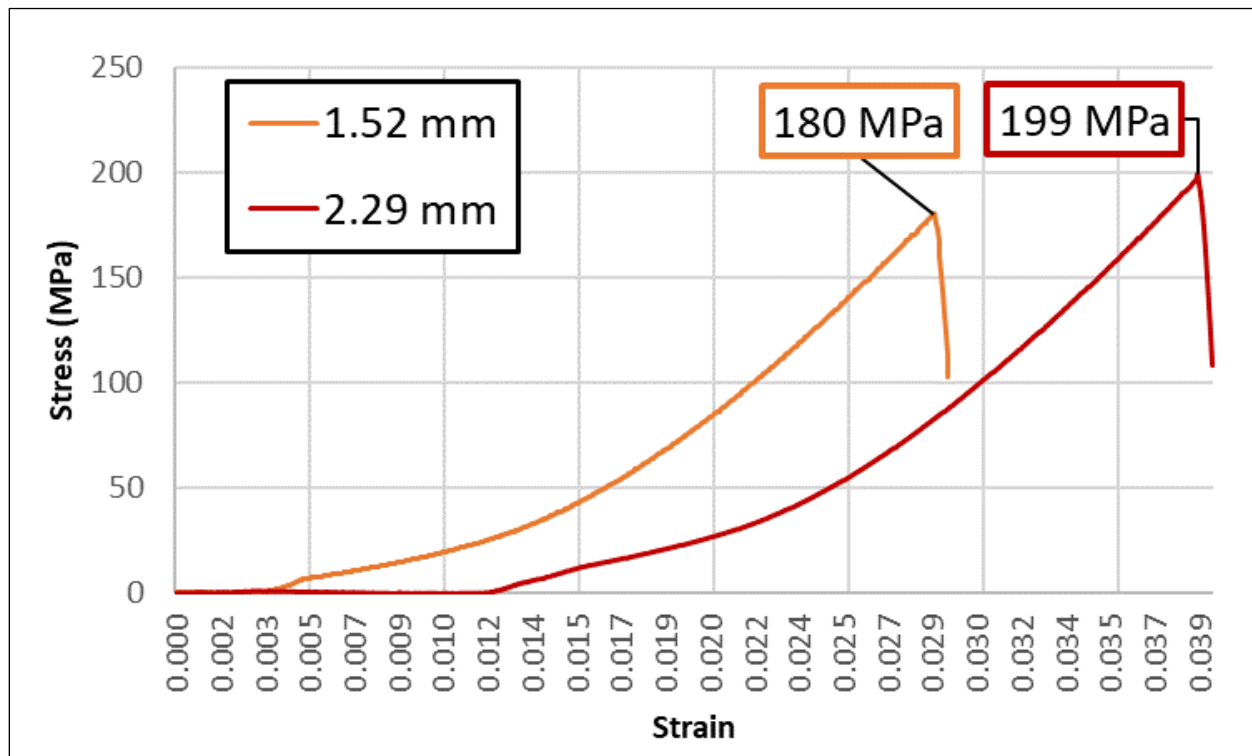
Figure 4-8. Tensile testing results from test set 2.
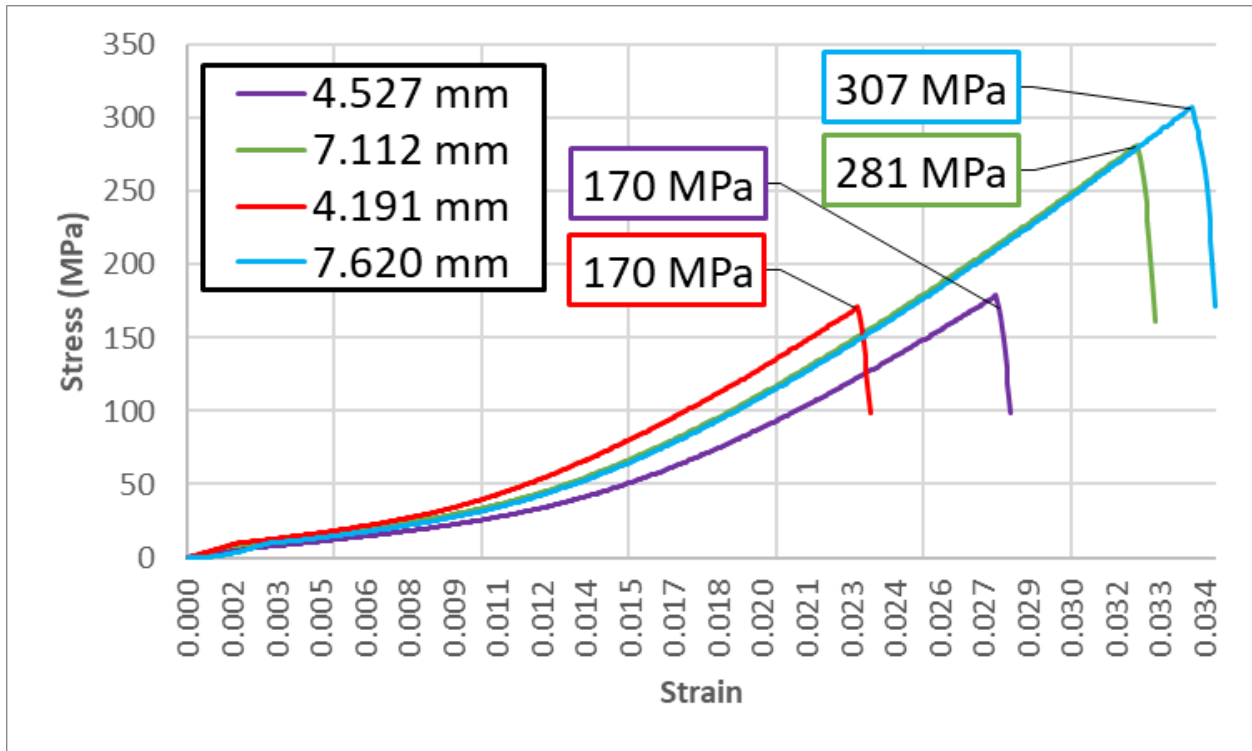
Figure 4-9 Tensile testing results from test set 3.
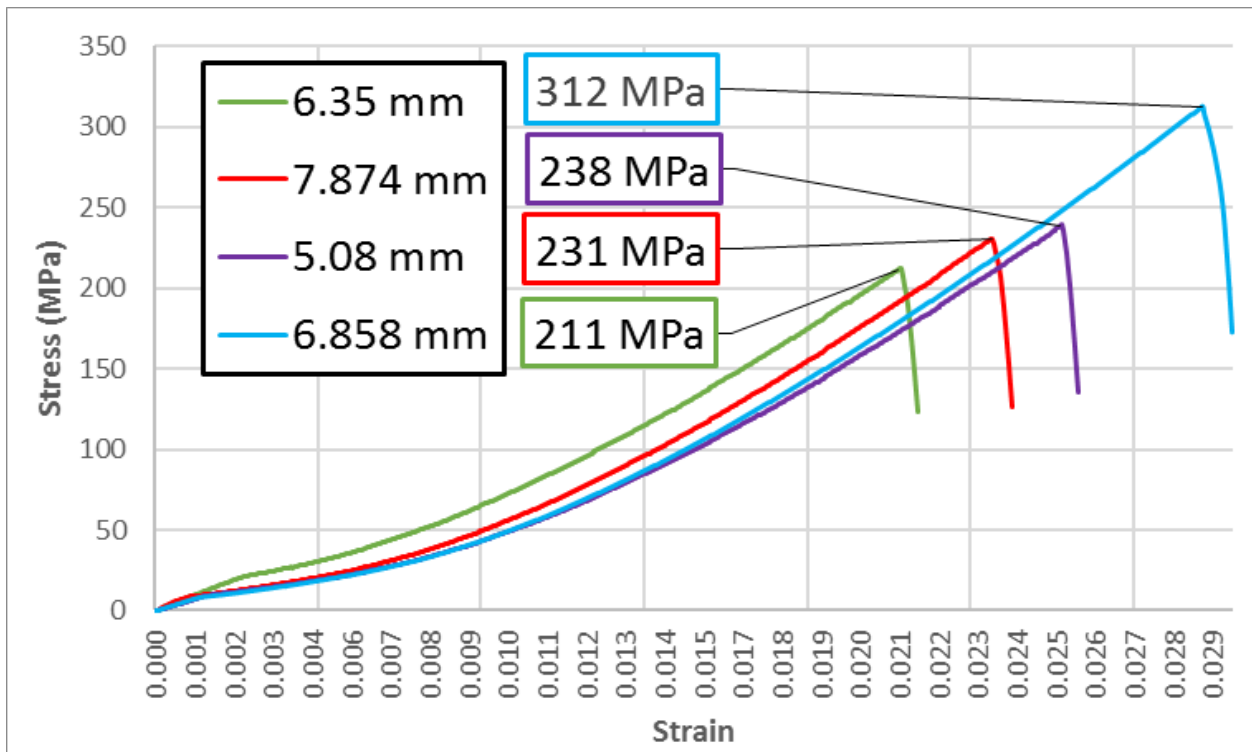
Figure 4-10. Tensile testing results from test set 4.

25

4.3   MATHEMATICAL TRANSIENT THERMAL MODEL

A 2D transient thermal model was developed to determine the temperature variation over the entire welding process. This model was based on previous research which utilized a 1D transient heat conduction model [58, 83].

The energy balance equation method seen in *Equation 4.1* was used to calculate the temperature profile over both workpieces throughout the welding process. This was completed by treating the two workpieces as a single 2D grid and applying the appropriate thermal properties to regions of said grid corresponding to each workpiece. Then the temperature of each element was determined using the energy balance method for each element in the grid. The energy balance equation is defined as follows:

$$mc_p \frac{dT}{dt} = hA_s(T - T_{amb}) + \varepsilon\sigma A_s(T^4 - T^4_{surr}) + kA_{contact}\frac{T - T_{contact}}{L} \qquad \textit{Equation 4.1}$$

where:

$m = $ mass, kg

$c_p = $ heat capacity of the workpiece material, $J/kg \cdot K$

$T = $ element temperature, K

$T_{surr} = $ temperature of the surroundings to which the element radiates, K

$T_{amb} = $ temperature of ambient air for natural convection, K

$T_c = $ temperature of neighboring elements in contact, K

$\varepsilon = $ emissivity of the workpiece

$t = $ time, s

$h = $ heat transfer coefficient of the workpiece, $W/m^2 \cdot K$

$k = $ thermal conductivity, $W/m \cdot K$

L = element width, m

A_s = surface area in contact with surrounding air, m^2

A_c = surface area between the element and neighboring elements, m^2

σ = Stefan-Boltzmann constant, $W/m^2 \cdot K^4$

Both T_{amb} and T_{surr} are assumed to be constant and these temperatures are associated with the top and bottom edges of the grid. As the size of the elements is constant throughout the welding process the surface area A_s is constant. The heat transfer coefficient was approximated to that of stagnate air over a flat plate as the oscillation amplitude is small in relation to the length of the workpieces. The change in time dt was chosen as a constant value. To ensure that the energy balance equation would converge given the chosen dt, a convergence check was performed. The convergence check was an equation that would validate that convergence will occur in a given direction so long as the value of the equation was less than 0.5. The convergence validation equation was broken into three equations for each direction criteria. The convergence validation equations are as follows:

$$r_{n,x} = \alpha \frac{dt}{dx^2} \qquad\qquad \textit{Equation 4.2}$$

$$r_{n,y} = \alpha \frac{dt}{dy^2} \qquad\qquad \textit{Equation 4.3}$$

$$r_{n,x,y} = \alpha \frac{dt}{dx \cdot dy} \qquad\qquad \textit{Equation 4.4}$$

where:

n = integer noting which workpiece is being checked

x = x direction

y = y direction

$$\alpha = \frac{k}{\rho \cdot C_p} = \text{thermal diffusivity}, \ m^2/s \cdot K$$

$dt = $ change in time, s

$dx = $ change in distance in the x direction, m

$dy = $ change in distance in the y direction, m

Equations 4.2 through 4.4 are used to ensure that the chosen values of dt, dx, and dy will allow Equation 4.1 to converge to a solution. Equation 4.1 is used to iteratively calculate the thermal profile along the weld interface. This thermal profile is validated by the experimental data in Figure 4-6.

4.3.1 Mathematical Transient Model Results

The results from the thermal transient model for a 2D radial symmetric cross-section of the welding process is shown in Figure 4-11. Figure 4-12 shows the comparison between the experimental thermal profile and the thermal profile generated from the numerical model.
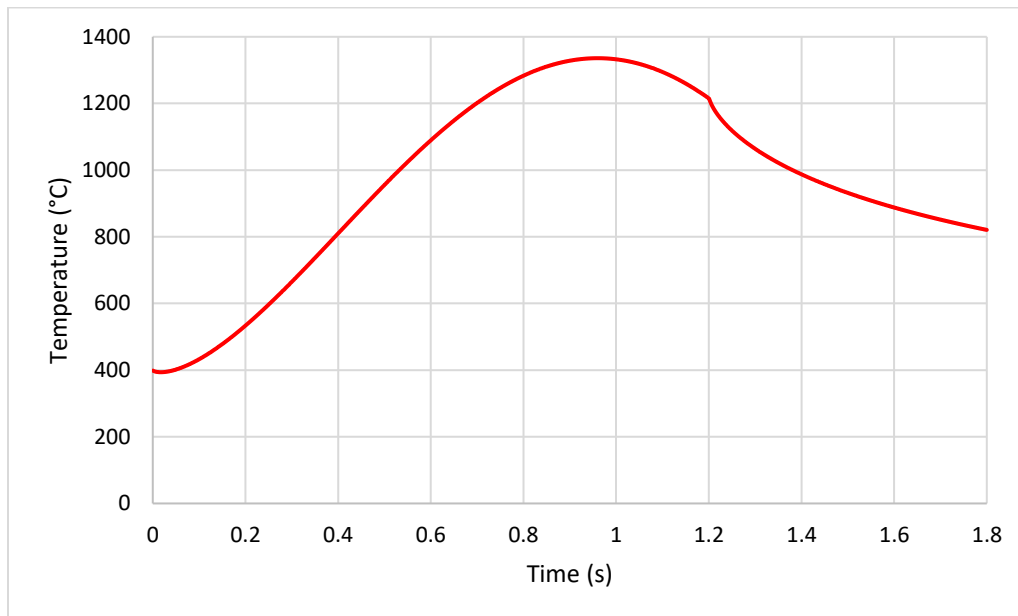
Figure 4-11. Maximum temperature of Ti-64 along the weld interface profile as a function of time from the numerical model.

28
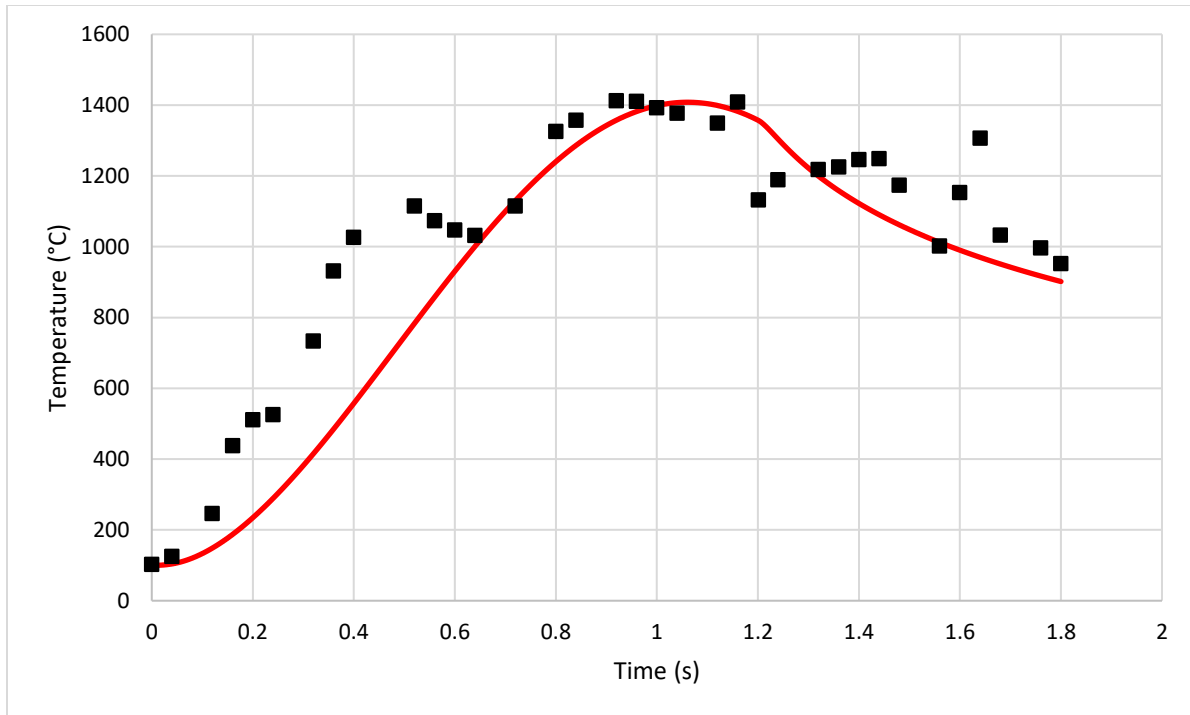
Figure 4-12. Comparison between experimental data the numerical model's thermal profile.

The results show a sinusoidal growth in temperature followed by a rapid decrease in temperature which coincides with the point where the frictional heat flux ceases. This is the expected outcome and matches the experimental results quite well with the numerical simulation only deviating in the beginning with a shallower growth, but afterwards it falls well within what was experimentally captured.

4.4 FINITE ELEMENT ANALYSIS

4.4.1 Materials

The material models for Ti-64 and CCM used material properties outlined in Chapter 3 under section 8.3 and 8.4, respectively.

4.4.2 Structure

Both the thermal and structural portions of the thermomechanical simulation were modeled in ANSYS. A 2D model was chosen for both portions of the simulation as 2D models can model the experimental trends without assuming material expulsion perpendicular to the oscillation direction [55]. Doing this saves a tremendous amount of computation time [84], without severely limiting the accuracy of the simulation model. The geometry of the 2D models were made to match the 2D cross-sectional view of the workpieces with an overall height being equal to the workpieces' nominal diameters and their overall length being determined by the distance at which the thermal values are unaffected by the heat flux generated by the LFW process. This distance was determined by analyzing the thermal history of the LFW process that was recorded by the FLIR IR imaging camera. As previously mentioned since CCM has virtually no literature analyzing its temperature-dependent material properties at elevated temperatures, thus the CCM side was considered to have constant thermal and mechanical properties. In stark contrast, Ti-64's material properties vary heavily with temperature and this variance is well documented. As such temperature-dependent material property values were created by picking off data points from property-temperature plots from literature, then inputting them into ANSYS. This was done to ensure that all temperature-dependent properties were represented within the range of 22°C to 1600°C, with the ambient temperature for both models being set to 22°C. The model geometry for the transient thermal and transient structural simulations can be seen in Figures Figure 4-13 and Figure 4-14, respectively.
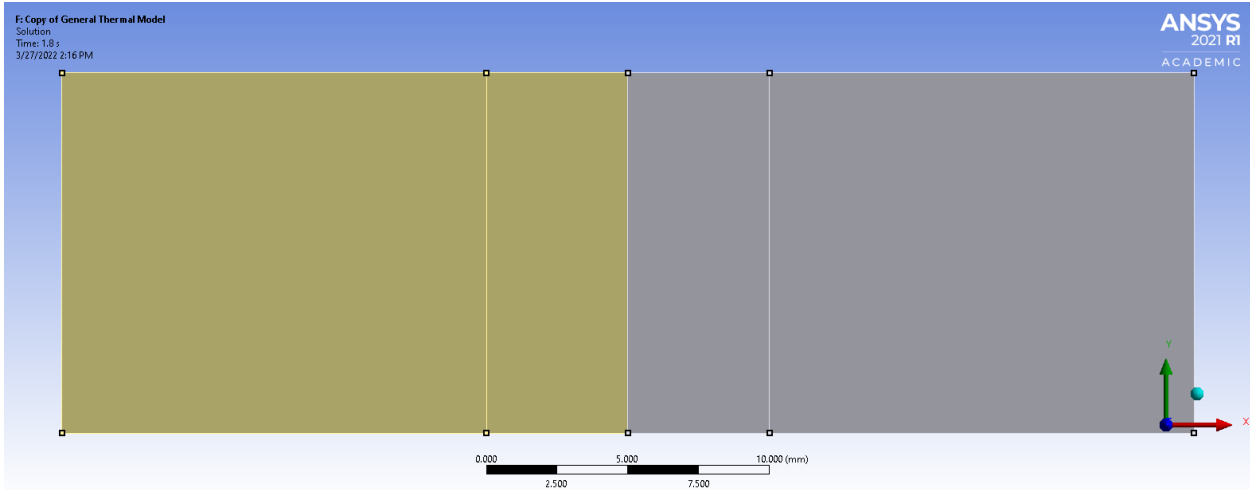
Figure 4-13. Transient thermal simulation model geometry.
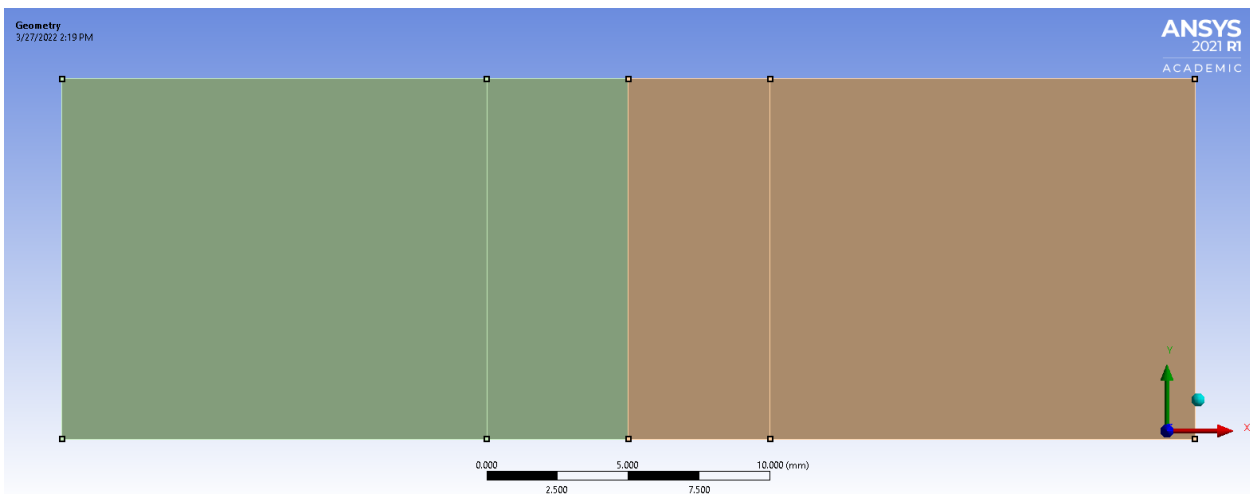
Figure 4-14. Transient structural simulation model geometry.

The mesh for the transient thermal simulation was created by modifying the program recommended settings. The element size was set to 0.2 mm, edges were set to be straight, and all other settings were left to their default values. This resulted in a total of number nodes and number elements. Figure 4-15 shows the resulting mesh for the transient thermal model, and Figure 4-16 shows a zoomed-in view of the elements along the weld interface.

Figure 4-15. Mesh distribution for the transient thermal FEA model.

Figure 4-16. Zoomed in view of mesh elements along the weld interface of the transient

thermal FEA model.

The mesh for the transient structural simulation was created by modifying the program

recommended settings. The elements were triangular with the elements in the HAZ having

element size of 0.2 mm. The elements in the bulk material had an element size of 0.635 mm. All

elements had their edges set to be straight. This was done to reduce the computation time, and

better allow for large deformations without reducing element size which would increase

computation times. As deformation was only being considered on the Ti-64 side, the CCM was

32

set to have rigid behavior. Because of this, the number of elements for the transient structural model was reduced by 50%. This resulted in a total of number nodes and number elements. Figure 4-17 shows the resulting mesh for the transient structural model. Figure 4-18 shows a zoomed-in view of the elements along the weld interface.
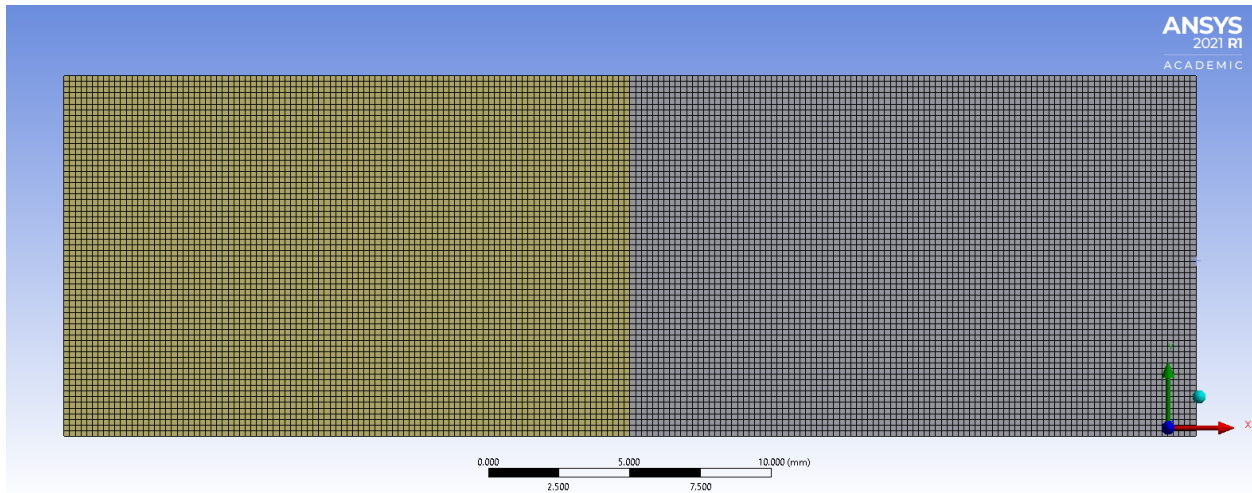

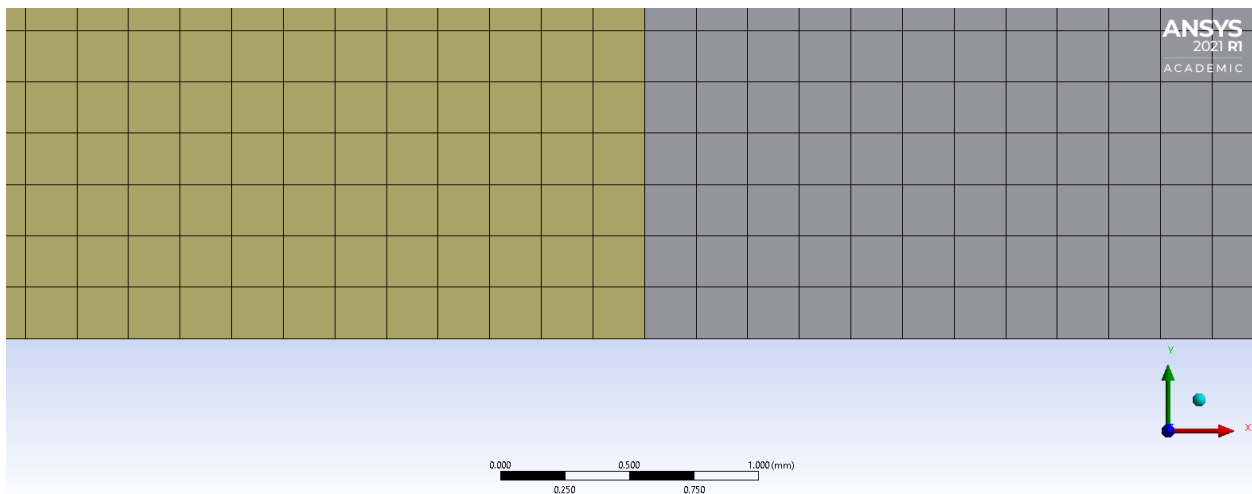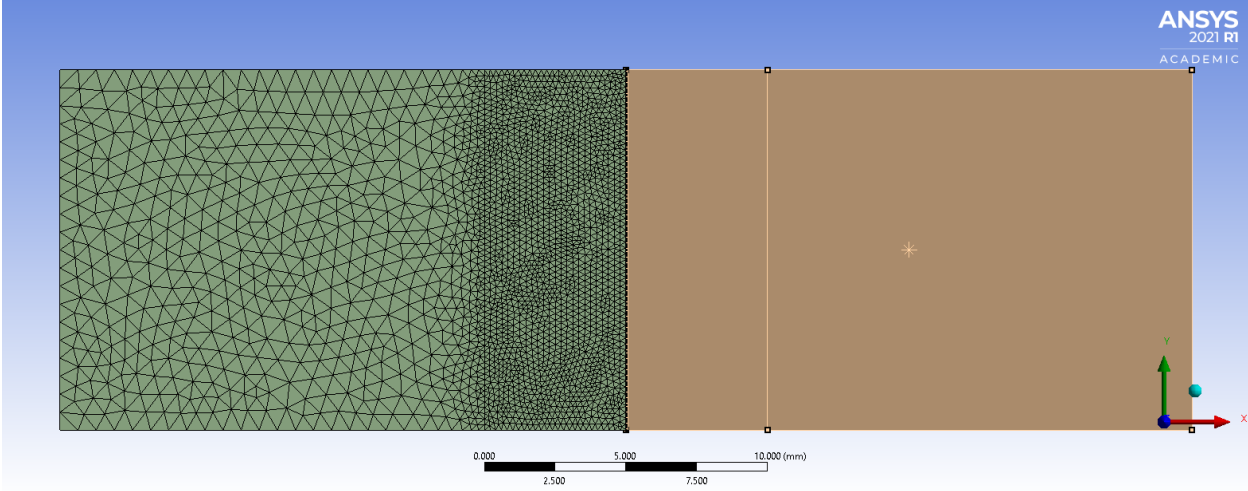*Figure 4-17. Mesh distribution for the transient structural FEA model.*
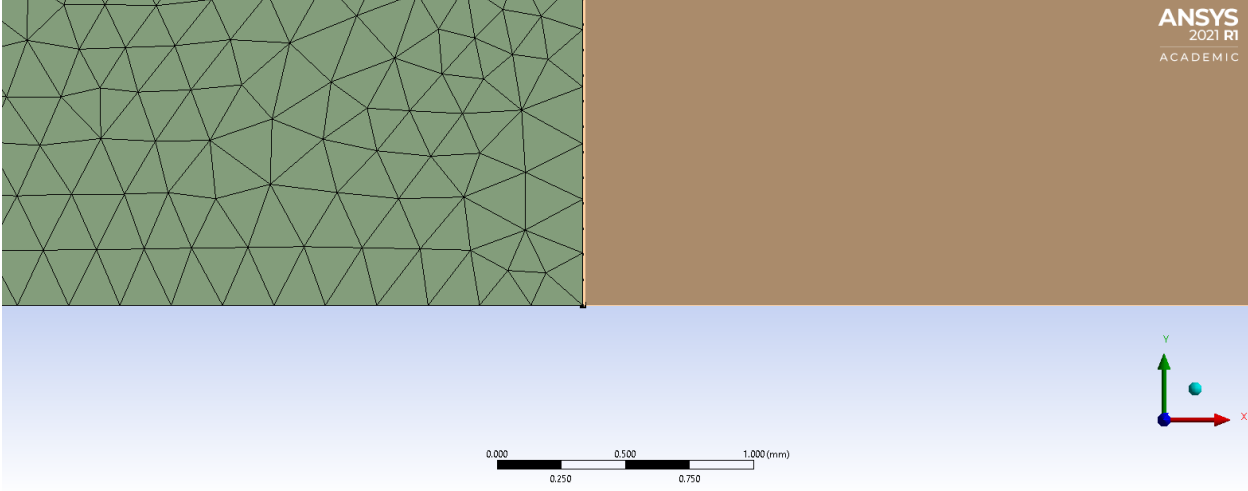
Figure 4-18. Zoomed in view of mesh elements along the weld interface of the transient structural FEA model.

4.4.3 Simulation Model – Transient Thermal Analysis

The transient structural simulation was modeled in ANSYS using the same model from the transient thermal model, but only considering deformation in the Ti-64 specimen. Its overall size was 12.7 mm by 20 mm. The constraints and applied for the transient thermal model can be seen below in Figure 4-19.
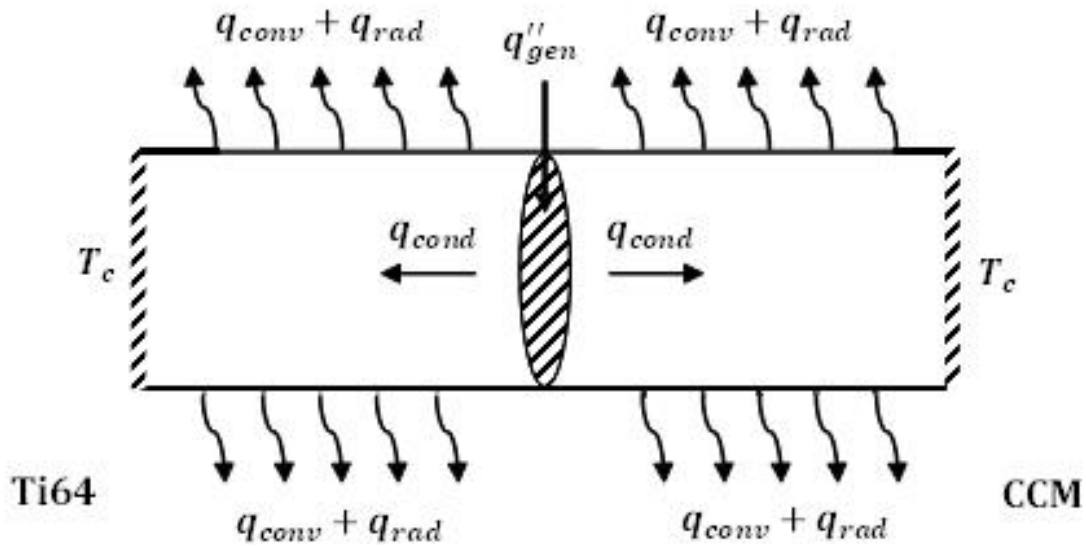
Figure 4-19. Transient Thermal Constraints.

4.4.4 Simulation Model — Transient Structural Analysis

The transient structural simulation was modeled in ANSYS using the same model from the transient thermal model, but only considering deformation in the Ti-64 specimen. As both models shared the same geometry, only minor adjustments were needed to structurally constrain the model and apply the appropriate thermal conditions and loads from the transient thermal model. The constraints and applied for the transient structural model can be seen below in Figure 4-20.
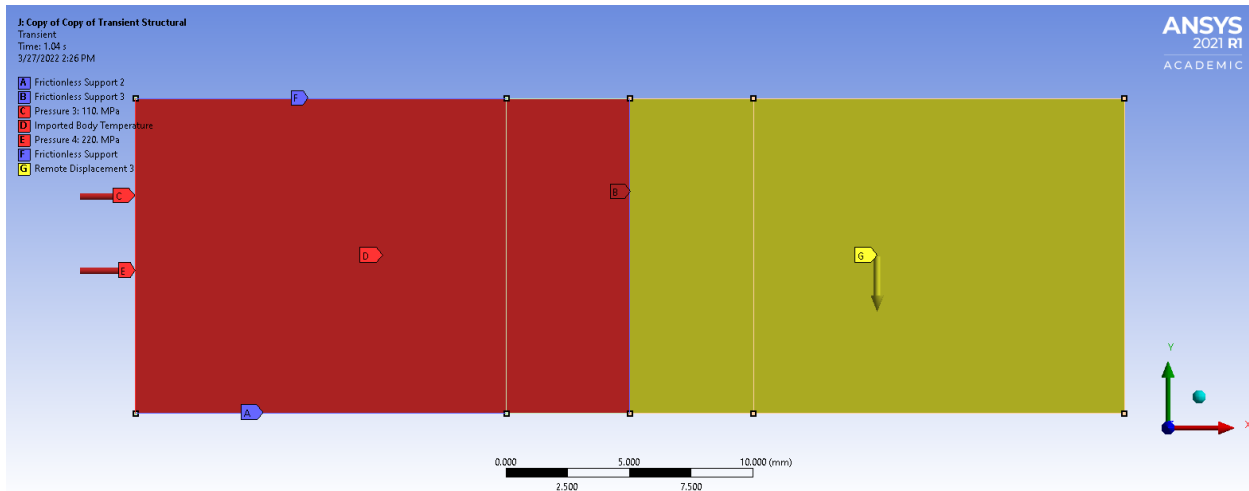
Figure 4-20. Transient Structural Constraints.

In addition to the structural constraints and loads previously mentioned, the thermal values of the Ti-64 portion of the transient thermal model were applied to the transient structural model at each time step to capture thermal strain in the structural analysis. As this was not an exploratory study; the applied force, ramp-up time, decay time, and forging time were not considered in this analysis. The effect of oscillation frequency, amplitude, burn-off, and forging pressure were parameters of interest for this model.

4.5   RESULTS AND DISCUSSION – THERMAL ANALYSIS

The results from the thermal simulation are shown in Figure 4-21 through Figure 4-26. With Figure 4-21 showing temperature field across both workpieces at the end of the welding process, and Figure 4-22 showing the temperature field of the workpieces at 1.1857 s into the welding process. Figure 4-23 plots the development of the maximum temperature along the weld interface over time. Figure 4-24 shows a plot comparing the development of the maximum temperature over time from the thermal simulation to the experimental thermal data. Showing that simulation's thermal development follows the same general trend as the experimental data

35

and is largely within 5% error of said data. Figure 4-25 shows the maximum thermal profile

across the workpieces from the simulation, which occurred at 0.9 s. In Figure 4-26 it is shown

that the simulated thermal profile is a good fit to the experimental thermal data found in Figure

4-4 typically falling within 5% error. Both Figure 4-24 and Figure 4-26 illustrate the accuracy of

the simulation with error of less than 5% in comparison the experimental results, and the ability

of the model to predict the thermal values of the part both longitudinally and transversely

throughout the welding process.
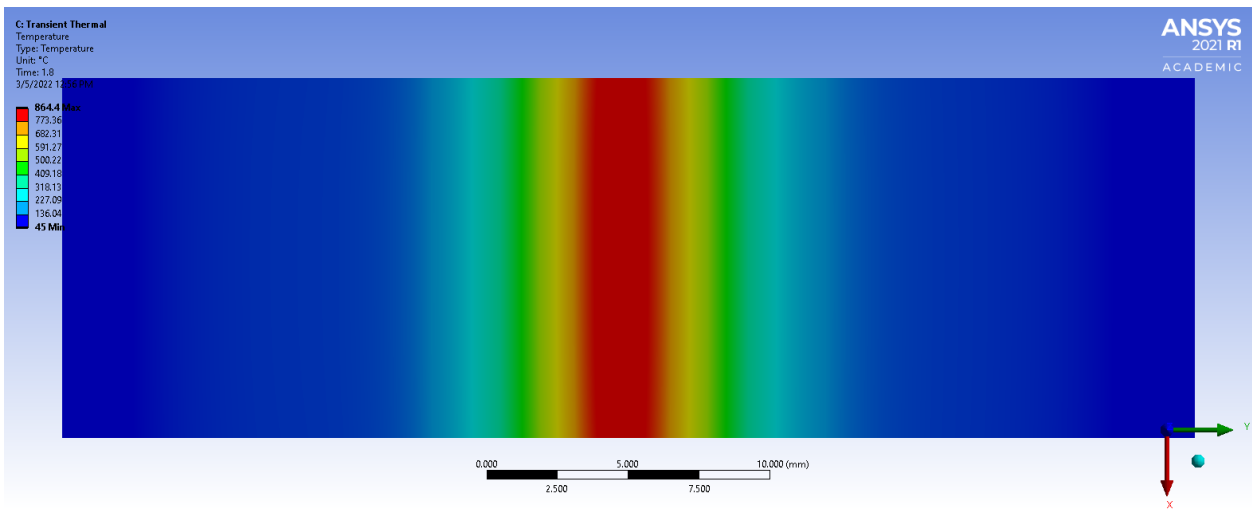
Figure 4-21. Temperature profile across the workpiece at 1.8 s.
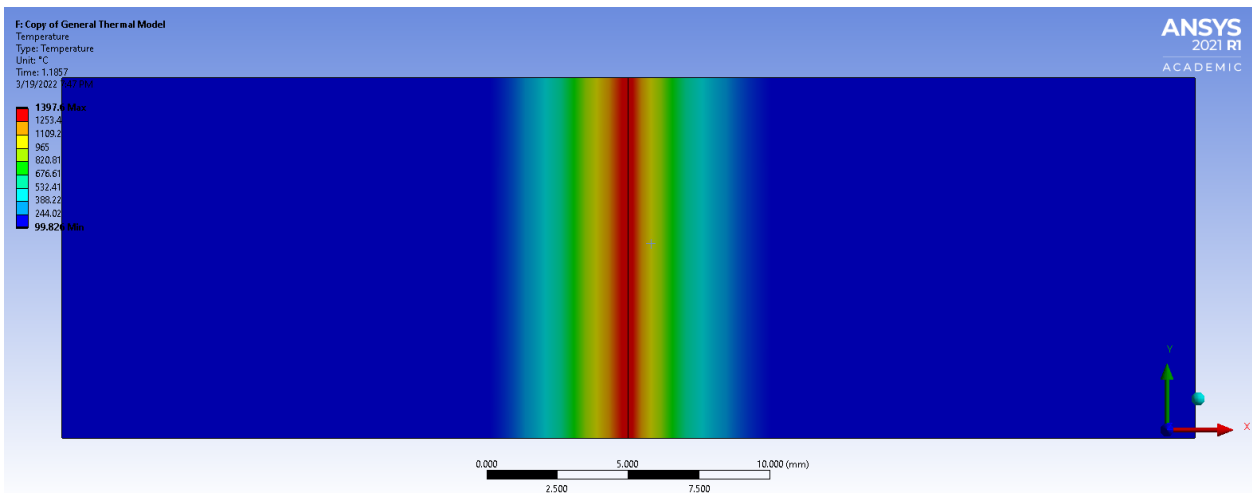
Figure 4-22. Temperature profile across the workpiece at 1.1857 s.
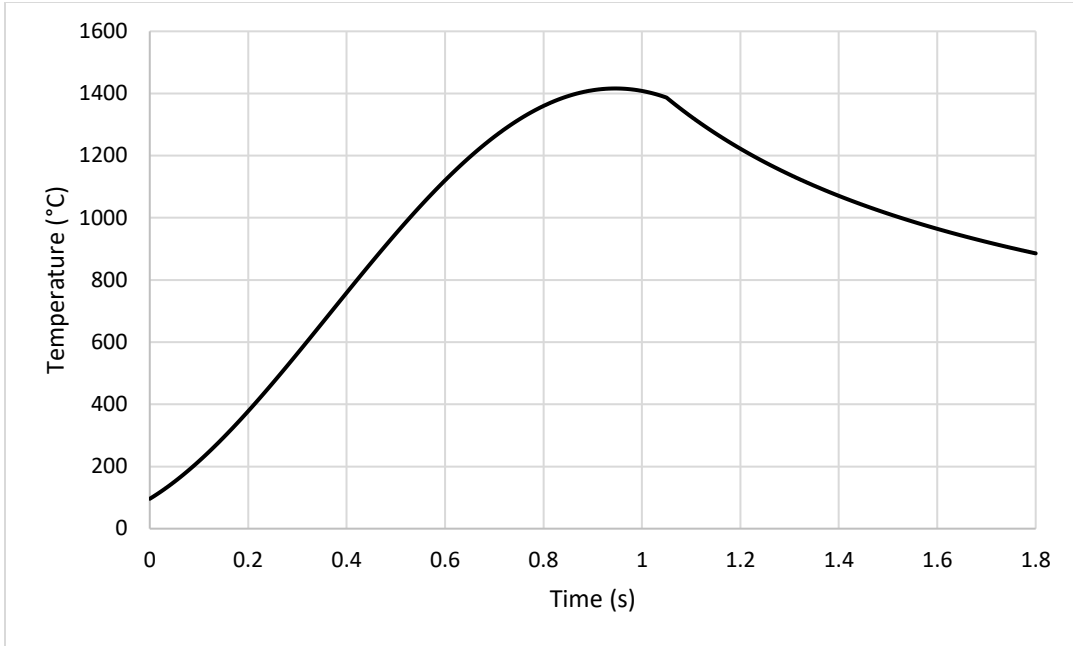
Figure 4-23. Maximum temperature of Ti-64 along the weld interface profile as a

function of time from the transient thermal model.
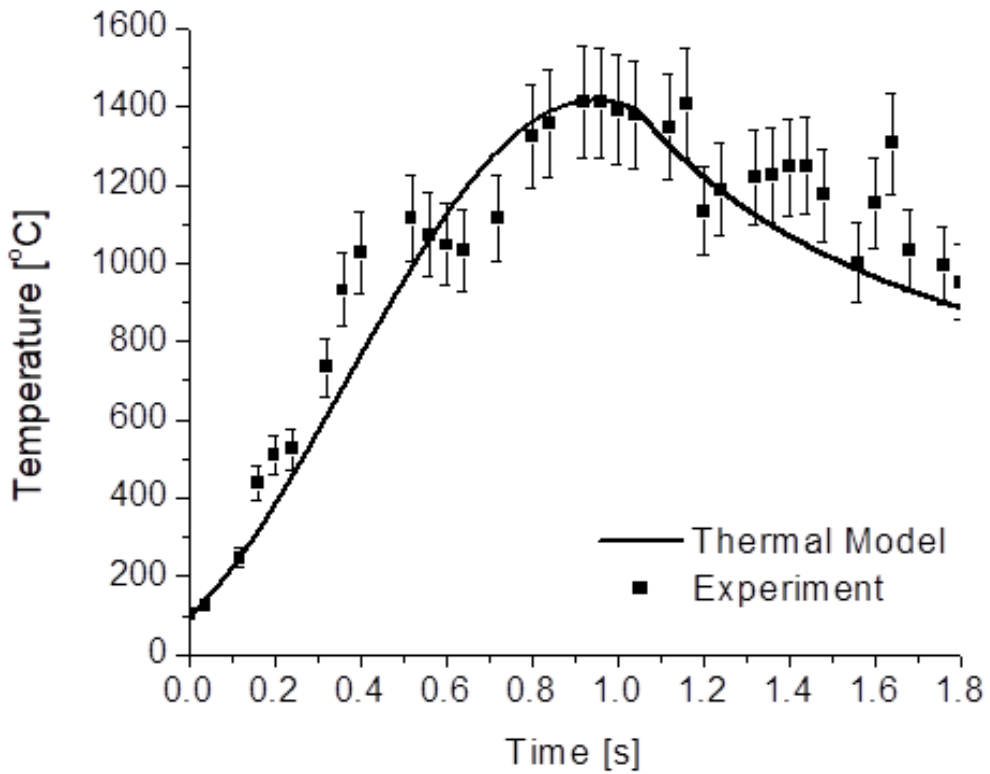
Figure 4-24. Comparison of the thermal model to experimental results. [79]
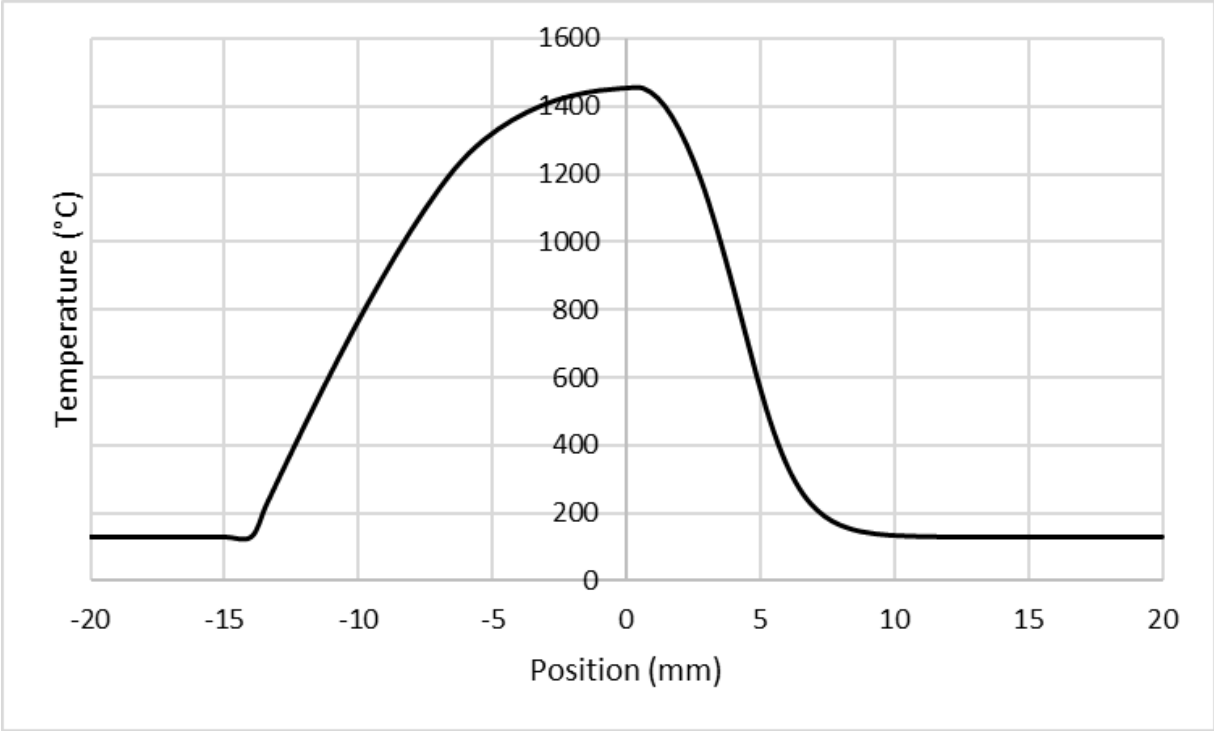
Figure 4-25. Temperature field across the workpiece at the end of the simulation.
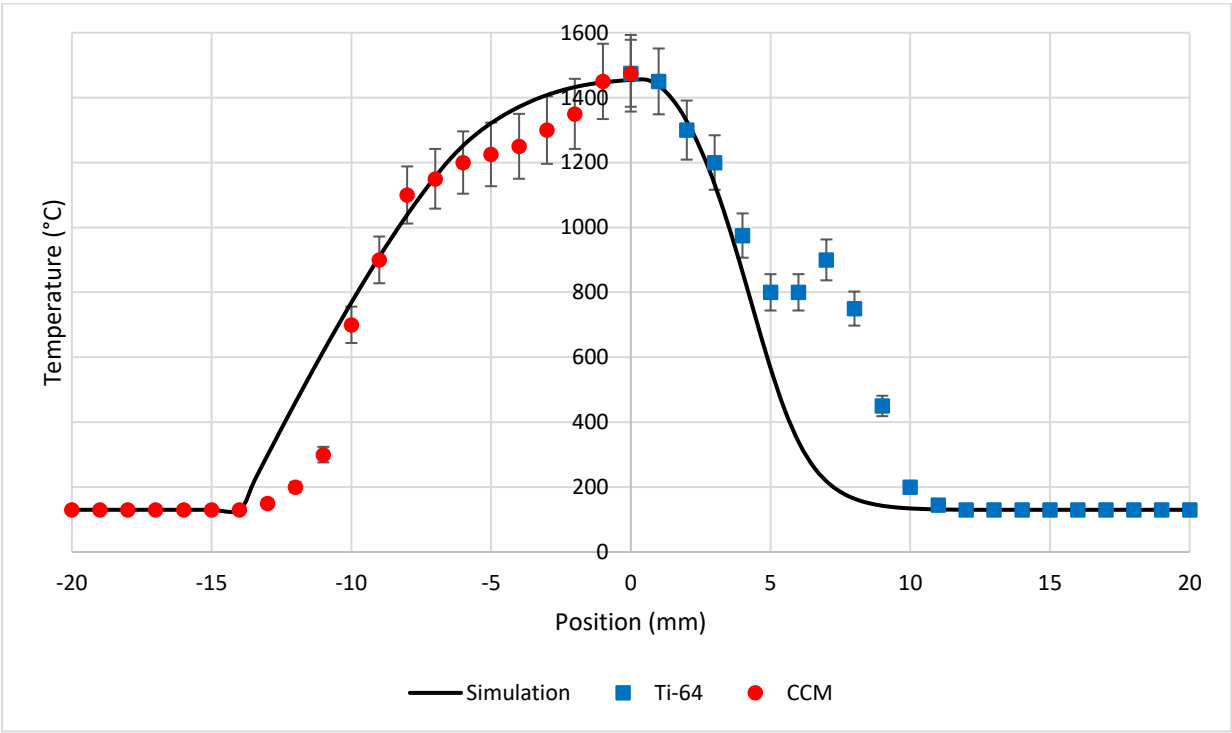
Figure 4-26. Comparison of simulated thermal profile across the workpiece to thermal

data at 1.2 s into the weld process.

4.6 RESULTS AND DISCUSSION – STRUCTURAL ANALYSIS

The deformation which is caused by the thermal stress and thermal expansion can be seen below in Figure 4-27. Figure 4-28 shows the total Ti-64 deflections from the thermomechanical simulation model. The deformations match well with experimental results. Figure 4-29 compares the deformation profile of the simulation to the experimental results. Successful bonding of the welded specimens was not achieved, with the notable exception of test 7. This implies that for a set oscillation frequency of 50 Hz, amplitude of 4 mm, and a forging pressure of 270 MPa a burn-off distance of 7.62 mm is required for successful bonding. Both experimental and simulation results show excessive deformation is primarily generated by the Ti-64 while the CCM generated virtually no deformation, this wrapping phenomenon is most likely the cause of the weld failure.
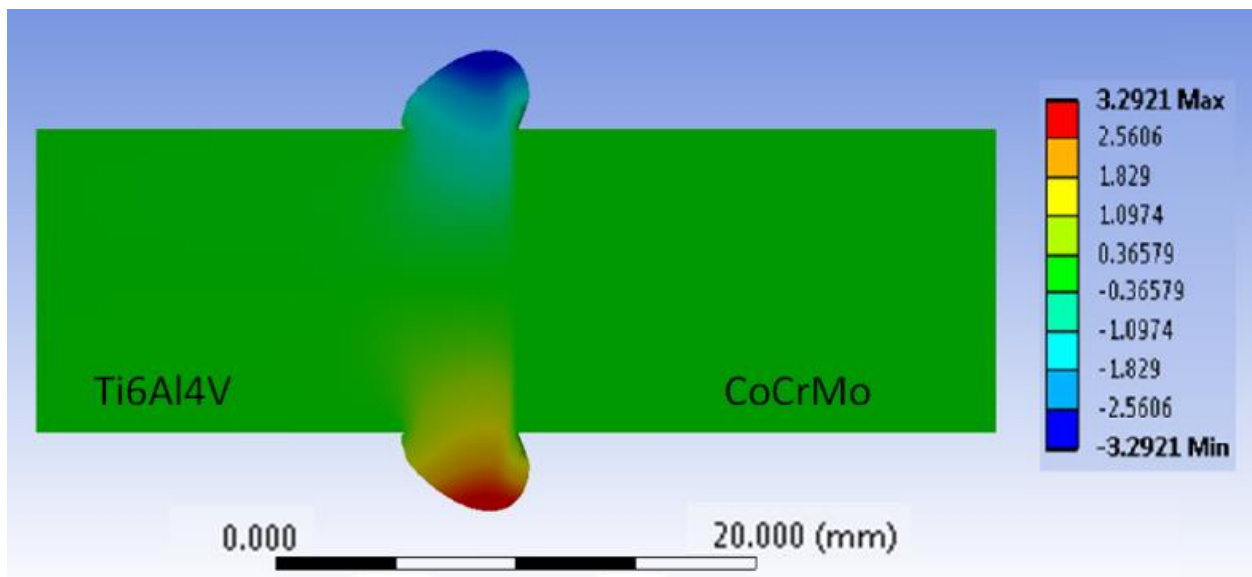
Figure 4-27. Deflections generated from the thermomechanical simulation model. [2, 79]
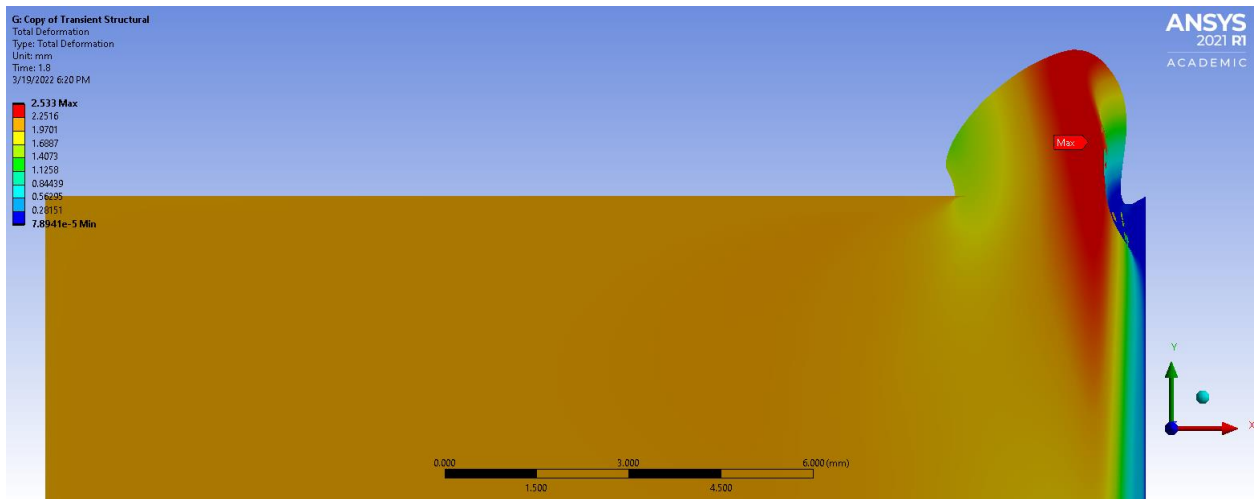
Figure 4-28. Ti-64 deflections generated from the thermomechanical simulation model.
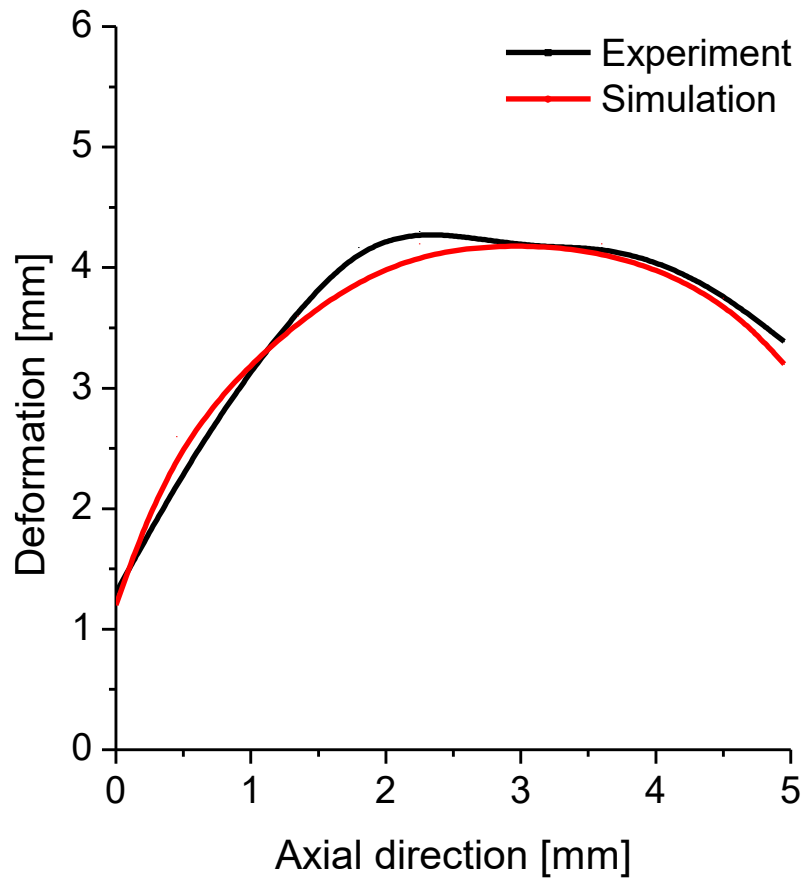
Figure 4-29. Comparison of simulation and experimental deflection results. [2]

4.7 Conclusions

This study produced a FEA model to predict the temperature profile of welded workpieces along and across the weld interface throughout the welding process. The analysis also shows the structural deformation generated from the LFW process which fall in line with the experimental results. The thermal model accounted for conduction, convection, and radiation. Results from the thermal simulation measure within 5% error tolerance to the experimental data. The welding process was monitored with an IR camera to record the development of the thermal profile of the weld-affected area. The experimental results showed that the Ti-64 workpiece tended to wrap around the CCM workpiece rather than bond to it. This was primarily caused by Ti-64 undergoing its beta transus phase change, which occurs in the temperature range of 900°C to 1000°C. The phase change weakened it, while CCM doesn't undergo a similar phase change thus it simply sheared the Ti-64 causing the Ti-64 to wrap around it. It should also be noted that increasing the forging pressure, forging time, and blanking the frequency of the oscillation improved the resulting weld. This suggests that (1) parameter optimization is crucial to achieving successful bonding via LFW and (2) that materials chosen for dissimilar bonding should have similar melting points and have similar material properties such as tensile strengths at peak temperatures during the welding process to achieve improved bonding. In conclusion, the joining of Ti-64 to dissimilar high-strength metals via LFW is not recommended as Ti-64 undergoes a beta transus phase change which greatly reduces its tensile, shear, and compressive strengths. Although, bonding of Ti-64 to low strength metals or high strength plastics is possible as the reduced material strength of Ti-64 would allow for bonding so long as the other material as a similar melting point to Ti-64.

5 LW RESEARCH

5.1 INTRODUCTION

This study focuses on the effect of laser power on the weldability of Ti-64 to Nitinol butt welds via LW. The experimental design of this study was constructed such that the experiment would be broken into two groups with one group having twice the laser power as the other with all other parameters being identical. This was done to determine the effect of laser power on the weldability of the dissimilar metals. The exact parameters used are detailed in the experiment section. Thermal imaging was incorporated to collect thermal data to help build an accurate thermomechanical simulation model. Thermal monitoring is a commonly used technique in the literature, although the typical method is done via implanting thermocouples in the parent materials near the weld interface or by placing the thermocouples so close to the workpieces that the temperature gradient from heat loss from is negligible. This work instead monitored the thermal history of the welding process via a thermal imaging camera.

This work demonstrates how essential detailed knowledge of material properties at elevated temperatures are as those properties are the primary factor in determining what types of approximations, and assumptions are necessary. It is also the one of the primary factors in deciding which analysis method to use for simulation.

5.2 LW EXPERIMENT

Both materials came as flat rectangular stock. The flat stock was machined to flat plates measuring 2 mm by 60 mm by 120 mm. As the cost of the materials was prohibitively expensive only 6 specimens were manufactured. A figure detailing the process parameters used in the

42

experiment can be seen in Figure 5-1. A table listing the process parameters used during the

welding process can be seen below in Table 5-1.
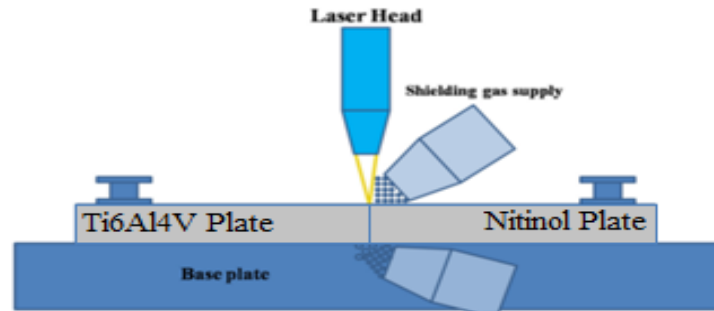
Figure 5-1. LW Schematic detailing process parameters. [85]

Table 5-1. Process parameters used for the LW experiment. [85]

Trials	Specimens	Laser Power (W)	Weld Speed (mm/s)	Heat Input (J/cm)	Weld Time (s)
	1		5	1500	12.07
1	2	750	20	375	3.02
	3		100	75	0.60
	4		5	3000	12.07
2	5	1500	20	750	3.02
	6		100	150	0.60

As with the LFW research, a FLIR E60 thermal imaging camera was utilized to capture

the temperature history throughout the welding process. Again, this was paired with a computer

running the FLIR Tools software package in order to record, save, and later analyze the

thermographic history. A thermal image taken during the welding process can be seen in Figure

5-2 where the thermal values are in Celsius. From Figure 5-2 the thermal profile along the weld

interface at the end of the LW process was extracted. The extracted thermal profile was a

function of pixels and can be seen in Figure 5-3. It was then converted into units of length,

specifically millimeters. This final thermal profile was used to validate the thermal portion of the

FEA model. The final thermal profile can be seen in Figure 5-4.
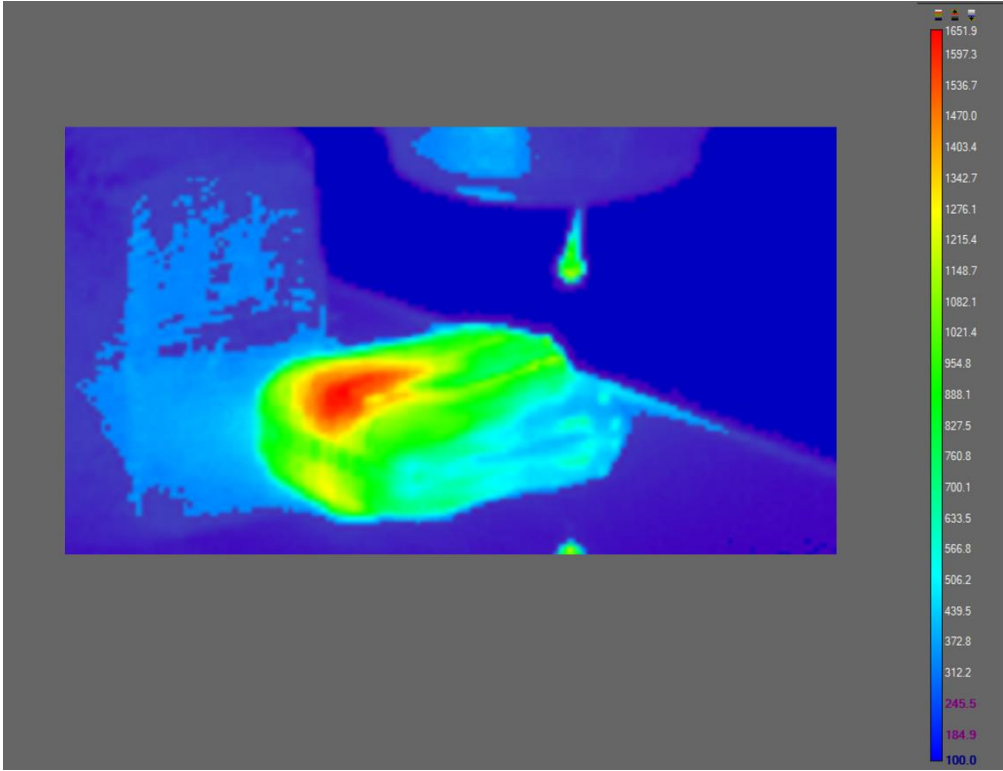
Figure 5-2. IR image taken at the end of the welding process.
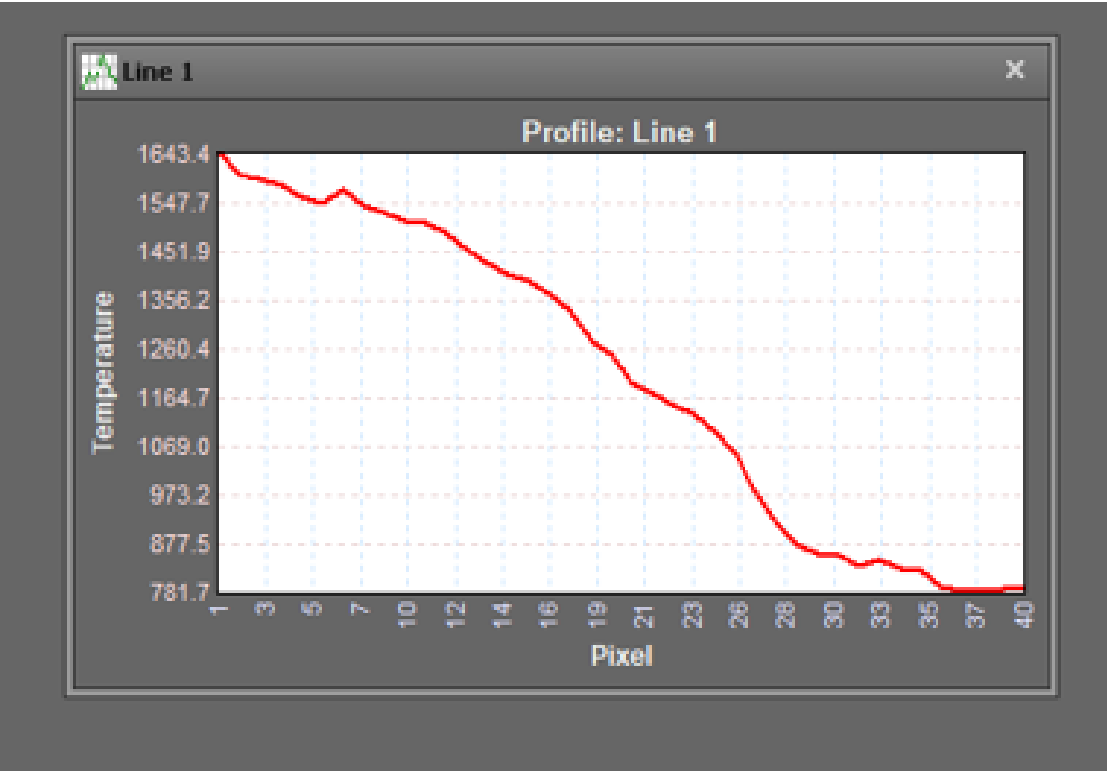
Figure 5-3. Thermal profile along the weld interface at the end of the welding process.
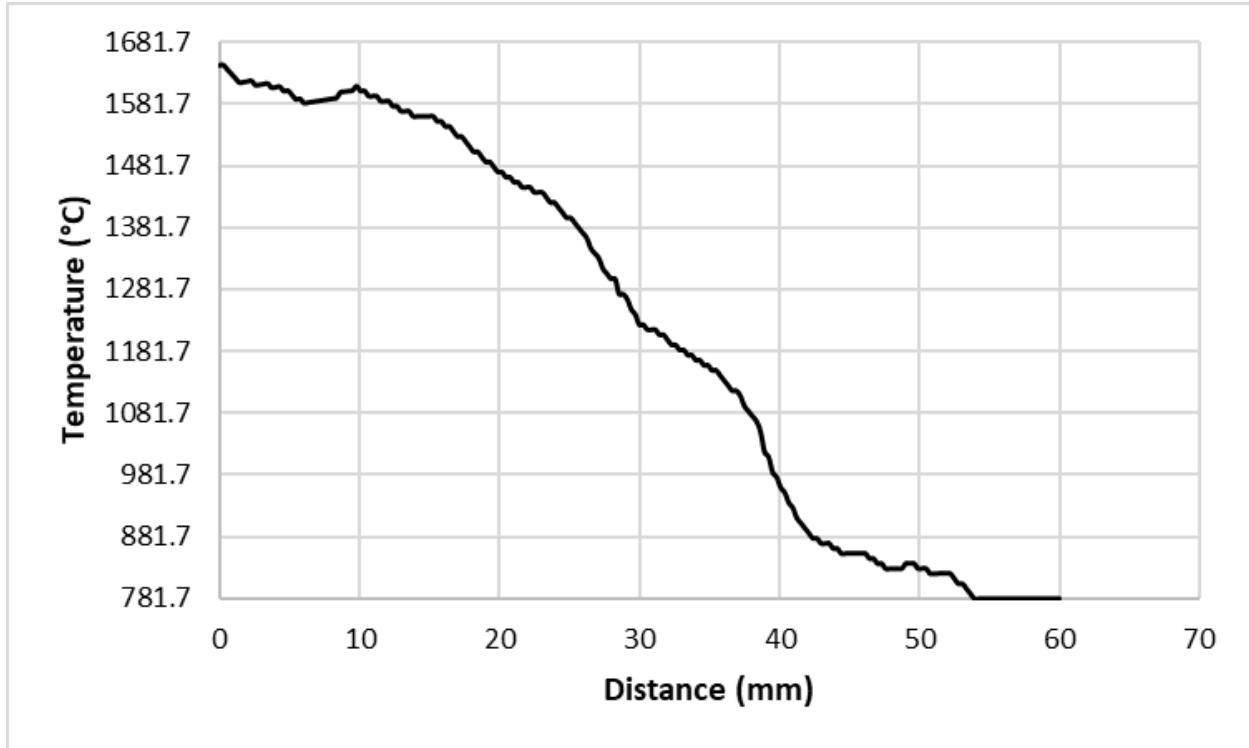
Figure 5-4. Extrapolated thermal profile along the weld interface.

5.2.1 Experimental Analysis

Tensile testing was not performed on the samples as visual inspection showed that bonding was unsuccessful primarily due to the presence of thermal cracking. Figures 5-5 and 5-6 display the LW results for trials 1 and 2, respectively. Measurements of the weld deformation across the weld interface were taken to serve as a reference for the FEA simulation model. From those measurements a deformation profile was created. The experimental deformation profile can be seen in Figure 5-7.
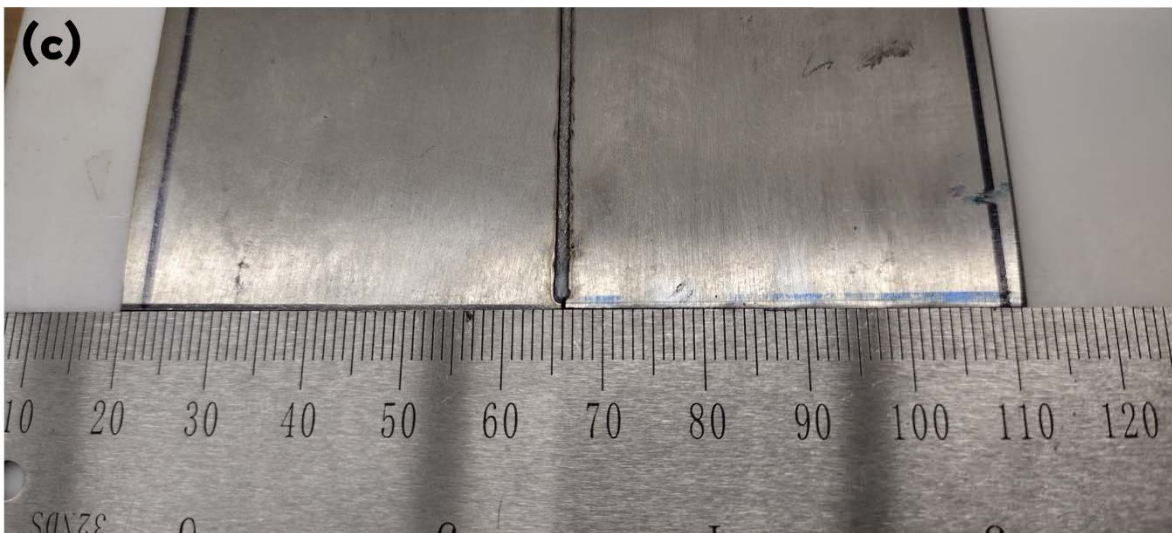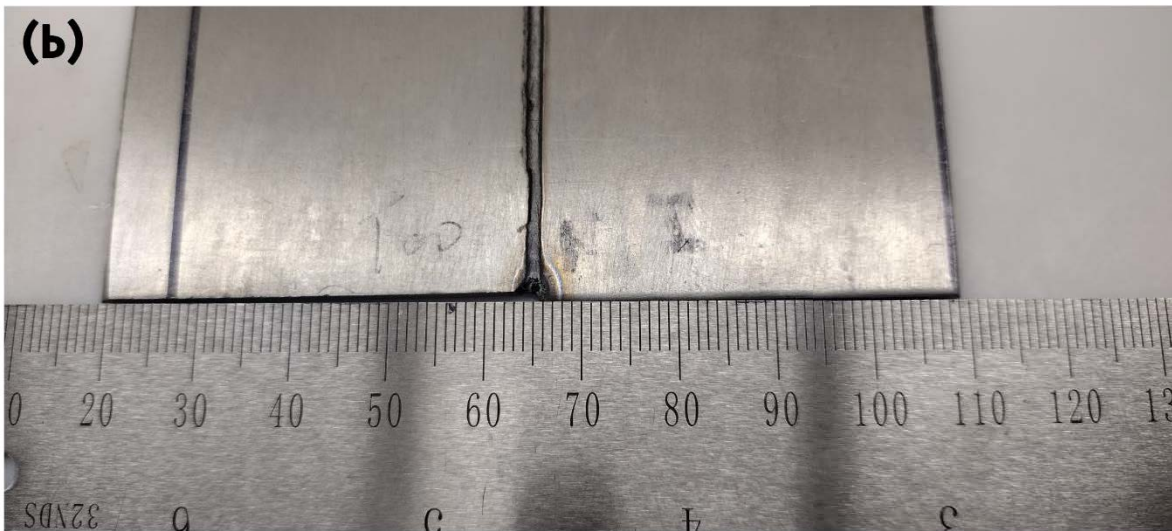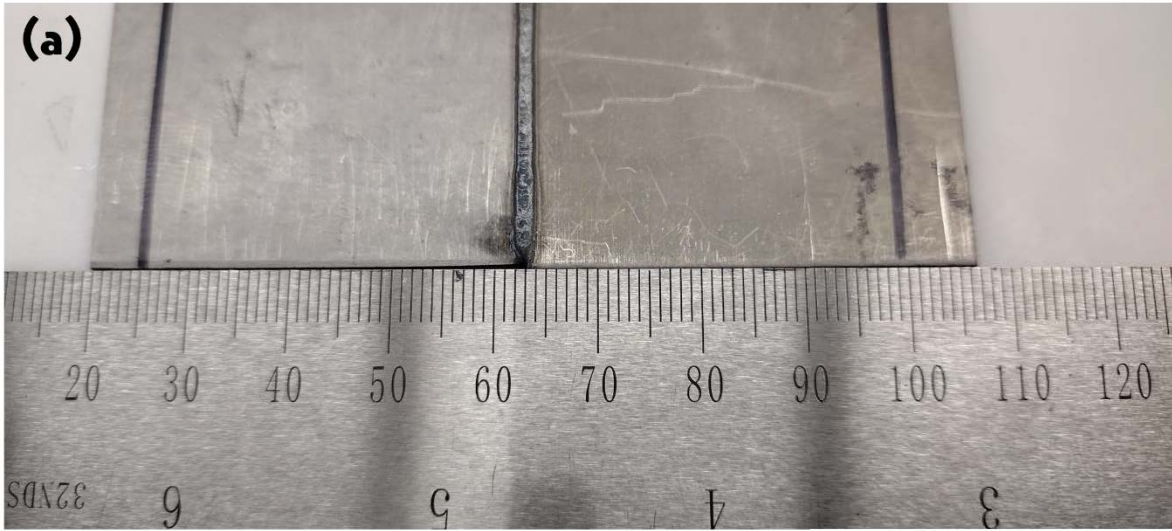
Figure 5-5. Trial 1 LW results for velocities (a) 5 mm/s, (b) 20 mm/s, and (c) 100 mm/s.
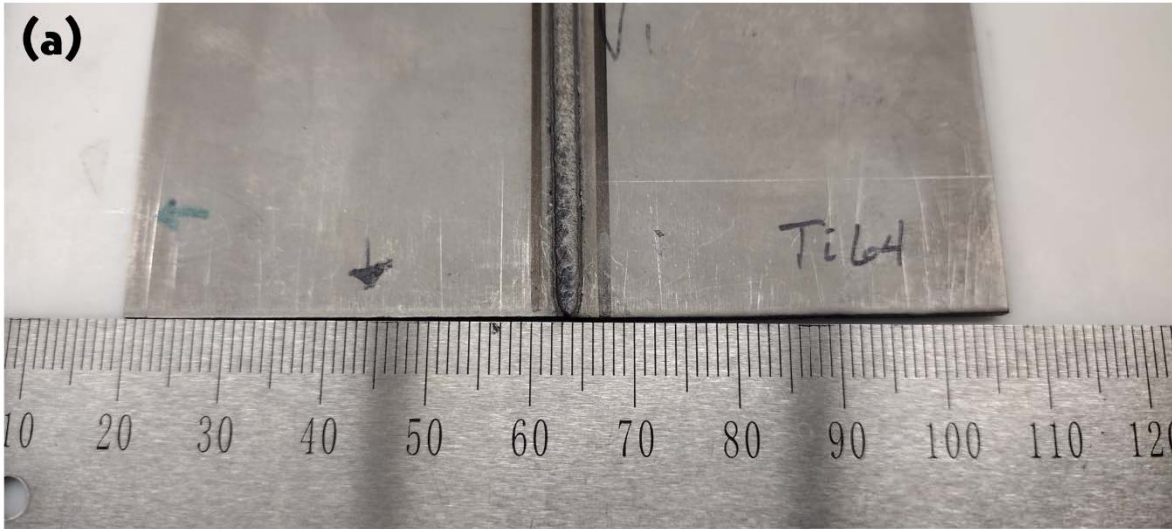
Figure 5-6. Trial 2 LW results for velocities (a) 5 mm/s, (b) 20 mm/s, and (c) 100 mm/s.
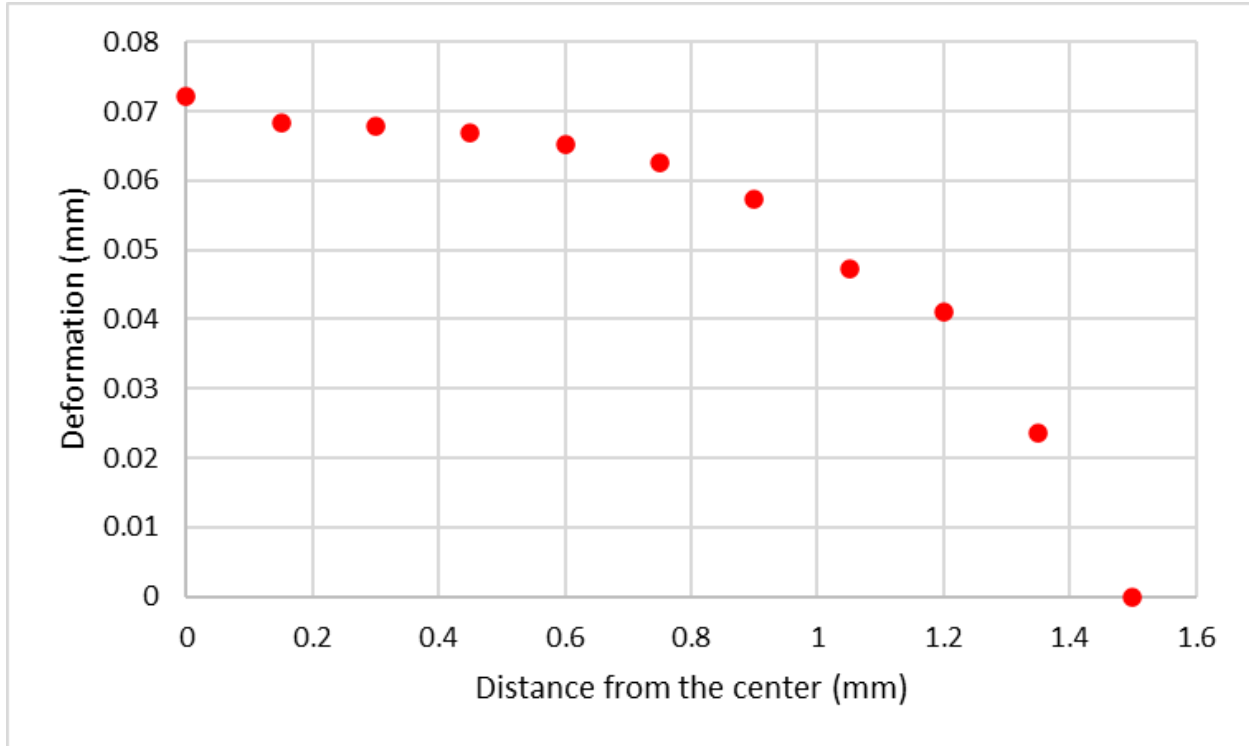
Figure 5-7. Experimental deformation data across the weld interface.

To determine if material flowed across along the weld interface SEM imaging was performed with EDS analysis utilizing the JEOL JIB-4500 MULTI BEAM SYSTEM. To achieve this samples were taken from both sides of the weld interface. These samples were prepared in accordance with standard metallic specimens for SEM analysis. A total of 6 SEM images were taken for each specimen with the standard electron voltage of 15kV. The SEM images for the Ti-64 and Nitinol specimens can be seen below in Figures 5-8 and 5-9, respectively. Note that the black regions in Figures 5-8 and 5-9 are surface cracks which are too deep for SEM imaging. As such, those regions are displayed as completely black.
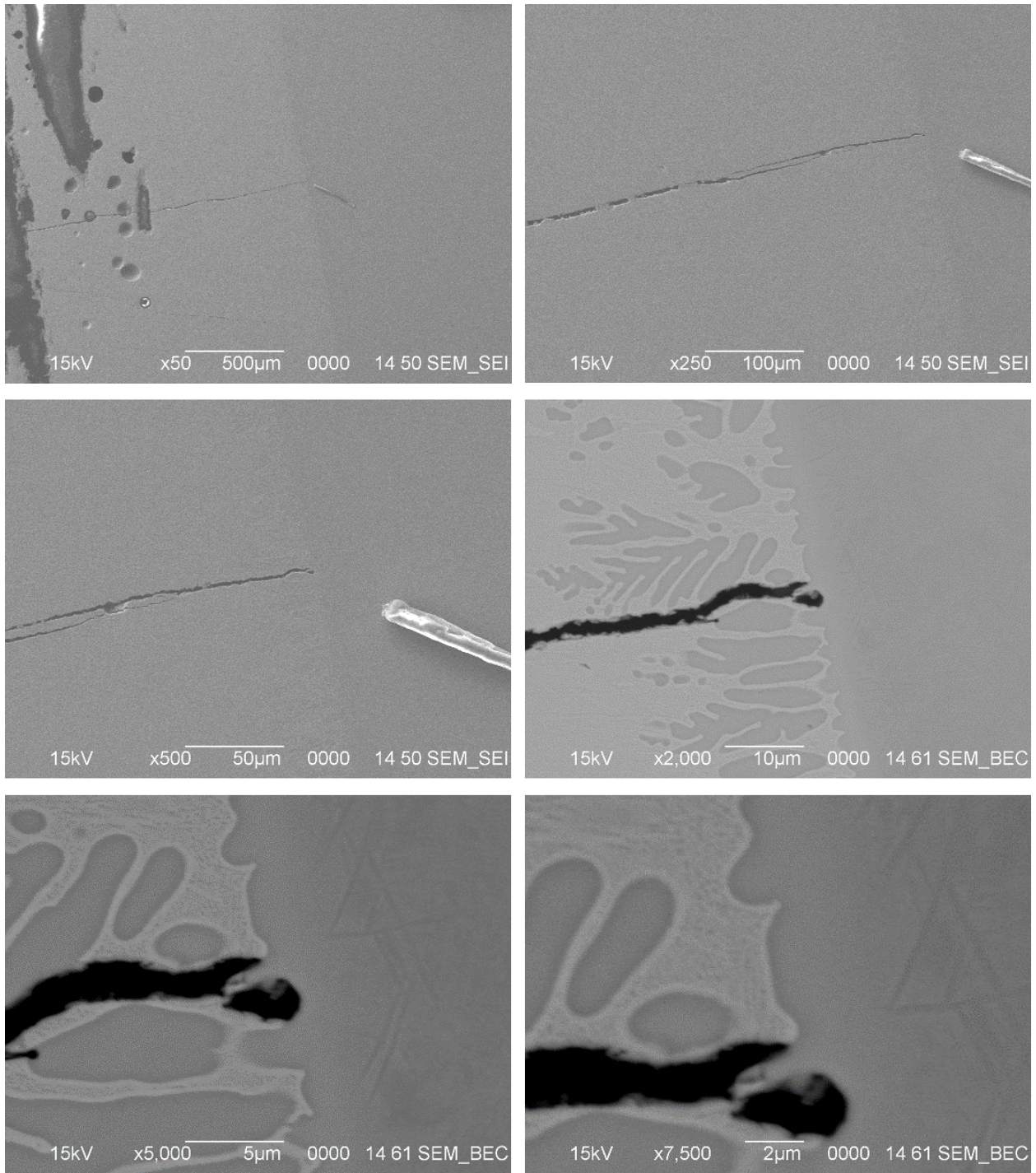
Figure 5-8. SEM imaging of Ti-64 specimen.
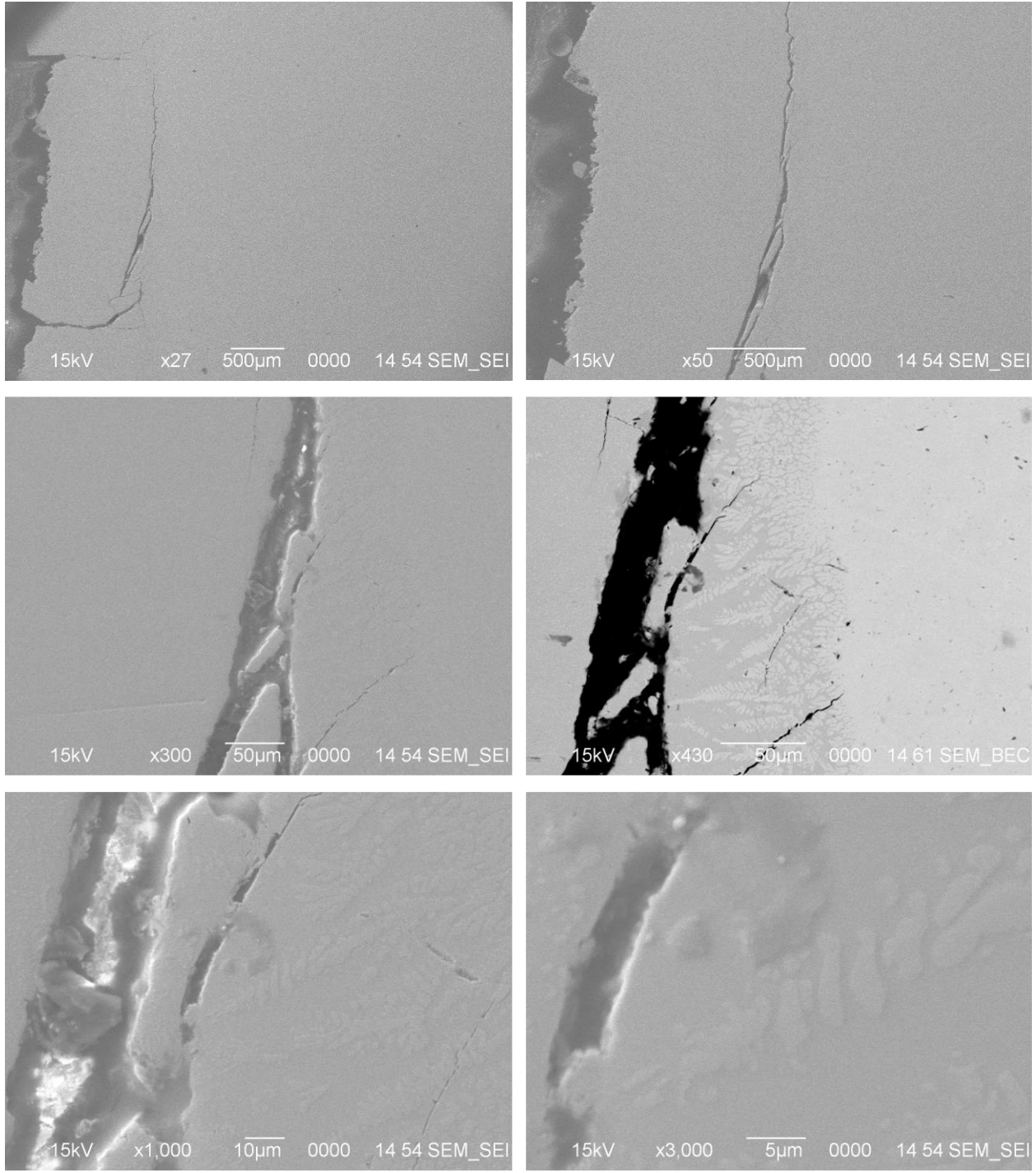
Figure 5-9. SEM imaging of Nitinol specimen.

Following the SEM imaging, EDS was performed at three different regions for each specimen to determine the material composition in different areas. Again, note that the pure black regions in Figures 5-10 through 5-15 are surface cracks. Figures 5-10 through 5-12 show the EDS results for the selected regions of the Ti-64 specimen, and figures 5-13 through 5-15 shows the EDS results for the regions of the Nitinol specimen. From Figures 5-10 through 5-12 cross-contamination of the two materials can be shown to have occurred due to the fact that there are large Ni k peaks in two of the three regions of the Ti-64 specimen. This is also confirmed when looking at figures 5-13 through 5-15 as there are clear Al k peaks in the Nitinol specimen. These results show that crossflow between the two materials during the laser welding process did occur.

Element	Wt%	At%
VL	00.00	00.00
AlK	11.66	18.98
TiK	88.34	81.02
Matrix	Correction	ZAF
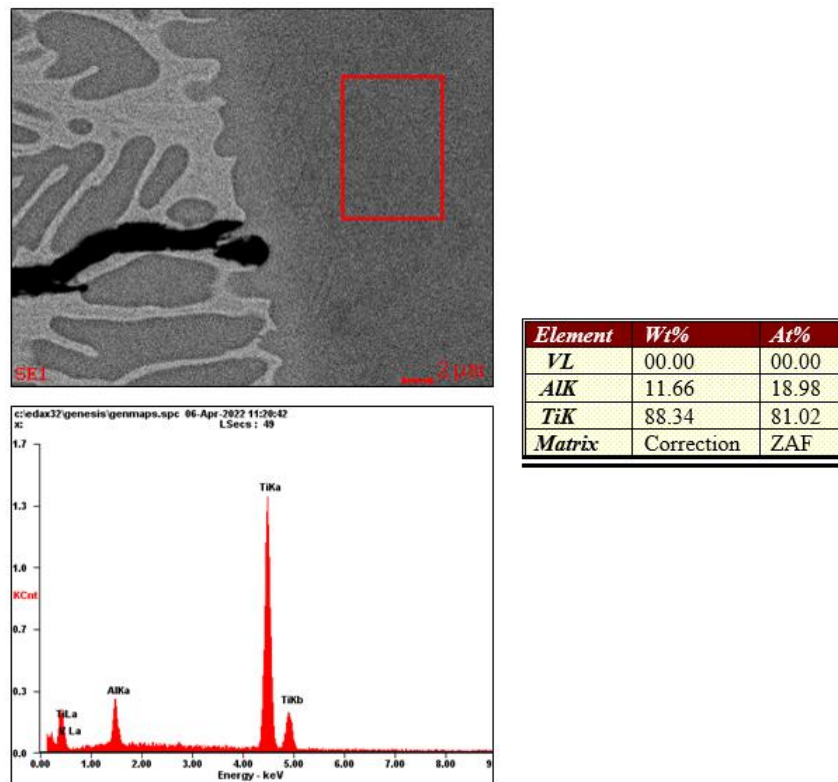
Figure 5-10. EDS analysis of region 1 for Ti-64 specimen.
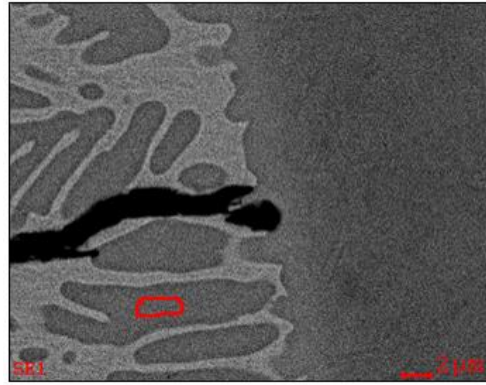
Element	Wt%	At%
AlK	10.25	17.21
TiK	77.74	73.52
NiK	12.01	09.27
Matrix	Correction	ZAF
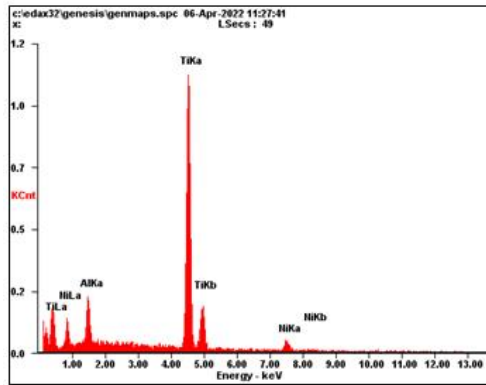
Figure 5-11. EDS analysis of region 2 for Ti-64 specimen.
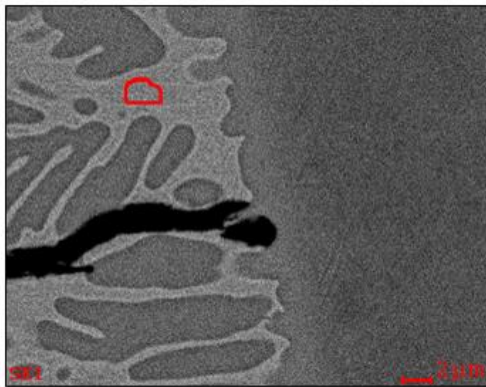
Element	Wt%	At%
AlK	06.53	11.64
TiK	64.28	64.48
NiK	29.19	23.89
Matrix	Correction	ZAF
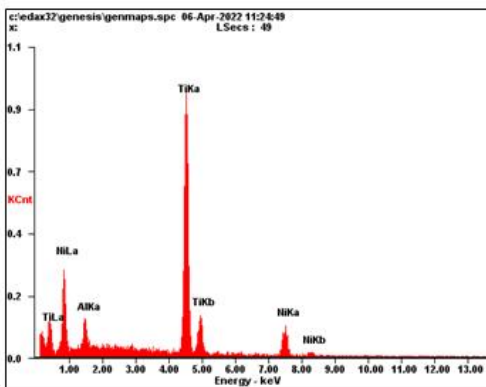
Figure 5-12. EDS analysis of region 3 for Ti-64 specimen.

52
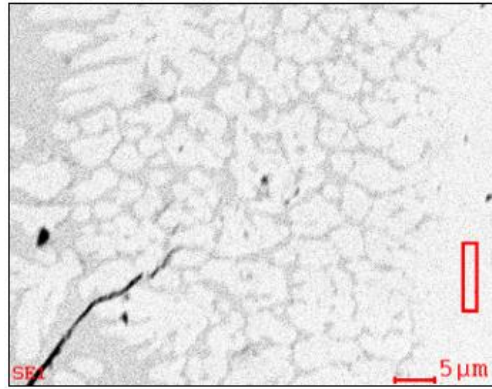
Element	Wt%	At%
TiK	44.55	49.62
NiK	55.45	50.38
Matrix	Correction	ZAF
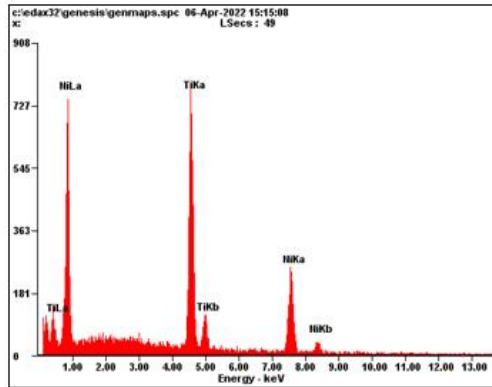
Figure 5-13. EDS analysis of region 1 for Nitinol specimen.
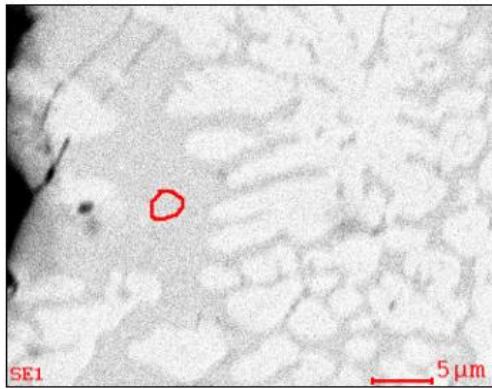
Element	Wt%	At%
AlK	03.83	07.10
TiK	57.53	60.01
NiK	38.64	32.89
Matrix	Correction	ZAF
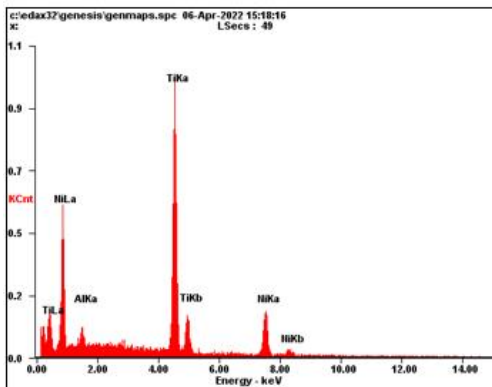
Figure 5-14. EDS analysis of region 2 for Nitinol specimen.

Element	Wt%	At%
AlK	01.47	02.85
TiK	45.09	49.39
NiK	53.44	47.76
Matrix	Correction	ZAF
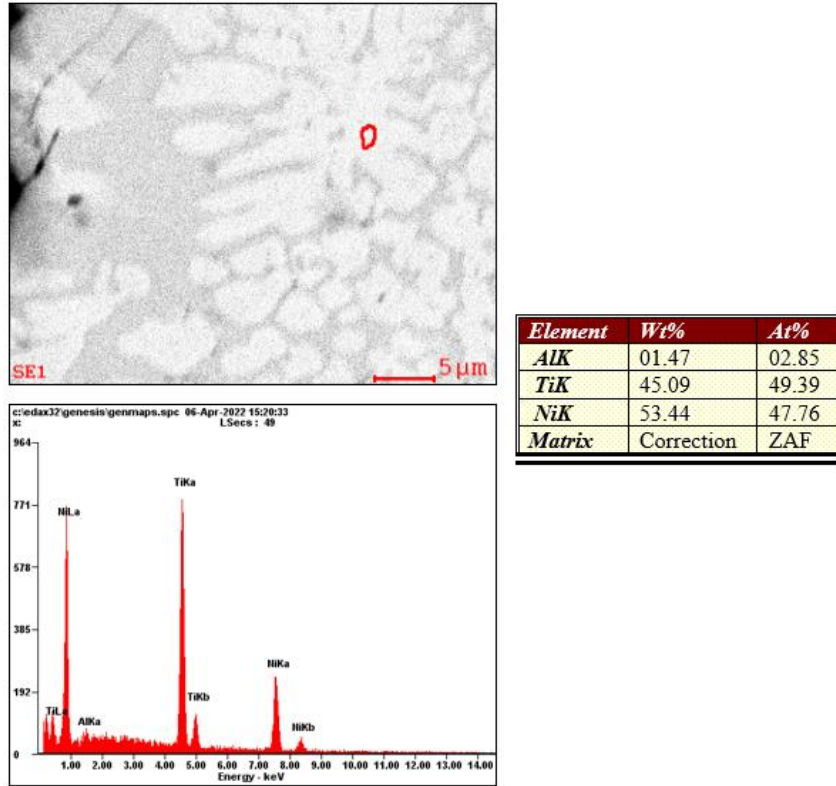
Figure 5-15. EDS analysis of region 3 for Nitinol specimen.

5.3 FINITE ELEMENT ANALYSIS

5.3.1 Materials

The material models for Ti-64 and Nitinol. The material properties of Ti-64 are outlined in Chapter 3 under section 3.8.3. Nitinol is a shape memory alloy often used in the medical industry as for stents for heart valves and blood vessels due to its shape memory properties and its biocompatibility. Nitinol's shape memory effect is temperature dependent with the activation temperature ranging from 20°C to 100°C. Figures 5-16 through 5-18 display Nitinol's thermal and mechanical properties as functions of temperature. Table 5-2 lists the constant material properties of Nitinol used for the simulation.
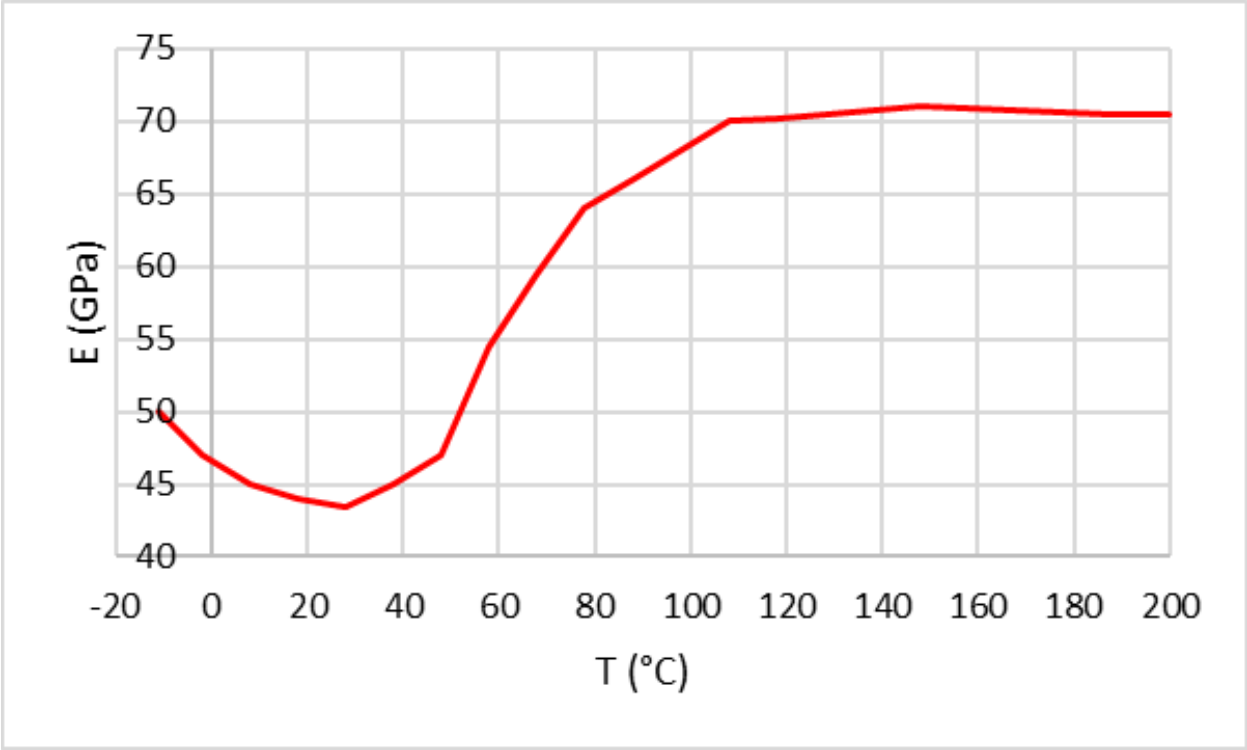
Figure 5-16. Young's Modulus as a function of temperature. [86]
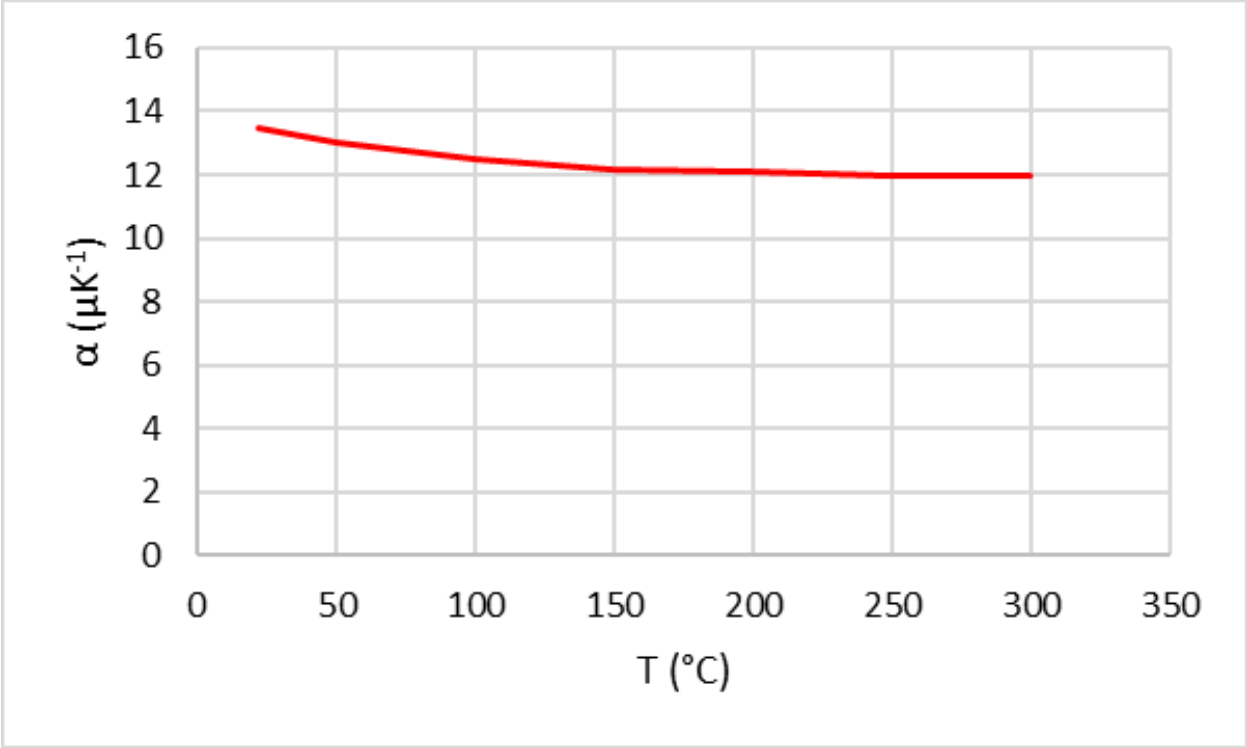
Figure 5-17. Coefficient of linear thermal expansion as a function of temperature. [87]
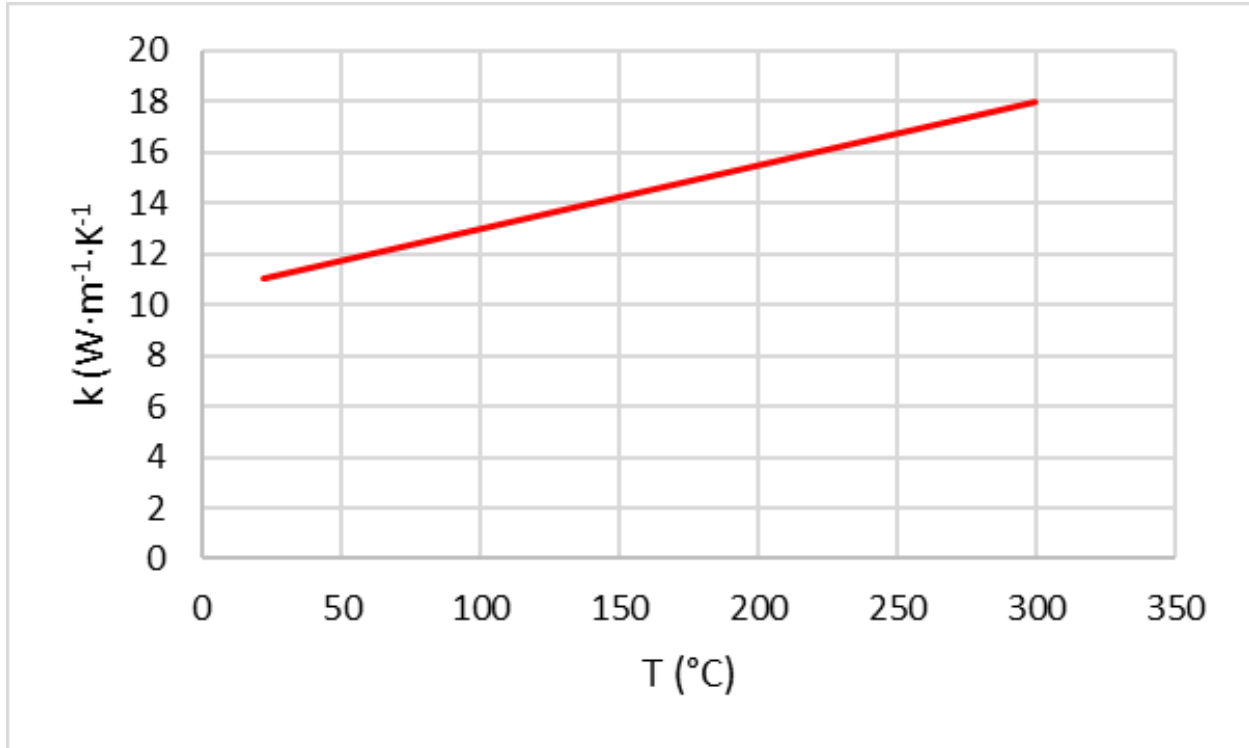
Figure 5-18. Thermal conductivity as a function of temperature. [87]

Table 5-2. Constant material properties of Nitinol.

Material	Nitinol
ϱ (kg·m^3)	6450
T_M (°C)	1300
C_P (J·kg^{-1}·K^{-1})	836.8
σ_T (MPa)	895
v (unitless)	0.33

5.3.2 Structure

The Both the thermal and structural portions of the thermomechanical simulation were modeled in ANSYS. Similarly, to the LFW FEA modeling, a 2D model was chosen in lieu of a 3D model. Although, as vertical deformations were a point of interest the structural portion used

56

a 3D model. The geometry of the thermal model was made to match the 2D cross-sectional view of the workpieces with the same length as the plates 60 mm, but the width was reduced to 10 mm as experimental data from the FLIR IR imaging camera indicated that the temperature normalizes at a width much shorter than the true width of the plates. Similarly, the structural model used the same dimensions with a thickness of 2 mm. Both the thermal and structural portions of the simulation shared the same model properties and mesh. To account for the movement of the laser the edges along the weld interface were divided into 12 segments each with a length of 5 mm. The reason for this was twofold. First, it allowed for the generate of a fine mesh along and near the weld interface while being course in the far field. Second, it allowed for the simulation of a moving heat input to via the application of heat input functions to individual edge segments during the simulation. The model geometry used for this simulation can be seen in Figure 5-19 where the green zone is the Ti-64 side and the yellow zone is the Nitinol side.
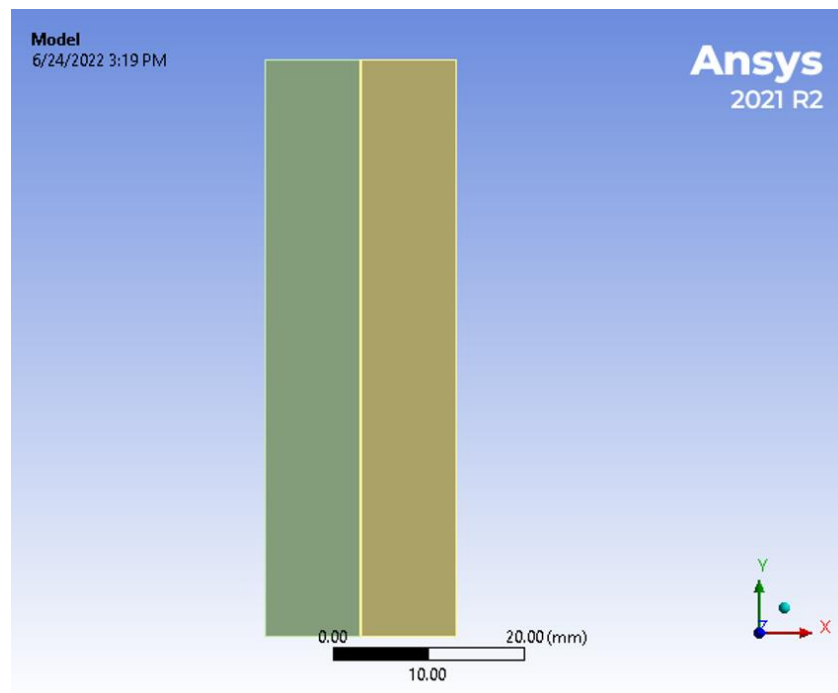
Figure 5-19. Model geometry for both the transient thermal and the transient structural

simulations

57

The mesh for the transient thermal simulation was created by modifying the program recommended settings. The element size was left to its default setting. The left and rightmost edges of the model were set to have 40 divisions, while each of the 12 segments along the weld interface had 60 divisions. This allowed for the generation of fine mesh along the interface with a courser mesh in the far field. Along with this, smoothing was set to high and element edges were set to be straight with all other settings left to their default values. This resulted in a total of 65351 nodes and 20869 elements. The transient structural simulation utilized the same mesh as the transient thermal simulation. Figure 5-20 shows the resulting mesh for both the transient thermal and transient structural model, and Figure 5-21 displays a zoomed-in view of the mesh along the weld interface.
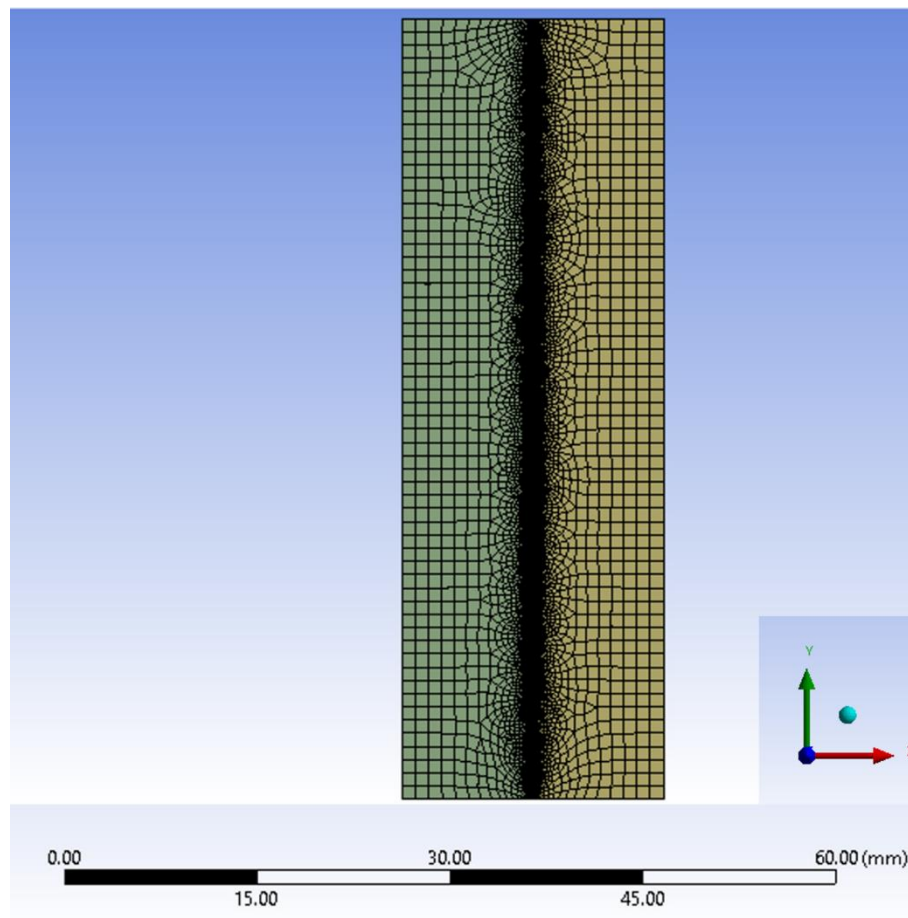
Figure 5-20. Mesh distribution for the LW FEA model.

58
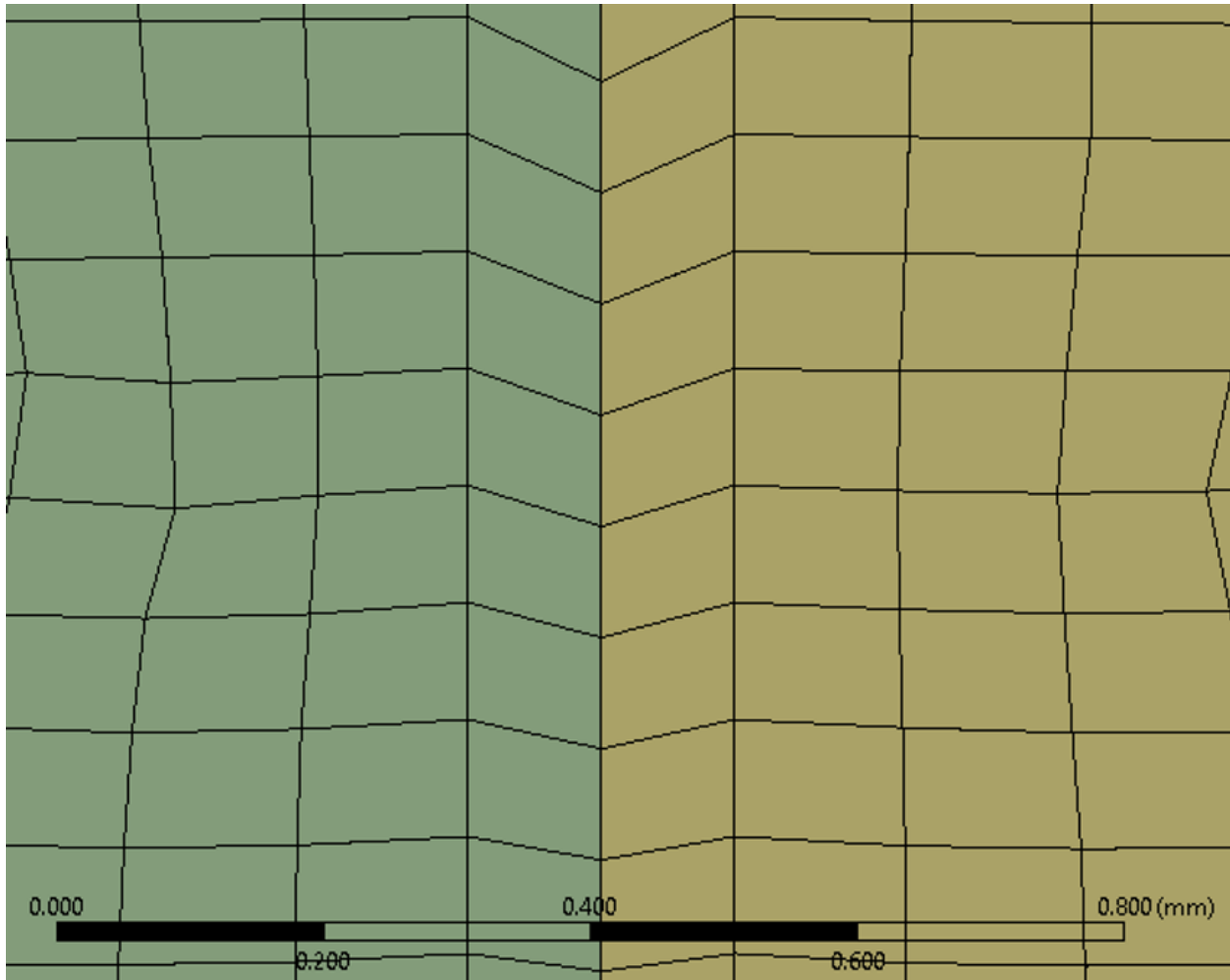
Figure 5-21. Zoomed in view of mesh elements along the weld interface of the transient thermal FEA model.

5.3.3 Simulation Model – Transient Thermal Analysis

As the workpieces are motionless during the welding process, the effect of convective heat transfer could be approximated to zero. The top and bottommost edges where set to radiate heat to the surroundings with the ambient temperature set to 22°C. A temperature boundary condition was applied to the left and rightmost edges such that their temperature would increase until it reached the normalized temperature of 700°C at the end of the simulation. To simulate the moving heat input from the laser, a quadratic heat input was sequentially applied to each

segment along the weld interface. This simulation was modeled to simulate the welding of specimen 1 from trial 1. The constraints and applied for the transient thermal model can be seen below in Figure 5-22.
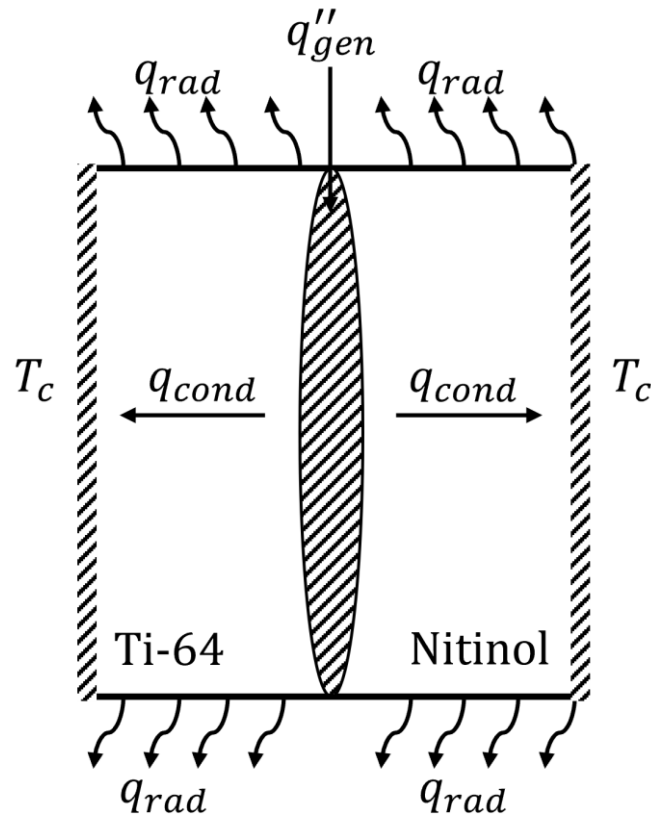
Figure 5-22. Transient Thermal Constraints.

5.3.4   Simulation Model — Transient Structural Analysis

The transient structural simulation was modeled in ANSYS using the same model from the transient thermal model, considering deformation for both workpieces. As both workpieces are stationary during the welding process, their outermost edges were constrained to be fixed along with the side and bottom surfaces. In addition to this, at distances greater than 1.5 mm from the weld interface were fixed. This was to ensure that the weld interface and the area around it was allowed to freely deform.

60

5.4 RESULTS AND DISCUSSION – THERMAL ANALYSIS

The results from the thermal simulation are shown in Figures Figure 5-23 through Figure 5-25. With Figure 5-23 showing thermal profile across the specimen at the end of the welding process, Figure 5-24 plotting the development of the maximum temperature along the weld interface over time, and Figure 5-25 showing a plot comparing the simulated development of the maximum temperature along the weld interface over time to the experimental thermal profile found in Figure 5-4. From Figure 5-25 it is clear that the simulated thermal profile is a good fit to the experimental thermal profile, being within a 5% error tolerance of the experimental profile. Thus, the simulation model is both accurate to the experimental data and able to predict thermal values throughout the welding process.
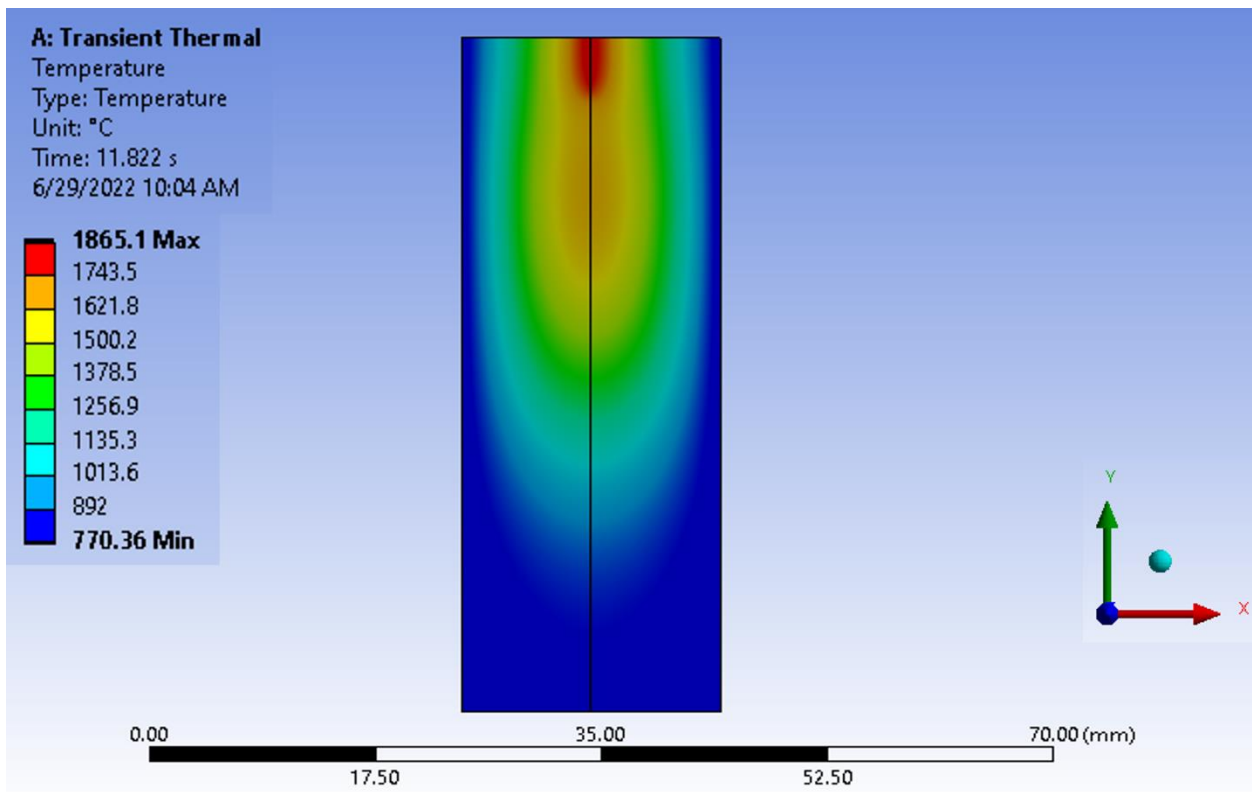
Figure 5-23. Temperature field across the workpieces at the end of the simulation.
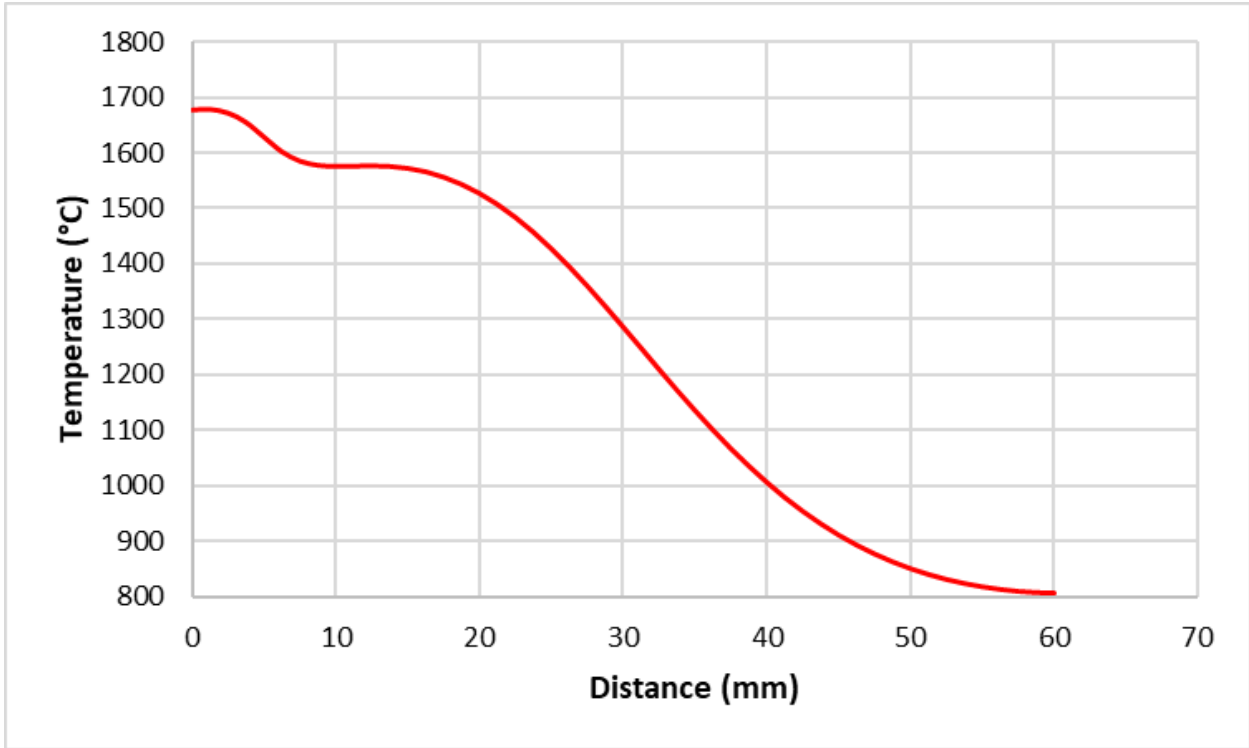
Figure 5-24. Temperature profile along the weld interface at the end of the simulation.
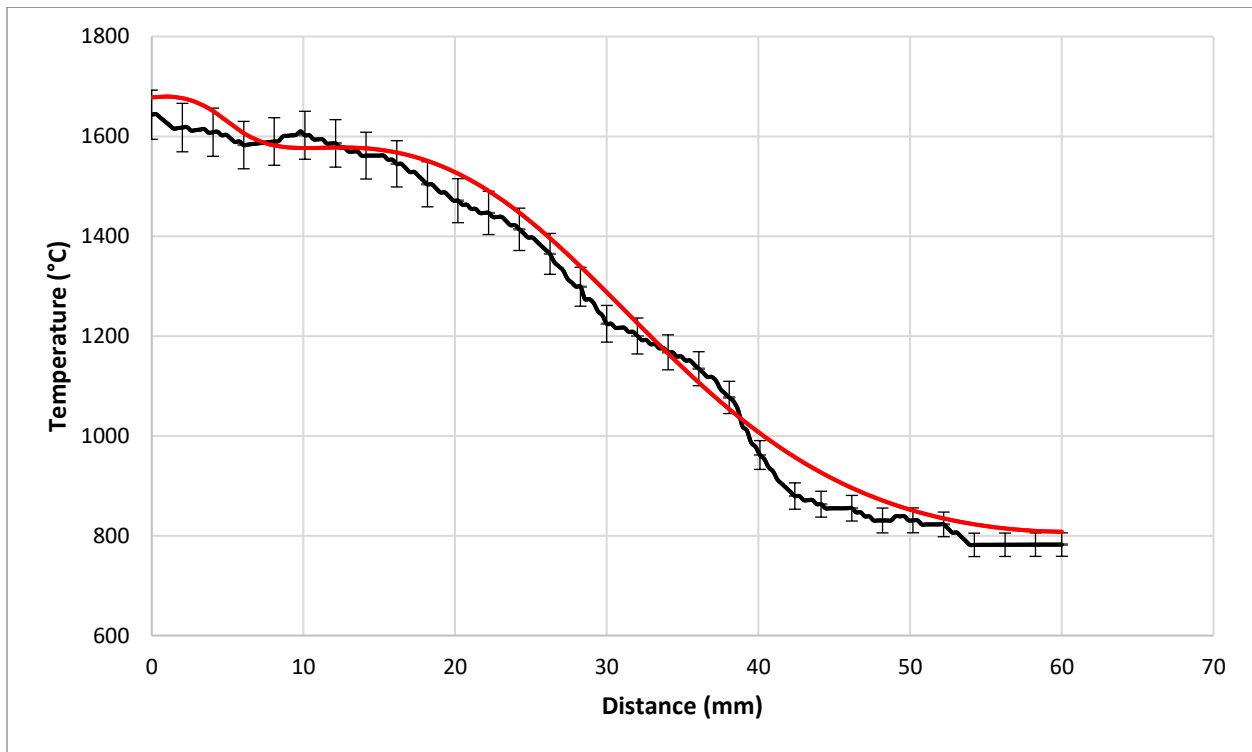
Figure 5-25. Comparison of the thermal model to experimental results.

5.5 Results and Discussion – Structural Analysis

The deformation was caused by the thermal stress and thermal expansion. The deformation field at the end of the simulation can be seen in Figure 5-26. The deformation profile along the weld interface at the end of the simulation can be seen in Figure 5-27. The simulation only encompasses the welding process not the cooling phase in which thermal expansion would retract to its final deformation after resolidification. The experimental results show at the material along the weld interface melting and resolidifying was the dominant factor that shaped the weld deformation. The simulation only considered thermal stress and expansion, but not melting and resolidification. In trial 1, weld penetration did not reach the plate thickness thus the plates were not fully bonded to each other. In trial 2 weld penetration exceeded the plate thickness which caused the bottom of the plate to melt. Thus both trials failed to produce successful bonding.
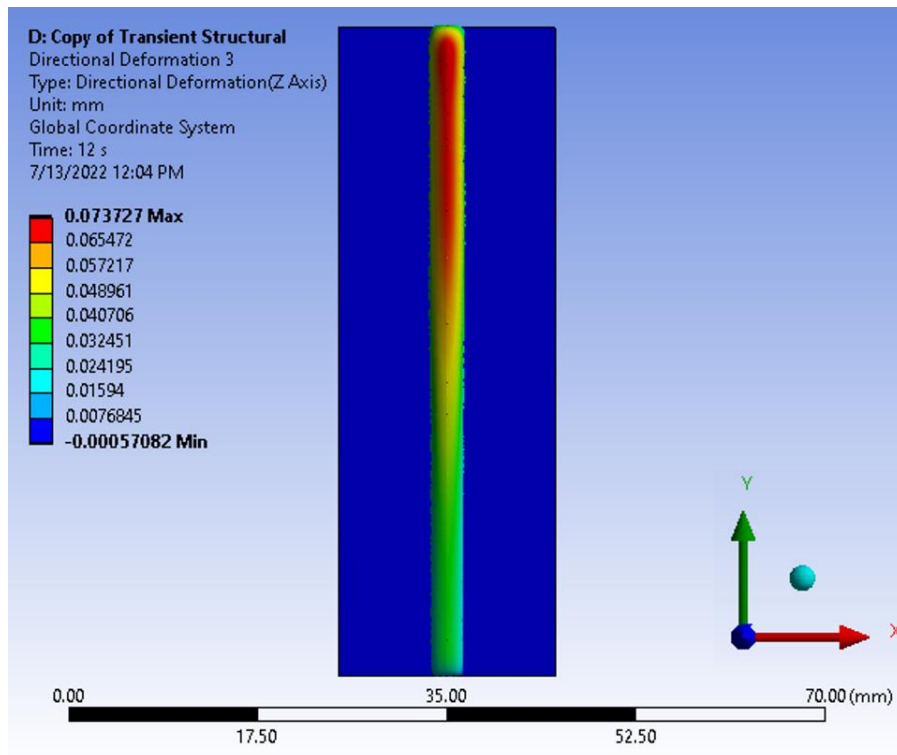
Figure 5-26. Deformation field at the end of the simulation.

63
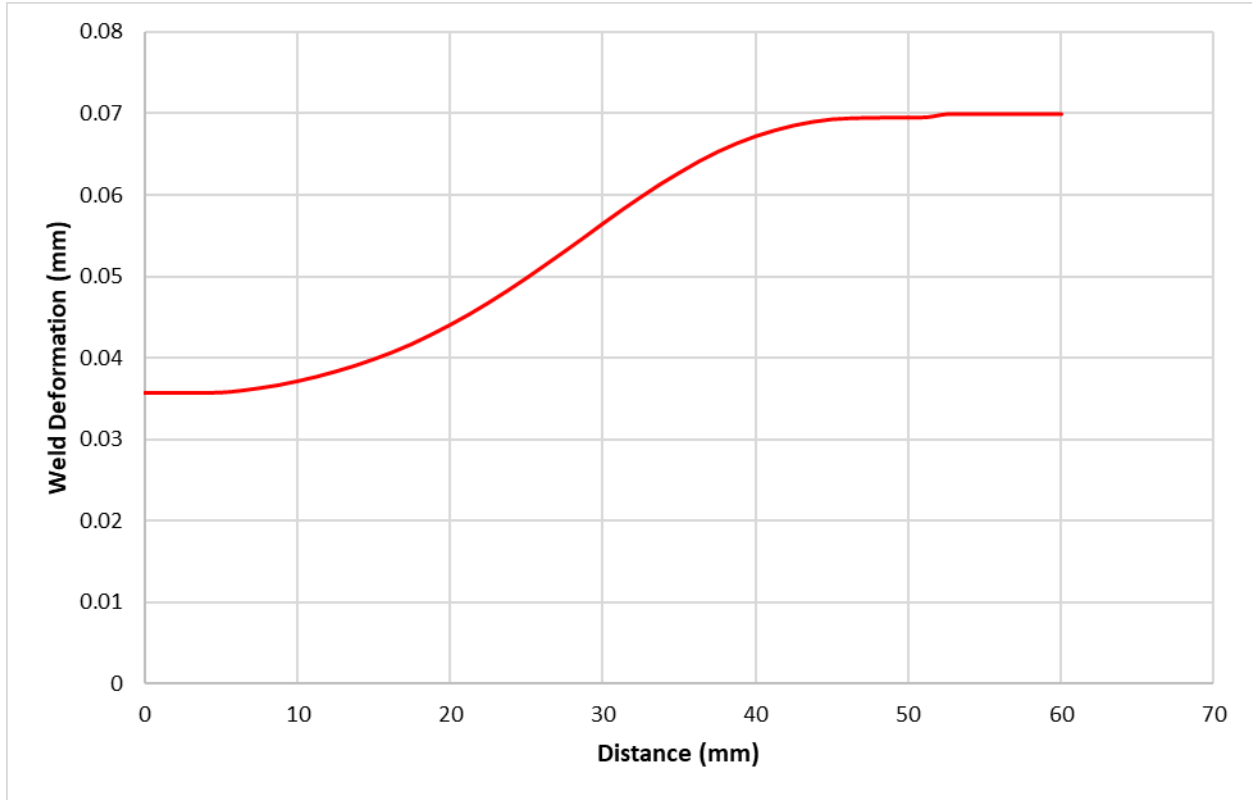
Figure 5-27. Deflection profile along the weld interface at the end of the simulation.

As it was not feasible to measure the deformation profile along the weld interface during the welding process the simulated longitudinal deformation profile could not be compared to the experimental results. Instead, the simulation results were compared to the deformation profile across the weld interface. With the assumption that the deformation profile was symmetric centered around the weld interface. Figure 5-28 illustrates the comparison between the comparison between the simulation's transverse deformation profile and the experimental data points across the weld interface. From Figure 5-28 it is also shown that the simulation's results are within 5% error of the experimental data. As both Figures 5-25 and 5-28 show that both the thermal and structural simulation results follow the trend as their respective experimental data and are within 5% error, it can be concluded that the simulation model is accurate and can predict thermal values during the LW process.
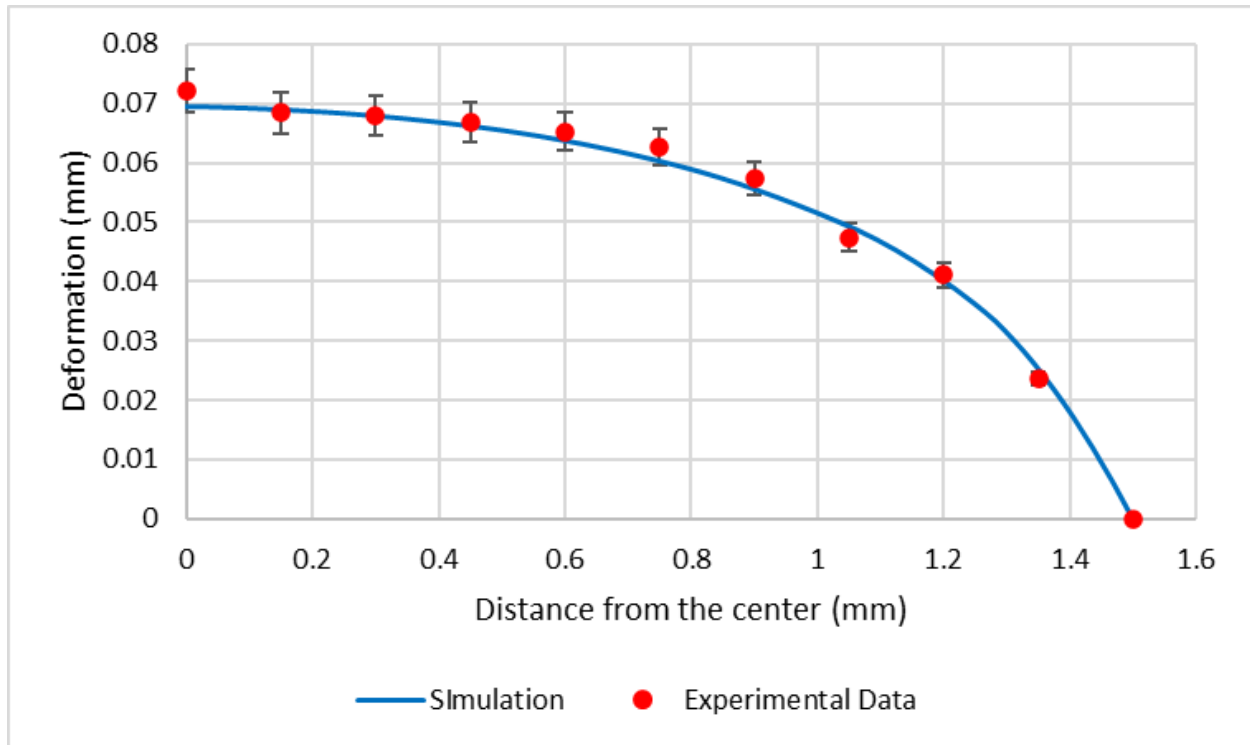
Figure 5-28. Comparison of the simulated transverse deformation profile to experimental results.

5.6 CONCLUSIONS

This study produced a FEA model to predict the temperature profile of welded workpieces along and across the weld interface throughout the welding process. The analysis also shows the structural deformation generated from the LFW process which fall in line with the experimental results. The thermal model accounted for conduction and radiation only as the workpieces were stationary making heat loss due to convection negligible. Results from the thermal simulation measure within 5% error tolerance to the experimental data. The welding process was monitored with an IR camera to record the development of the thermal profile of both the weld-affected area and the entirety of both workpieces during welding. Which reduced its material strength such that bonding was not possible. The SEM and EDS analysis showed that the intermetallic interactions between the two metals did occur along the weld interface.

65

Although thermal cracking occurred during both trials, its presence in trial 2 was significantly increased. This indicates that the use of laser power at or above 1500 W will result massive amounts of thermal cracking and failure to bond so long as all other parameters are in line with the parameters used in this study. While the thermal cracking was less severe in trial 1 it too resulted in unsuccessful bonding. This suggests that to bond these two dissimilar metals a low laser power is necessary when the plate thickness is small. Alternatively, the use of thicker plates could improve bonding as the laser penetration would not melt down to the underside of the plates. In conclusion, the joining of Ti-64 to Nitinol via LW is possible but further research into the ideal process parameters and workpiece thicknesses is needed.

6 REFERENCES

[1]   A. R. McAndrew, P. A. Colegrove, C. Bühr, B. C. Flipo and A. Vairis, "A literature review of Ti-6AL-4V linear friction welding," *Progress in Materials Science,* vol. 92, pp. 225-257, 2018.

[2]   A. W. Glaspell, C. Seydlorsky, J. J. Ryu and K. Choo, "Thermal Stress Simulation Model of DIssimilar Linear Friction Welding (LFW) Technology for Manufacturing of Bi-Metallic Biomedical Implants," in *ASME International Manufacturing Science and Engineering Conference*, USA, 2020.

[3]   I. Bhamji, M. Preuss, P. L. Threadgill and A. C. Addison, "Solid state joining of metals by linear friction welding: a literature review," *Materials Science and Technology,* vol. 27, no. 1, pp. 2-12, 2011.

[4]   M. E. Sapp, "A History of Welding," WELDINGHISTORY.ORG, 1 May 2003. [Online]. Available: http://www.weldinghistory.org/. [Accessed 1 March 2022].

[5]   B. Uday M., M. N. Ahmad Fauzi, H. Zuhailawati and A. B. Ismail, "Advances in friction welding process: a review," *Science and Technology of Welding and Joining,* vol. 15, no. 7, pp. 534-558, 2010.

[6]   T. J. Ma, Y. Zhong, W.-Y. Li, Y. Zhang, S. Q. Yang and C. L. Yang, "On microstructure and mechanical properties of linear friction welded dissimilar Ti–6Al–4V and Ti–6·5Al–3·5Mo–1·5Zr–0·3Si joint," *Science and Technology of Welding and Joining,* vol. 17, no. 1, pp. 9-12, 2012.

[7]   M. R. Daymond and N. W. Bonner, "Measurement of strain in a titanium linear friction weld by neutron diffraction," *Physica B: Condensed Matter,* vol. 325, pp. 130-137, 2003.

[8]   E. Ceretti, L. Fratini, C. Giardini and D. L. Spisa, "Numerical modelling of the linear friction welding process," *International Journal of Material Forming,* vol. 3, pp. 1015-1018, 2010.

[9]   W.-Y. Li, T. Ma, Q. X. Zhang, L. S. Yang and H. Liao, "Microstructure Characterization and Mechanical Properties of Linear Friction Welded Ti-6Al-4V Alloy," *Advanced Engineering Materials,* vol. 10, no. 1, pp. 89-92, 2008.

[10]   T. J. Ma, W. Y. Li, B. Zhong, Y. Zhang and J. L. Li, "Effect of post-weld heat treatment on microstructure and property of linear friction welded Ti17 titanium alloy joint," *Science and Technology of Welding and Joining,* vol. 17, no. 3, pp. 180-185, 2012.

[11]   J. Sorina-Müller, M. Rettenmayr, D. Schneefeld, O. Roder and W. Fried, "FEM simulation of the linear friction welding of titanium alloys," *Computational Materials Science,* vol. 48, no. 4, pp. 749-758, 2010.

[12]   V. Corzo, O. Casals, J. Alcalá, M. A. and M. Anglada, "Mechanical evaluation of linear friction welds in titanium alloys through indentation experiments," *Welding International,* vol. 21, no. 2, pp. 125-129, 2007.

[13]   M. Maalekian, "Friction welding – critical assessment of literature," *Science and Technology of Welding and Joining,* vol. 12, no. 8, pp. 738-759, 2007.

[14]   T.-S. Jun, F. Rotundo, X. Song, L. Ceschini and A. M. Korsunsky, "Residual strains in AA2024/AlSiCp composite linear friction welds," *Materials & Design,* vol. 31, no. Supplement 1, pp. S117-S120, 2010.

[15]   I. Bhamji, R. J. Moat, M. Preuss, P. L. Threadgill, A. C. Addison and M. J. Peel, "Linear friction welding of aluminium to copper," *Science and Technology of Welding and Joining,* vol. 17, no. 4, pp. 314-320, 2012.

[16]   I. Bhamji, M. Preuss, R. J. Moat, P. L. Threadgill and A. C. Addison, "Linear friction welding of aluminium to magnesium," *Science and Technology of Welding and Joining,* vol. 17, no. 5, pp. 368-374, 2012.

[17]   P. Wanjara and M. Jahazi, "Linear friction welding of Ti-6Al-4V: Processing, microstructure, and mechanical-property inter-relationships," *Metallurgical and Materials Transactions A,* vol. 36, p. 2149–2164, 2005.

[18]   A. Addison, "Linear friction welding information for production engineering," TWI industrial members report - 961/2010, Cambridge, 2010.

[19]   A. Addison, "Linear friction welding of engineering metals," TWI industrial members report - 894/2008, Cambridge, 2008.

[20]   U. U. Ofem, P. A. Colegrove, A. Addison and M. J. Russel, "Energy and force analysis of linear friction welds in medium carbon steel," *Science and Technology of Welding and Joining,* vol. 15, pp. 479-485, 2010.

[21]   A. R. McAndrew, P. A. Colegrove, A. C. Addison, B. C. Flipo and M. J. Russel, "Energy and Force Analysis of Ti-6Al-4V Linear Friction Welds for

Computational Modeling Input and Validation Data," *Metallurgical and Materials Transactions A,* vol. 45, pp. 6118-6128, 2014.

[22]   R. Turner, J.-C. Gebelin, R. Ward and R. Reed, "Linear friction welding of Ti–6Al–4V: Modelling and validation," *Acta Materialia,* vol. 59, no. 10, pp. 3792-3803, 2011.

[23]   A. Chamanfar, M. Jahazi and J. Cormier, "A Review on Inertia and Linear Friction Welding of Ni-Based Superalloys," *Metallurgical and Materials Transactions A,* vol. 46, p. 1639–1669, 2015.

[24]   American Welding Society, Welding handbook, 8th ed., vol. 1, L. P. Connor, Ed., Miami, FL: American Welding Society, 1987.

[25]   V. I. Vill, Friction Welding of Metals, New York: American Welding Society, Inc., 1962.

[26]   P. Romilly, "Linear friction welding for near net shape manufacturing of titanium parts," in *Proceedings of the 13th World Conference on Titanium*, San Diego, 2016.

[27]   H. H. Koo and W. A. Bareslack III, "Structure, properties, and fracture of linear friction welded Al-Fe-V-Si alloy 8009," *Materials Characterization,* vol. 28, no. 2, pp. 157-164, 1992.

[28]   E. Akca and A. Gursel, "The importance of interlayers in diffusion welding - A review," *PERIODICALS OF ENGINEERING AND NATURAL SCIENCES,* vol. 3, pp. 12-16, August 2015.

[29]   K. M. Vijay, "Resistance Spot Welding, A Review," *International Journal of Mechanical and Production Engineering Research and Development (IJMPERD),* vol. 8, no. 2, pp. 403-418, 2018.

[30]   S. M. Manladan, M. F. Hamza and I. Abdullahi, "A REVIEW ON THE APPLICATION OF RESISTANCE SPOT WELDING OF AUTOMOTIVE SHEETS," *Journal of Engineering and Technology,* vol. 10, pp. 20-37, 2015.

[31]   C. Rajarajan, P. Sivaraj, T. Sonar, S. Raja and N. Mathiazhagan, "Resistance spot welding of advanced high strength steel for fabrication of thin-walled automotive structural frames," *Forces in Mechanics,* vol. 7, pp. 1-13, 2022.

[32]   D. Tanmoy, "Resistance Spot Welding: Principles and Its Applications," in *Engineering Principles - Welding and Residual Stresses*, London, IntechOpen, 2022.

[33]   M. Shafi, "Resistance Spot Welding: Definition, Construction, Working Principle, Applications, Defects, Advantages, and Disadvantages [PDF]," Mechanical E-Notes, [Online]. Available: https://mechanicalenotes.com/resistance-spot-welding/. [Accessed 24 June 2022].

[34]   S. K. Bhudolia, G. Gohel, K. F. Leong and A. Islam, "Advances in Ultrasonic Welding of Thermoplastic Composites: A Review," *Materials (Basel),* vol. 13, pp. 1-26, 2020.

[35]   A. Yousefpour, M. Hojjati and J.-P. Immarigeon, "Fusion Bonding/Welding of Thermoplastic Composites," *Journal of Thermoplastic Composite Materials,* vol. 17, pp. 303-341, 2004.

[36] D. A. Grewell, A. Benatar and J. B. Park, Plastics and Composites Welding Handbook, Munich: Hanser Gardner Publications, 2013.

[37] I. F. Villegas, L. Moser, A. Yousefpour, P. Mitschang and H. E. Bersee, "Process and performance evaluation of ultrasonic, induction and resistance welding of advanced thermoplastic composites," *Journal of Thermoplastic Composite Materials,* vol. 26, pp. 1007-1024, 2013.

[38] I. Mihaela and S. Elena, "An overview of welding in solid state," *The Annals of "Dunarea de Jos" University Of Galati,* vol. 12, pp. 31-38, 2008.

[39] D. Ananthapadmanaban and K. A. V. Geethan, "Fracture Behavior of Solid-State Welded Joints," in *Engineering Failure Analysis*, London, United Kingdom, IntechOpen, 2020.

[40] K. Satish, M. Aishna, K. Santosh and S. Harvinder, "Friction stir welding: Types, merits & demerits, applications, process variables & effect of tool pin profile," *Materials Today: Proceedings,* Vols. 56, Part 5, pp. 3051-3057, 2022.

[41] A. R. McAndrew, *Modelling of Ti-6Al-4V Linear Friction Welds,* Bedfordshire: Cranfield University, 2015.

[42] R. Rudrapati, "Effects of welding process conditions on friction stir welding of polymer composites: A review," *Composites Part C: Open Access,* vol. 8, pp. 1-7, 2022.

[43] D. K. Soni, "A Review of Laser Welding Process for Thin Steel Sheets," *International Journal of Research in Modern Engineering and Emerging Technology,* vol. 1, no. 3, pp. 94-100, April 2013.

[44]   J. Svenungsson, I. Choquet and A. F. Kaplan, "Laser Welding Process – A Review of Keyhole Welding Modelling," *Physics Procedia,* vol. 78, pp. 182-191, 2015.

[45]   C. A. Walsh, "LASER WELDING - Literature Review," Materials Science and Metallurgy Department, University of Cambridge, Cambridge, England, 2002.

[46]   A. Bhuvaneshwaran, B. Anandavel and D. Noorullah, "A Literature Review On Laser Beam Welding Processes," *International Journal for Science and Advance Research In Technology,* vol. 6, no. 12, pp. 56-62, December 2020.

[47]   C. P. Mazmudar and K. Patel, "A Literature Review on Effect of Laser Welding Parameters on," *International Journal for Scientific Research & Development,* vol. 1, no. 10, pp. 2102-2105, 2013.

[48]   B. Flipo, K. Beamish, B. Humphreys, M. Wood and A. Shilton, "Linear Friction Welding of TI 6AL 4V for Aerostructure Applications," in *Trends in Welding Research Proceedings of the 10th International Conference*, Tokyo, 2016.

[49]   S. Bertrand, "Finite Element Modeling of the Linear Friction Welding Process," UNIVERSITÉ DU QUÉBEC, Montreal, 2019.

[50]   A. Chamanfar, M. Jahazi, J. Gholipour, P. Wanjara and S. Yue, "Maximizing the integrity of linear friction welded Waspaloy," *Materials Science and Engineering: A,* vol. 555, pp. 117-130, 2012.

[51]   A. M. García, BLISK Fabrication by Linear Friction Welding, E. Benini, Ed., InTechOpen, 2011, pp. 411-434.

[52]	L. A. Lee, A. McAndrew, C. Buhr, K. A. Beamish and P. A. Colegrove, "2D Linear Friction Weld Modelling of a Ti-6Al-4V T-Joint," *Journal of Engineering Science and Technology Review,* vol. 8, no. 6, pp. 44-48, 2015.

[53]	A. Vairis and M. Frost, "High frequency Linear friction welding of a titanium alloy," *Wear,* vol. 217, no. 1, pp. 117-131, 1998.

[54]	A. Vairis, *High frequency linear friction welding,* Bristol: University of Bristol, 1998.

[55]	A. R. McAndrew, P. A. Colegrove, A. C. Addison, B. C. Flipo and J. Michael, "Modelling the influence of the process inputs on the removal of surface contaminants from Ti–6Al–4V linear friction welds," *Materials & Design,* vol. 55, no. Part A, pp. 183-195, 2015.

[56]	A. R. McAndrew, P. A. Colegrove, A. C. Addison, B. C. Flipo, M. J. Russel and L. A. Lee, "Modelling of the workpiece geometry effects on Ti–6Al–4V linear friction welds," *Materials & Design,* vol. 87, no. 15, pp. 1087-1099, 2015.

[57]	A. Vairis and M. Frost, "On the extrusion stage of linear friction welding of Ti 6Al 4V," *Materials Science and Engineering: A,* vol. 271, no. 1-2, pp. 477-484, 1999.

[58]	A. Vairis and M. Frost, "Modelling the linear friction welding of titanium blocks," *Materials Science and Engineering: A,* vol. 292, no. 1, pp. 8-17, 2000.

[59]	Y. Guo, T. Jung, L. Chiu Yu, L. Hangyue, S. Bray and P. Bowen, "Microstructure and microhardness of Ti6246 linear friction weld," *Materials Science and Engineering: A,* vol. 562, pp. 17-24, 2013.

[60]   M. Karadge, M. Preuss, C. Lovell, P. J. Withers and S. Bray, "Texture development in Ti–6Al–4V linear friction welds," *Materials Science and Engineering: A,* vol. 459, no. 1-2, pp. 182-191, 2007.

[61]   Y. Guo, Y. Chiu, M. M. Attallah, H. Li, S. Bray and P. Bowen, "Characterization of Dissimilar Linear Friction Welds of α-β Titanium Alloys," *Journal of Materials Engineering and Performance,* vol. 21, pp. 770-776, 2012.

[62]   W. Li, A. Vairis, M. Preuss and T. Ma, "Linear and rotary friction welding review," *International Materials Reviews,* vol. 61, no. 2, pp. 71-100, 2016.

[63]   A. Paoletti, F. Lambiase and A. Di Ilio, "Optimization of Friction Stir Welding of Thermoplastics," *Procedia CIRP,* vol. 33, pp. 562-567, 2015.

[64]   S. Eslami, B. V. Farahani, P. J. Tavares and P. Moreira, "Fatigue behaviour evaluation of dissimilar polymer joints: Friction stir welded, single and double-rivets," *International Journal of Fatigue,* vol. 113, pp. 351-358, 2018.

[65]   Y. Huang, X. Meng, Y. Wang, Y. Xie and L. Zhou, "Joining of aluminum alloy and polymer via friction stir lap welding," *Journal of Materials Processing Technology,* vol. 257, pp. 148-154, 2018.

[66]   APCI, LLC, "White Paper on Solid State Bonding and APCI's Linear Friction Welding Technology," 2011.

[67]   B. Lang, T. C. Zhang, X. H. Li and D. L. Guo, "Microstructural evolution of a TC11 titanium alloy during linear friction welding," *Journal of Materials Science,* vol. 45, pp. 6218-6224, 2010.

[68]   L. Kuncˇická, K. Radim and C. Lowe Terry, "Advances in metals and alloys for joint replacement," *Progress in Materials Science,* vol. 88, pp. 232-280, 2017.

[69]   M. Semlitsch, "Titanium alloys for hip joint replacements," *Clinical Materials,* vol. 2, pp. 1-13, 1987.

[70]   A. R. McAndrew and B. C. D. Flipo, "Linear Friction Welding for Near Net Shape Manufacturing of Titanium Alloy Ti-6Al-4V Aerospace Components," in *2018 9th International Conference on Mechanical and Aerospace Engineering (ICMAE)*, Budapest, 2018.

[71]   ANSYS, "Ti-6AL-4V Material Properties," ANSYS, Inc., Canonsburg, 2021.

[72]   M. Boivineau, C. Cagran, D. Doytier, V. Eyraud, M.-H. Nadal, B. Wilthan and G. Pottlacher, "Thermophysical Properties of Solid and Liquid Ti-6Al-4V (TA6V) Alloy," *International Journal of Thermophysics,* vol. 27, no. 2, pp. 507-529, March 2006.

[73]   K. Moghadasi, M. S. M. Isa, A. M. Ariffin, M. Z. M. Muhammad Zulhiqmi Mohd jamil, S. Raja, B. Wu, M. Yamani, B. R. M. Muhamad, F. Yusof, F. M. Jamaludin, S. b. A. K. Mohd, B. b. A. Razak and N. b. Yusoff, "A review on biomedical implant materials and the effect of friction stir based techniques on their mechanical and tribological properties," *Journal of Materials Research and Technology,* vol. 17, pp. 1054-1121, March-April 2022.

[74]   C. Song, M. Zhang, Y. Yang, D. Wang and Y. Jia-kuo, "Morphology and properties of CoCrMo parts fabricated by selective laser melting," *Materials Science & Engineering A,* vol. 713, no. 24, pp. 206-213, 2018.

[75]   F. Schroeder, R. M. Ward, R. P. Turner, M. M. Attallah, J.-C. Gebelin and R. C. Reed, "Linear friction welding of titanium alloys for aeroengine applications: Modelling and validation," in *Trends in Welding Research, Proceedings of the 9th International Conference*, Chicago, 2012.

[76]   P. Jedrasiak, H. Shercliff, A. McAndrew and P. Colegrove, "Thermal modelling of linear friction welding," *Materials & Design,* vol. 156, pp. 362-369, 15 October 2018.

[77]   P. Jedrasiak and H. R. Shercliff, "Modelling of heat generation in linear friction welding using a small strain finite element method," *Materials & Design,* vol. 177, pp. 1-10, 2019.

[78]   W. Li and F. Wang, "Numerical Simulation of Linear Friction Welding Based on ABAQUS Environment: Challenges and Perspectives," *Journal of Materials Engineering and Performance,* vol. 23, pp. 384-390, 2013.

[79]   D. Irwin, C. Seydlorsky, A. Gautam, A. W. Glaspell, K. Choo and J. Ryu, "Dissimilar linear friction welding technology for manufacturing of functional materials: Bi-metallic Ti6Al4V-CoCrMo joint implants," in *Summer Biomechanics, Bioengineering, and Biotransport Conference*, Seven Springs, USA, 2019.

[80]   P. Geng, G. Qin, L. Changan, W. Hao and J. Zhou, "Study on the importance of thermo-elastic effects in FE simulations of linear friction welding," *Journal of Manufacturing Processes,* vol. 56, no. A, pp. 602-615, 2020.

[81]   ASTM Standard, *Standard Test Methods for Tension Testing of Metallic Materials,* West Conshohocken: ASTM International, 2013.

[82]   ASTM Standard, *Standard Specification for Wrought Cobalt-28Chromium-6Molybdenum Alloys for Surgical Implants,* West Conshohocken: ASTM International, 2011.

[83]   W.-Y. Li, T. Ma and J. Li, "Numerical simulation of linear friction welding of titanium alloy: Effects of processing parameters," *Materials & Design,* vol. 31, no. 3, pp. 1497-1507, 2010.

[84]   R. Turner, R. M. Ward, R. March and R. C. Reed, "The Magnitude and Origin of Residual Stress in Ti-6Al-4V Linear Friction Welds: An Investigation by Validated Numerical Modeling," *Metallurgical and Materials Transactions B,* vol. 43, pp. 186-197, 2012.

[85]   A. Glaspell, J. J. Ryu and K. Choo, "Thermal Stress Simulation Model of Ti6Al4V-NITI DIssimilar Laser Welding Process," in *ASME International Manufacturing Science and Engineering Conference*, USA, 2021.

[86]   S. P. Mizar, "Thermomechanical characterization of NiTiNOL and NiTiNOL based structures using ACES methodology," Worcester Polytechnic Institute, Worcester, 2005.

[87]	M. K. Stanford, "Thermophysical Properties of 60-NITINOL for

Mechanical Component Applications," NASA, Cleveland, 2012.